DOCTORAL DISSERTATION

Investigating hydrodynamics of an artificial estuarine channel that is affected by a flood control structure
(洪水制御構造物の影響を受けた人工感潮水路の流体力学に関する調査研究)

March 2023

Department of Civil and Environmental Engineering

Graduate School of Engineering

Hiroshima University

GILLANG NOOR NUGRAHANING GUSTI

Acknowledgements

Acknowledgements

The members of my supervisory committee deserve the best accolades and my deepest thanks for their expertise, encouragement and support. Prof. Kawanishi was particularly generous with his encouragement, guidance, support, and patience during the course of my doctoral study at the Hiroshima University.

I would like to express my gratitude to Nakashita Sensei for his help and support in the laboratory and Dr. Mohammad Basel Al Sawaf for hid wonderful support and guidance during my field experiment, paper writing, and also life outside of academics. I also thank all the laboratory members, Faruq, Xiao, Mori, Torigoe, Hiep, and Guo for their helps and supports. I also thank Dr. Mochammad Meddy Danial and Dr. Henny Herawati for their cooperation in the international collaboration research project.

In this opportunity, I would like to thank the Ministry of Education, Culture, Sports, Science and Technology (MEXT) Japan for supporting my doctoral program at Hiroshima University. I am sincerely grateful for the opportunity that has been given to me to experience living and studying in Japan.

Thank you to all friends and colleagues who supported me during my doctoral study at Hiroshima, particularly my organization committee of PPI Hiroshima (the Indonesian Student Association in Hiroshima) in the 2019/2020 period and my cycling buddies from "Ngonthel Hiroshima".

I would like to thank my family, my parents Mr. Ginna Santosa and Mrs. Lilis Rusenywati for their nonstop supports and prayers, and also my little sister and brothers Nurma, Ghifa, and Ozzy. Last but not least, I am particularly grateful to Lillah Zuhrotul Ukhro, for your existence in my life and your endless supports through thick and thin. You gave me lights when there was only dark around me and together with you, I was to grow old.

GILLANG NOOR NUGRAHANING GUSTI
Higashi Hiroshima, Japan

Table of Contents

Table of Contents

List of Symbols

Symbol		Unit
u_s	Current velocity in the longitudinal direction	m/s
u_n	Current velocity in the lateral direction	m/s
R_s	Radius of curvature	m
ρ_0	Constant reference density	m^3/s
ρ	Water density	kg/m^3
η	Water level	m
Q	Discharge	m^3/s
T	Temperature	°C
S	Salinity	ppt
N	Brunt Vaisala frequency	1/s
Ri	Gradient Richardson number	m
Φ	Potential energy anomaly	J/m^3
g	Gravitational acceleration	m/s^2
h	Water depth	m
$\bar{u}_t$	Depth-averaged tidal velocity	m/s
$\bar{u}_r$	Depth-averaged river velocity	m/s
A_z	Vertical eddy viscosity	m^2/s
k	Bottom drag coefficient	-
k_s	Surface stress coefficient	-
ρ_a	Air density	kg/m^3
$\overline{U_a}$	Height-averaged wind velocity	m/s
ε, δ	Mixing efficiency parameters	-
Fr	Residual flow-induced subtidal friction	$kg\ m/s^2$
Ft	River-tide interaction-induced subtidal friction	$kg\ m/s^2$
Frt	Tidal asymmetry-induced subtidal friction	$kg\ m/s^2$
$b_0(t)$	Mean water level	m
A_n	Tidal amplitude	m
ω	Tidal frequency	1/s
θ	Tidal phase	radian
W	Channel width	m

List of Symbols

$\widetilde{U}$	Nondimensionalized current velocity	

List of Notations

Notations	
ADCP	Acoustic Doppler Current Profiler
SPM	Suspended Particulate Matter
CTD	Conductivity-Temperature-Depth sensor
MLIT	Ministry of Land, Infrastructure, Transport and Tourism
CDW	Current Deflective Wall
ACT-HR	High Resolution, Automatic Conductivity-Temperature sensor
TP	Tokyo Peil

List of Figures

List of Figures

List of Figures

List of Tables

Abstract

Human activities have grown gradually over the decades to become the major force that modifies all aspects of nature, including the interaction of rivers and tides in estuaries. Understanding basic knowledge about circulation and mixing in estuaries is necessary to optimize the management strategy and long-term vision of developing and managing these unique environments. This dissertation investigated the spatiotemporal variations in estuarine circulation and subtidal dynamics to present a deeper understanding of how human intervention, particularly in an artificial estuarine channel known as the Ota Diversion Channel, affects estuarine hydrodynamics. This work is divided into three main themes: (i) the influence of a flood control structure on lateral flow dynamics, (ii) the intrinsic mechanisms of estuarine circulation due to the longitudinal variation in channel geometry, and (iii) the effects of regulated freshwater discharge on subtidal dynamics.

The purpose of the first theme was to investigate the lateral circulation that is affected by the flood control structure in an estuarine channel. In this study, a numerical simulation was utilized to simulate the secondary flow and salinity structure in the Ota Diversion Channel. The simulation was divided into two scenarios based on the existence of a flood gate. The simulation results showed that the existence of a flood gate affects the secondary flow structure. The gate provides resistance to water flow, thus limiting the streamwise velocity. This limitation induces a smaller centrifugal force, which results in the dominance of barotropic and baroclinic pressure gradients over other terms. The interaction between these two terms generated a strong secondary flow in the meandering section of the Ota Diversion Channel.

The second theme aims to offer a comprehensive understanding of the dynamics of tidal rivers with longitudinally varying channel geometry. To accomplish the aforementioned aims, this work provides a spatiotemporal analysis of the water current and density for a fortnight period of a mesotidal estuarine channel that encompasses both curved and straight channels in the streamwise direction. Moreover, a quantitative analysis of the governing mechanisms of estuarine dynamics was performed to determine the alteration of driving mechanisms due to channel geometry variation. The longitudinal velocity profile

Abstract

indicates the existence of tidal asymmetry, in which ebb currents are dominant over flood currents. The asymmetry, which is induced by the interaction between the channel curvature and density gradient, was observed to be more enhanced in the curved channel than in the straight channel. Moreover, the across-channel bathymetry difference between curved and straight channels leads to different patterns of lateral flow in those channels. Additionally, the longitudinal and lateral velocities averaged for the spring/neap tides revealed that the channel with a higher degree of curvature had greater residual circulation. However, the periodically varying density distribution denotes the existence of tidal straining, which is slightly modified by the variation in geometry. The notable findings of this study are as follows: (i) the variability in channel geometries introduces different responses of tidal straining and tidal stirring; (ii) the river effect (river-induced shear) in the curved channel substantially increases compared to the straight channel over a certain threshold of river runoff. The findings of this study deepen our understanding of tidal river dynamics in longitudinally varying channel geometries.

The aim of the third study was to examine the spatial and temporal behavior of subtidal friction and subtidal flux in a tidal river channel with limited river runoff. This study utilized the frequency domain and theoretical decomposition analyses to determine the dominant tidal and subtidal mechanisms. Frequency domain analysis indicated the dominance of semidiurnal and diurnal tides in the observed tidal river channels. The rate of energy transfer owing to shallow water interaction was found to be stronger for the current velocity than for the water elevation. Decom-position analysis showed that subtidal friction and flux in a low-discharge tidal river channel are largely influenced by subtidal flow-induced subtidal friction and Eulerian return flux, respectively. The key findings of this study are as follows: (i) the limited amount of river runoff (4–20 m^3/s) leads to the vertical variability of subtidal friction contributions from subtidal flow and subtidal-tidal interaction, as well as Eulerian return flux, and (ii) the vertical variability of the aforementioned terms can be associated with the existence of influential longitudinal subtidal density gradients along the tidal river. This study advances the understanding of subtidal dynamics in tidal river systems, particularly those with limited discharge.

Abstract

CHAPTER 1: Introduction

1.1 Study Overview

The estuary can be defined as a transitional coastal body of water that is directly connected to the seas, extending into the furthers limit of tidal influence into the river, and within which saltwater is measurably diluted by freshwater runoff derived from land drainage [1]. The interaction between propagating tides, which transport saline water into the estuary, and river runoff, which flushes saline water out of the estuary, generates density differences between the upstream and downstream ends of the estuary. These differences further induce density currents, which could act in both longitudinal and transversal water circulation and lead to a mixing process between saline and fresh water, adding complexity to the hydrodynamics of the estuary.

Because of the fertile water, navigational access for trades, and easy accessibility to the sources of materials, estuaries have been the main centers of human civilization for ages. In fact, close to half a billion people live on or close to estuaries in many mega-cities around the world [2]. Since estuaries are subject to rapid industrial development and economic growth, careful management of estuaries is required. Consequently, the promotion of trade and industry leads to the alteration of the natural dynamics within estuaries through various means such as alterations of topography, land subsidence, channel closure, dredging, construction of reservoirs, and flow control structures. However, different anthropogenic alterations have different effects on the estuarine hydrodynamics. Hence, examining the effects of human intervention in estuaries remains a challenge.

The Ota Diversion Channel, situated in the western part of the Hiroshima metropolitan area, was constructed from 1934 to 1967 to protect the area from annual floodings due to the East Asian monsoon [3,4]. The channel is intended to divert half of the total discharge that flows into the Ota River Estuary during floodings, mitigating the City of Hiroshima from heavy inundations that often occurred before channel construction. The channel has two prominent features in the form of (1) a set of three sluice gates (known as the Gion Flood gate) that limit the river runoff to flow in under normal discharge conditions and

(2) the unequal shapes of the channel, which comprises a meandering channel in its upstream area and a straight channel in its downstream part. These features, specifically motivated the author to inspect how they affect the spatial and temporal distribution of hydrodynamics in the estuarine channel, such as water circulation, salinity stratification, and friction. Therefore, in this study, we examine the hydrodynamics variations induced by flood control structure and variation in longitudinal channel geometry in an estuarine channel with the Ota River estuary as a case-specific example.

1.2 Literature Reviews

1.2.1   Estuarine circulation and the interaction between river and tides

The circulation and mixing processes in estuaries are affected by various mechanisms such as strong tidal currents, irregular bathymetry, season-varying river runoff, energetic turbulence, and abrupt density gradients due to the interaction between ocean and river waters [5]. Early studies of estuaries have discovered that estuarine circulation generates a two-layer flow structure that varies vertically, with the seaward surface net flow of less saline water and landward bottom net flow of saltwater [6]. This two-layer flow structures exists because of contributions from the surface water slope (barotropic component) and density field (baroclinic component) [1]. These mechanisms along with their adjacent flows, are referred to as gravitational circulation which is the fundamental principle of classical estuarine circulation [7].

Even though density-driven circulation is an important feature in estuarine circulation, tides are no less significant because of their influence on stratification, while the nonlinearities in the propagating tides also play a major role in estuarine residual circulation [5,8,9]. Simpson et al. [10] observed temporal variations in stratification generated by tidal flow acting on the longitudinal density gradient in the Liverpool Bay. This phenomenon, which is known as tidal straining or strain-induced periodic stratification (SIPS), tends to induce weakly stratified or well-mixed conditions during the flood and stratified conditions during the ebb. In an estuarine channel, the surface water shifts faster than the water column beneath it because of shear in the velocity profile. At the ebb, the fresher water that flows in the surface eventually displaces the saltier water beneath; thus, stratification increases. Over the period of ebb events, the vertical salinity

difference increases, but may briefly decreases owing to the mixing at maximum current before increasing again in low water. During the flood tide, the vertical velocity difference diminished the stratification and disappeared at the time of high water levels.

Advancements in measurement technology and numerical models have provided greater opportunities to understand the influence of tidal straining in various environments. San Francisco Bay [11,12], Guadiana Estuary [13], Wadden Sea [14], and Indus River Estuary [15], to name a few, were examples of sites where tidal straining was found to be influential. In fact, at numerical study conducted by Burchard and Hetland [16] revealed that tidal straining is twice as influential as gravitational circulation to estuarine circulation, confirming the previous work by Burchard and Baumert [17] which suggested tidal straining as one of the major, if not the most influential, dynamics that control the stratification and estuarine circulation.

The interaction between river runoff and tidal current is known to affect each other [18,19]. However, the influence of these interactions on estuarine circulation has only recently been investigated. When analyzing the circulation of Changjiang River Estuary, Pu et al. [9] took into account the influence of freshwater input to the potential energy anomaly as "river effect". Similar to tidal straining, the river effect is also generated by vertical velocity shear in river flow. The vertical velocity shear was a product of bottom friction in the longitudinal direction. The shear velocity, then, affects the density gradient in a manner similar to that of tidal straining. However, because the freshwater only flows downstream, the river effect will only enhance stratification in the estuary.

Estuarine circulation and mixing are also significantly affected by the lateral dimension as a result of the lateral structure of the longitudinal flow and lateral advection [8]. In channelized estuaries, the lateral baroclinic forcings, due to the cross-channel density gradient, induce a lateral circulation [20] which converges at the surface during flood and diverges at ebb. This lateral circulation is also known as the secondary flow. In irregularly shaped estuaries, such as meanders, the strength of the secondary flow is also influenced by lateral velocity shear due to vertical differences in centrifugal force magnitude [21]. Hence, in meandering estuaries, the secondary flow is set up by a local imbalance between the barotropic pressure gradient, centrifugal acceleration, and the baroclinic pressure gradient [22,23]. Even though the secondary

flow can introduce mixing, as suggested by Nunes and Simpson [20], the flow may also lead to re-stratification of the water column owing to lateral straining as demonstrated by Scully and Geyer [24]. Furthermore, secondary flow has a tendency to be more influential during flood than tides [25], which in turn introduces asymmetry in the longitudinal momentum balance.

Apart from the estuarine circulation, the interaction between tides and river runoff, along with the friction due to bathymetry, can also result in temporal and spatial variation in the water level in the estuary. Speer and Aubrey [26] demonstrated the nature of tidal distortion owing to the propagation of tides into shallow estuarine system. Shallow water interaction produces overtides and compound tides, with M2 overtides dominating the nonlinearity of the estuary. Furthermore, the topography of the estuary also induces tidal current asymmetry between ebb and flood tides [27], and different patterns of asymmetry can be expected from different estuarine topographies. River discharge can significantly influence propagating tides by altering tidal energy, decreasing tidal amplitude and its range, and delaying wave propagation [28,29]. With the tides propagating upstream, all these distortions increase in importance, until the point at which the propagating tides start to rapidly decline [30]. Additionally, the interaction between river and tide induces subtidal (averaged over a diurnal period) water level that increases into the upstream until the point where the tidal influence becomes extinct [31].

Similar to tidal straining, the advancement of measurement techniques has helped to widen the scope of knowledge on the interactions between river and tide, particularly on the subject of subtidal water level fluctuation. One study in the St. John River, Florida [32], reported that subtidal waves that propagate upstream experience attenuation due to the interaction with river discharge, with higher discharge causing higher attenuation. By solving all the terms in the subtidal momentum balance, Buschman et al. [33] demonstrated that subtidal water levels are affected by subtidal friction. Subsequently, subtidal friction was decomposed into contributions by residual flow, river-tide interactions, and tidal asymmetry. Even though river discharge is only explicitly dominant in the subtidal friction generated by residual flow, Sassi and Hoitink [34] reported that all three subtidal frictions terms were affected by river discharge. Because each subtidal friction terms is closely associated with the strength of forcings from the river and ocean, the

magnitude of each term will vary longitudinally, with the residual flow term tending to be stronger in the landward direction and opposite in the other two terms [35].

1.2.2 Human intervention to estuaries

Since the 20th century, the significance of human activities on our planet have grown gradually up to the point that they have become a primary driver in modifying the earth system by forcing abrupt physical, chemical, and biological changes in the environment, including estuaries [2,36]. A long-term study of water level and historical records of bathymetry in Venice Lagoon revealed that morphological changes, due to multiple human constructions, that occurred in the last century induced an increase in the amplitude of major tidal constituents along with shifting in tidal asymmetry [37]. Even more, another study in the Ganges-Brahmaputra-Meghna Delta, indicated that the effects of tidal amplification from human intervention in estuarine and coastal areas can be more influential than by sea level rise [38]. Hence, for better management strategies, basic knowledge of estuarine dynamics in specific cases and general implications are required.

In the 20th century, almost all Europeans estuaries were modified to facilitate transportation by larger ships to ports situated closer to the hinterlands [39]. Hence, the most well-documented human intervention in estuarine studies is channel deepening due to dredging which induces amplification of the tidal amplitude. Channel deepening prominently induces tidal amplification when a tidal wave propagates upstream. Examples include Elbe, Ems, Loire, Scheldt [40], Tampa Bay [41], Cape Fear [42], the Hudson River [43], and the Pearl River Delta [44]. The channel deepening also led to the reduction of hydraulic drag which shifts the SPM trapping location landward [45] and might create a feedback loop that continuously alter tidal and sediment dynamics. Similarly, a lower hydraulic drag leads to an increase in storm surge propagation [42]. Despite the increased risk of storm surge, the risk of major flooding due to high river discharge is reduced by more effective flood water conveyance [43]. Additionally, channel deepening also induces an increase in estuarine circulation, although not as significant as the monthly-to-seasonal variability due to river discharge and tides [41,46,47].

Although not as comprehensive as channel deepening, several others human activities and their effects on estuaries have been documented.

a) Reclamation

Reclamation weakens regional flow intensity and induce shoal acceleration, which subsequently significantly reduces intertidal volume [48,49]. Additionally, reclamation creates and increases local channel convergence, leading to the longer duration of tidal asymmetry [50].

b) Channel closure

A numerical study of the Modaomen Estuary revealed that the closure of the estuarine channel can reduce saltwater intrusion [51]. Another study in the Rhine-Meuse Estuary showed a decreased tidal amplitude when an estuarine channel was closed [52].

c) Large embankment

Large embankment decreases the tidal prism, enhances sediment accumulation, and continuously decrease local intertidal volume [53].

d) Dam construction and operation

The study of the impacts of the operation of the Three Gorges Dam on the Yangtze River estuary shows that the spatiotemporal pattern of river-tide interaction is sensitive to the freshwater regulation of the dam [54]. Additionally, Wei et al. [48] showed that dam operation can alter the sediment dynamics in estuaries, leading to either shoal erosion or accretion, relative to the local condition of the estuary.

e) Storm surge barrier

Generally, this barrier prevents a large portion of tidal energy from propagating further into the estuary [55,56]. This blockage led to a reduction in tidal amplitude, a decrease in current velocity, and eventually weakened tidal mixing. Weak water exchange, subsequently, enhances the stratification in the estuary.

f) Dikes

The implementation of dikes in estuaries increase the salinity in the estuary, although the variance in salinity and water mixing is weakened. However, according to a numerical simulation study of the Changjiang Estuary, the effect of dikes on saltwater intrusion may vary under different weather conditions [57].

g) Small-scale structure

Liu et al. [58] presented a 3D model to analyze the impact of small-scale structures (1m x 2m bridge pilings) in large numbers. These structures did not have a significant impact on the interest area overall. In the near-field, these structures affect local mixing and local-scale flow and may also have a significant impact on water quality and sedimentation.

1.3 Research Novelties and Objectives

Human activities can play a dominant role in the state of equilibrium in estuaries by modifying one or more forcings that play an active role in these environments. Previous studies have shown that different artificial engineering projects may have varying effects on local estuaries. Although it seems that such studies resemble case-specific studies based on research sites, this may not be the case. Certain engineering projects have general implications that can be applied to various estuaries. Examples can be found in cases that include channel deepening and storm surge barriers, in which they generate tidal amplification and reduce tidal energy in different estuaries. The Ota River Estuary in Hiroshima provides an ideal and unique location for conducting studies on the influence of artificial engineering project on estuaries. Even though the estuary has undergone various engineering interventions [3], one major engineering intervention that not only affect the circulation in the estuary, but also the socioeconomics of the Hiroshima metropolitan area, is the Ota Diversion Channel. The freshwater runoff into the channel is regulated by a set of sluice gates. These gates have effects similar to those of river damming [54]. However, instead of the usual damming situated far upstream of the river, these sluice gates affect the circulation from areas where salinity intrusion is still relatively strong. Additionally, the Diversion Channel features variation in its along-estuary

topography, which so far has received little attention on how this variation affects estuarine circulation [8]. Therefore, the effects of the flood control structure and longitudinal variation in topography on spatial and temporal flow patterns, salinity and the underlying hydrodynamic mechanisms in estuaries need to be clarified. Tracing these variations is important for achieving a basic understanding of estuarine hydrodynamics under regulated river runoff conditions. Furthermore, the obtained knowledges can also provide new insights into the management of estuaries, particularly on policies regarding the construction of flood control structures and flood diversion canals in such environments.

Accordingly, the main objectives of this study can be defined as follows.

    a)   To understand the response of the longitudinal and lateral estuarine circulation to the existence of a flood control structure and examine the underlying mechanism that controls the circulation.

    b)   To characterize the effects of longitudinal variations in channel topography on circulation and mixing in an estuarine channel.

1.4 Study Area and Research Methods

1.4.1   Study area

The Ota River is a network of estuarine river branches that flow through Hiroshima City, Japan. The westernmost branch is called the Ota Diversion Channel (Fig. 1.1) which connects the Ota River directly to Hiroshima Bay and has a high tidal range of approximately 4 m [3]. The tidal compartment in the estuary stretches 13 km upstream from the river mouth. However, a set of sluice gates known as the Gion Flood Gate, separates the upstream part of the Ota River from its coastal counterpart. It consists of three sluice gates that allow only ~10% of freshwater discharge under normal condition to flow into the Ota Diversion Channel [59]. Hence, the Ota Diversion Channel could be considered as semi-closed estuarine channel in which the existence of an obstacle that blocks most of the freshwater discharge might further increase the complexity of the estuarine circulation within the channel. The length of the Ota Diversion Channel is about 9 km in total with a width ranging from 110 m near the Gion Flood Gate to 450 m in its river mouth. The average depth of this estuarine channel is 3 m, and it can be categorized as a tidal-dominated estuary.

Meanwhile, the salinity structure of the Ota Diversion channel is varies with the changing tidal phases because it is well mixed during the flood and strongly stratified on ebb [60].

Figure 1.1 The Ota River Estuary.

1.4.2   Research Methods

Field observation campaigns and a numerical model were utilized to conduct this study. Two field campaigns were conducted during from November 23, 2018, to December, 7 2018, in the Ota Diversion Channel to capture the spatiotemporal variation of water depth, salinity structure, and estuarine circulation. During the observational campaigns, data on the water current, salinity, temperature, and water depth were collected. Regarding the numerical simulation, the author applied a 3D model from Delft3D to examine the lateral circulation in the Ota Diversion Channel.

Chapter 2 presents the influence of the flood control structure on the lateral flow in the Ota Diversion Channel. In this study, a 3D hydrodynamic model from Delft3D is implemented. The inputs of the

numerical simulation include the river discharge from the Ota River and tides at the river mouth. Both inputs were obtained from the Yaguchi and Kusatsu gauging stations of the Ministry of Land, Infrastructure and Transportation. The simulation was validated using observational data from November 23 to December 7, 2018. Furthermore, the flow structures were analyzed on both the longitudinal and lateral dimensions as well as stratification to discuss the modification of the governing mechanisms of lateral circulation due to the flood control structure.

Chapter 3 examines the response of estuarine circulation and mixing to longitudinal variation in channel geometry. The relative stability of the water column was analyzed using the Brunt-Vaisala frequency and gradient Richardson number. A potential energy anomaly was implemented to examine the stratification in the Ota Diversion Channel. Furthermore, to identify the dynamics that control the flow and stratification in the channel, the author applied the time derivative of the potential energy anomaly presented by Pu et al [9].

Chapter 4 discusses the effect of freshwater discharge regulations on the subtidal dynamics in an estuarine channel. The dominant tidal processes were analyzed using spectral and harmonic analyses. Subsequently, the decomposition of subtidal friction and Stokes flux analyses were performed to examine the governing mechanism of subtidal variation and transports in the Ota Diversion Channel.

1.5 Research Outline

The main objective of this study was to examine the estuarine circulation in the Ota Diversion Channel, which is affected by the flood control structure and longitudinal variation in channel geometry. A detailed discussion of the governing mechanism involved in this study is presented in the following three sections. The last chapter of this document, hence, presents the conclusions of this study and recommendations for future research.

In Chapter 2, the author implements a three-dimensional hydrodynamic model to investigate the lateral flow in the Ota Diversion Channel. The main purpose of this chapter is to identify the lateral flow patterns

and their underlying mechanisms due to the influence of the flood control structure. This chapter was reproduced with minor changes from *Gusti, Gillang Noor Nugrahaning, and Kiyosi Kawanisi. 2020. "The Influence of Flood Control Structure on Secondary flow Dynamics in a Meandering Tidal Estuarine Channel". Journal of Japan Society of Civil Engineers, Ser. B1 (Hydraulic Engineering) 76(2): I_1393-I_1398. https://doi.org/10.2208/jscejhe.76.2_I_1393.*

In Chapter 3, observational data are utilized to investigate the influence of variation in longitudinal channel geometry on the spatiotemporal variation of the current flow and salinity structure. The main purpose of this chapter is to quantify estuarine dynamics and the alteration of its governing mechanisms due to longitudinally varying channel geometry. This chapter has been reproduced with minor changes from *Gusti, Gillang Noor Nugrahaning, Kiyosi Kawanisi, Mohamad Basel Al Sawaf, Faruq Khadami, and Cong Xiao. 2023. "Investigating Tidal River Dynamics in a Longitudinally Varying Channel Geometry". Continental Shelf Research, 253, 104901. https://doi.org/10.1016/j.csr.2022.104901.*

In Chapter 4, the variation in subtidal dynamics under limited river runoff is discussed using by utilizing observational data. Furthermore, this chapter presents the patterns of subtidal friction and transport under limited freshwater discharge. This chapter has been reproduced with minor changes from *Gusti, Gillang Noor Nugrahaning, Kiyosi Kawanisi, Mohamad Basel Al Sawaf, and Faruq Khadami. 2022. "Subtidal Dynamics in a Tidal River with Limited Discharge". Water, 14, 2585. https://doi.org/10.3390/ w14162585.*

Finally, the summary of this study and recommendations for future works are presented in Chapter 5.

CHAPTER 2: The Influence of Flood Control Structure on Secondary Flow Dynamics in a Meandering Tidal Estuarine Channel

2.1 Introduction

Secondary (transverse) flow could be distinguished as the flow that emerges in the direction normal to the primary (along channel/streamwise) flow. The primary flow is usually concluded as the depth-averaged flow in a single velocity profile [61]. Secondary flows in meanders, including curvature-driven and topography-driven secondary currents, have been considered to be primarily responsible for redistributing or shifting the primary flow. Although the magnitude of secondary flows is an order below primary flows, it has been reported that the streamwise dynamics and dispersion processes in estuaries can be affected by weak secondary flows that act on axial gradients in salt and momentum [62].

In saline environments such as estuaries, secondary flow plays a major role in estuarine dynamics by redistributing momentum and scalars across an estuarine channel faster than turbulent motions. Secondary flow is set up by a local inequilibrium between an inward-directed barotropic pressure gradient and an outward centrifugal acceleration [63]. The inequilibrium was generated by the difference in depth-dependency between centrifugal accelerations and pressure gradient, in which the former is depth-dependent, while the latter is depth-independent. Furthermore, secondary flows are further enhanced by stratification because cross-stream shears must increase with de-creasing viscosity to generate the vertical stress divergence required to achieve a steady cross-stream flow [23]. Thus, this leads to the importance of the addition of lateral baroclinic pressure gradients to the balance.

The balance of secondary flow in a natural tidal-affected environment has been relatively well explained by previous studies. However, studies on the balance of secondary flow in hu-man-affected environments, such as a tidal channel with a flood control structure, has received little interest. Herein, the purpose of this study is to comprehend the dynamics of secondary flow in a tidal estuarine channel that is affected by a flood control structure during different tidal phases. Hypothetically, the existence of flood control could

induce more complex estuarine dynamics, thus leading to the alteration of the balance of secondary flow and vice versa, which are yet to be proven. Therefore, it is hoped that this study could contribute into giving the initial understanding of the influence of man-made structures on the governing dynamics of secondary flow in estuarine environments.

2.2 Field site and Methods

2.2.1   Field site and measurement program

The Ota River is a network of estuarine branch rivers that flow through Hiroshima City, Japan. The westernmost branch is called the Ota Diversion Channel (ODC), as shown in Fig. 2.1, which connects the Ota River directly to Hiroshima Bay, which has the maximum tidal range of approximately 4 m [3]. However, a flood gate is located in the upstream end of ODC. The gate separates the water bodies from the upstream section of Ota River with its coastal counterpart. It consists of three sluice gates that only allow ~10% of freshwater discharge under normal conditions to flow into ODC [59].

A measurement program was conducted in the upstream section of ODC near the Gion Flood Gate from November 23th 2018 to December 7th 2018. Three ADCPs were installed on the bed along a transverse line (stations A, B, and C) in one of the meanders in ODC. These ADCPs were utilized to measure the flow velocity and water level that were later used to validate the results from the numerical simulation. Two Conductivity-Temperature (CT) Sensors and a CTD were also deployed at station A, near the Kusatsu Gauging Station, and Station D, respectively, to measure salinity for calibration and giving the boundary condition to the model. Bathymetry data were obtained through the Hydrographic Survey Remote Controlled Boat (Coden RC-S3) along the Ota Diversion Channel and extended length of both the Kyu Ota River and Ota River. Hourly water levels were available from the Ministry of Land, Infrastructure, Transport and Tourism (MLIT) of Japan at Kusatsu (seaward end of Ota Diversion Channel) and Misasa Bridge (Kyu Ota River) Gauging Stations. Meanwhile, hourly river discharge (water level) was obtained through an-other MLIT at the Yaguchi Gauging Station.
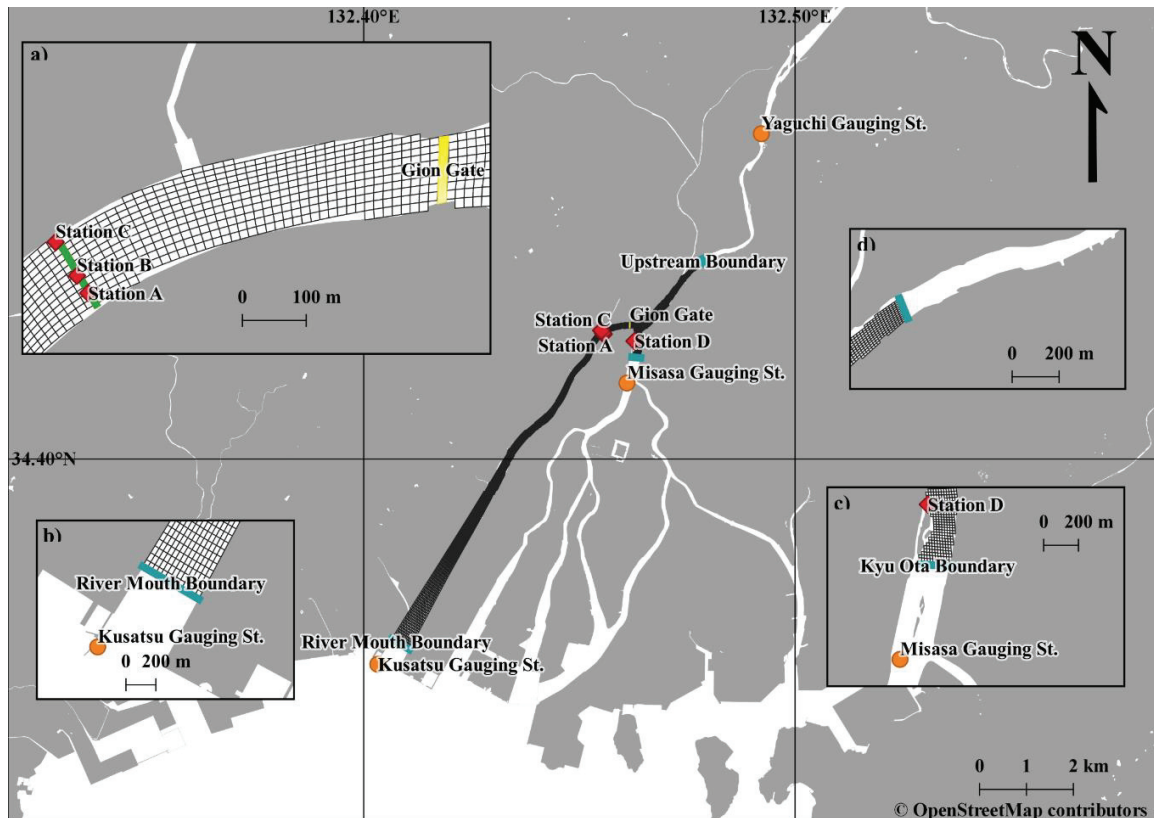
Figure 2.1 Map of the Ota River Network and the computational domain of the study (gridded area). Inset a) depicts the location where Gion Gate (yellow line), Stations A-D (red diamonds), Observational Cross-section (green line) which lied in parallel with Stations A-C, were situated. Insets b), c), and d) show the computational open boundaries (blue lines) of Kusatsu river mouth, Kyu Ota, and the river upstream, respectively. The MLIT Gauging Stations are depicted by orange circles.

2.2.2   Numerical Simulation

Delft3D runs the numerical hydrodynamic system by solving the unsteady shallow water equations that consist of horizontal momentum equations, continuity equations, and transport equations for conservative constituents. It uses two types of vertical grids in its simulation: the σ-coordinate system (σ-model) and the Cartesian Z coordinate system (Z-model). Delft3D, which also employs a quasi-3D model for its calculation, is proven to be able to simulate the secondary flow in meandering river according to Parsapour-Moghaddam and Rennie [64]. Considering the numerical advantages and its robustness to simulate the

hydrodynamics of a tidal-driven environment, Delft3D is adequately suited to simulate secondary flow dynamics in the Ota Diversion Channel.

Three open boundaries, as shown in Fig. 2.2, were applied in this model for convenient of interest area and availability. One was situated in the upstream part of the domain are near the Yaguchi Gauging Station. This upstream boundary is specified by an hourly series of river discharge and a constant salinity of 0. Another two were specified by an hourly series of water levels and situated in the extended part of the Kyu Ota River and at the river mouth close to Kusatsu Gauging Station. A constant salinity of 2 ppt was applied at the boundary of Kyu Ota as it was taken from the average salinity of CTD measurements in the Sta-tion D. Meanwhile, an hourly series of salinity was applied at the river mouth boundary from the CT Sensor measurement that was deployed in Kusatsu Gauging Station.

The computational grid cells in this study are set to correspond to the bathymetry and geometry of riverbanks. The maximum number of grid cells in the M and N directions (longitudinal/streamwise and lateral, respectively) are 362 and 58 depending on the topography of the river. The lateral resolution varies from 7.5m to 33m. On the other hand, the longitudinal resolution is slightly more diverse from those of the lateral with the highest resolution set at 13m and the lowest at 65m. Since this study focuses on the meandering area of Ota Diversion Channel, the numerical model has higher resolution grid cells in both orientations.

In this model, 10 vertical σ layers were defined with the composition of layer thickness increasing from below (2%) to top (20%). The model was run for 24 days from November 14th to December 7th 2018 and the early 1 week simulation was used as the run-up time for the model. The influence of the Gion Flood Gate was taken into account by defining a Current Deflective Wall (CDW) in the input of Delft3D that blocks 90% of the water flow. Two different scenarios, with flood gate (Scenario I) and without flood gate (Scenario II), were simulated to allow the authors to compre-hend the effect of flood gate existence on sec-ondary flow dynamics in a tidal estuarine channel. In order to determine the performance of the 10 vertical σ layers, a sensitivity test was also con-ducted by simulating a 20 vertical σ layers with same parameters only for Scenario I.

2.2.3   Evaluation Statistic Index

In studies that involve or make use of numerical models, there is always an essential need to compare their results with real measured data. This step, which is often called verification or validation, is needed to confirm the consistency of the model with measured data and to establish greater confidence in the capability of the model. Herein, the Pearson product-moment correlation (r) was applied particularly for water level, flow velocity, and salinity. The formula, which followed the expression that presented in de Pablo et al. [65], can be written as:

$$r = \frac{\sum_{i=1}^{n}(M_i - \overline{M_1})(O_i - \overline{O_1})}{\sqrt{\sum_{i=1}^{n}(M_i - \overline{M_1})^2}\sqrt{\sum_{i=1}^{n}(O_i - \overline{O_1})^2}} \tag{2.1}$$

M_i and O_i are the simulated parameters and observed parameters for the i-th time at a certain location, the overbar refers to the time-averaged values of simulated parameters. while n is the total observation time divided by 10 s as the interval time of data measurement. The correlation coefficient ranges from -1 to 1 with a positive value indicating a linear relationship, a negative value for an inverse relationship, and 0 indicates no correlation.

2.3 Results and Discussions

In order to analyze the secondary flow dynamics, a cross section shown in Fig. 2.1a was chosen as the site to record the three-dimensional velocity flow fields in the meandering section of the Ota Diversion Channel. The analysis here is done by the data taken during the flood and ebb for spring and neap tides (November 26th for spring tide and December 2nd for neap tide).

2.3.1   Model Evaluation

The Pearson correlation of was utilized to conduct model evaluation and sensitivity test. salinity was calculated at Station A, while values of water level and along-channel velocity were obtained by averaging the correlation values at stations A, B, and C for both procedures. Since the Gion Flood Gate was never

fully opened, only results from Scenario I, which were sufficient to be evaluated here. The Pearson correlations of these three parameters are shown in Table 2.1. Pearson correlations of water level, salinity, and along-channel velocity show 'strong', 'moderate positive', and 'good' correlations respectively. Therefore, it could be said that the results of simulation can represent the hydrodynamic conditions of the Ota Diversion Channel fairly-well. On the other hand, the results of sensitivity test are shown in Table 2.2. The correlation values of all parameters show 'strong' correlations between 10 and 20 vertical σ layers models with same parameters. The increase of the number of vertical layers is supposed to increase the accuracy of numerical simulation. However, the results of sensitivity test prove that 10 vertical σ layers is sufficient to simulate the hydrodynamic conditions of the Ota Diversion Channel.

Table 2.1 Person correlation values for simulation with flood gate.

Parameters	Pearson Corr.
Water level (m)	0.99
Salinity (‰)	0.59
Along-channel velocity (m/s)	0.74

Table 2.2 Person correlation values for sensitivity test.

Parameters	Pearson Corr.
Water level (m)	0.99
Salinity (‰)	0.97
Along-channel velocity (m/s)	0.98

2.3.2 Streamwise and Secondary Flow Structures

Fig. 2.2 shows the structure of streamwise and secondary velocity in the meandering section of the Ota Diversion Channel for both scenarios during flood and tide events at spring tide and neap tide. The omission of the sluice gate leads to stronger streamwise flow because the obstacle that blocked water flow has been removed, although it is less obvious in the case of ebb events. On the other hand, it appears that streamwise

velocity tends to form a high-velocity cell in the outer part of the meander that has deeper bathymetry regardless of the tidal phase. This could be addressed as a result of the geomorphology of the river, which allows the alteration of streamwise flow structure along the curvature [66].
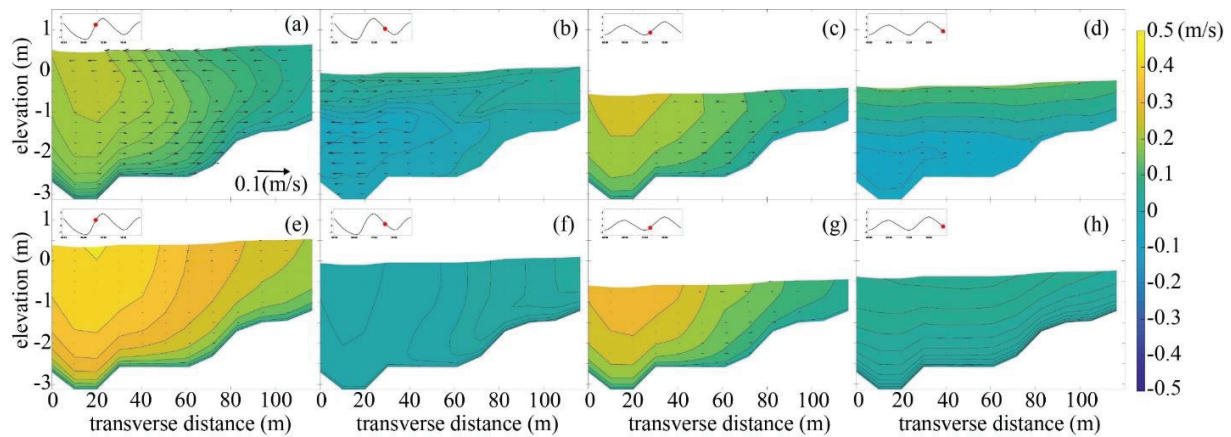
Figure 3.2 Secondary velocity (black arrow) and streamwise velocity (colored shading) with flood gate (first row) and without flood gate (second row). Each column represents the spring tide flood event, spring tide ebb event, neap tide flood event, and neap tide ebb event, respectively from left to right. The x-axis indicates the distance from the outer bank (left side) to the inner bank (right side). Positive values of streamwise velocity indicate the landward direction, while negative values indicate the seaward direction. These figures are landward oriented. Black lines along the figures denote areas with the same streamwise velocity.

On the other hand, the secondary flow was most apparent during the spring tide in Scenario I. The secondary flow during a flood event (Fig. 2.2a) represents the classic two-layer circulation flow [23] with outward surface velocity and inward velocity in the deeper part. During the ebb event (Fig. 2.2b), secondary flow pattern is reversed in the deeper section of the meander, while in the shallower section it has a similar pattern to the previous flood, albeit with weaker flow. Therefore, it creates an unobvious convergence zone in the middle section of the meander close to the surface. During neap tide (Fig. 2.2c and Fig. 2.2d), the secondary flow is in small magnitude with flood event omits a clearer secondary flow than the ebb event. In Scenario II, the secondary flow is minimum for flood events and close to non-existent on ebb events. Thus far, it could be said that the existence of a flood gate induces stronger secondary flow even though the streamwise velocity is faster in the scenario without flood gate.

2.3.3 Stratification Conditions

The salinity stratifications of the observed cross-section in both scenarios with different tidal phases are presented in Fig. 2.3. During the period of flood (Fig. 2.3a and Fig. 2.3e), fresher water was observed in the whole cross-section area in both scenarios with the salinity of the water was being slightly higher in Scenario II. Meanwhile, laterally stratified flow is observed on the flood of neap tide for both scenarios. More saline and heavier water flow is observed in the deeper section of meander along with higher streamwise flow and less saline water is observed in the shallow section of the meander (Fig. 2.3c and Fig. 2.3g). On the other hand, the ebb events of both scenarios omit different structures of salinity. Scenario I (Fig. 2.3b and Fig. 2.3d) induces strong vertical stratification with greater salinity throughout deeper depth, which in accordance with Kawanisi [60]. At the same time, Scenario II (Fig. 2.3f and Fig. 2.3h) produces well-mixed conditions with high salinity water. Accordingly, it could be deduced that the existence of the sluice gate creates a clear lateral distinction of the salinity across the observed cross section. The omission of the flood gate induces a stronger streamwise flow that could lead to further intrusion of saline water into the upstream. Since its resistance has been removed, the same thing also happens during ebb tides in which freshwater flow down further downstream in the Ota Diversion Channel. Thus, it leads to well-mixed conditions in the meandering part of the Ota Diversion Channel in Scenario II.
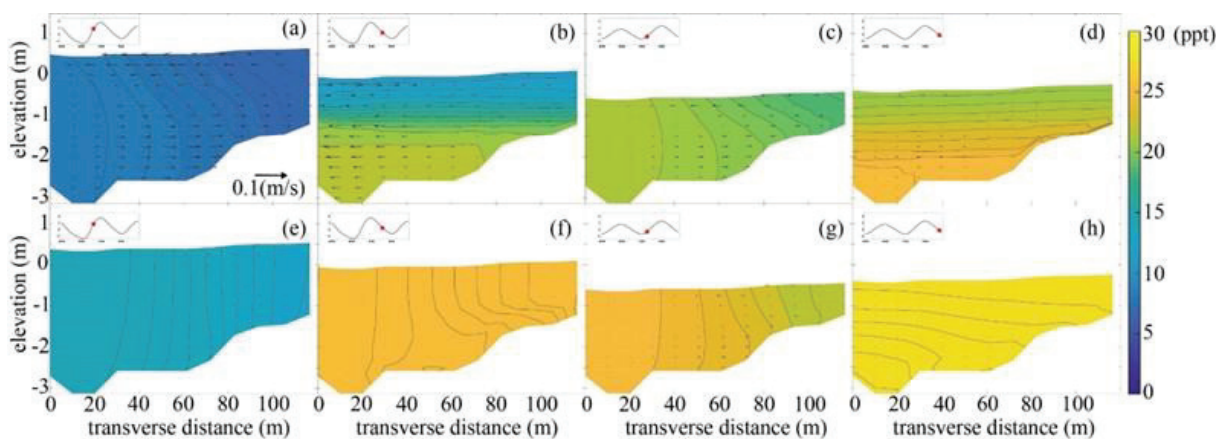
Figure 4.3 Secondary velocity (black arrow) and salinity (colored shading) with flood gate (first row) and without flood gate (second row). Each column represents the spring tide flood event, spring tide ebb event, neap tide flood event, and neap tide ebb event, respectively from left to right. The x-axis indicates the distance from the outer bank

(left side) to the inner bank (right side). These figures are landward oriented. Black lines along the figures denote areas with the same streamwise velocity.

2.3.4   Governing Mechanisms of Secondary Flow

The Scenario I, which incorporates the existence flood gate, has greater secondary flow despite its spatial variation across the cross section. Thus, in order to gain further understanding of the governing mechanisms of secondary flow in the Ota Diversion Channel, the lateral momentum balance, which is presented as below, is calculated.

$$\frac{\partial u_n}{\partial t} = -u_s \frac{\partial u_n}{\partial s} + \frac{u_s^2}{R_s} - g \frac{\partial \eta}{\partial n} - \frac{g}{\rho_0} \int_z^0 \frac{\partial \rho}{\partial n} dz - fu_s$$
$$+ \frac{\partial}{\partial z}\left(A_z \frac{\partial u_n}{\partial z}\right)$$

(2.2)

where n and s show lateral and streamwise directions, respectively; u_n and u_s represent the horizontal velocity in the lateral and streamwise directions respectively; R_s the radius of curvature; ρ_0 the constant reference density; ρ the density of water; A_z indicates the vertical eddy viscosity; and η denotes the surface water level. Meanwhile, the terms within Eq. (2.2) also represent several forces that govern the pattern of secondary flow. The first term on the left-hand side is the time rate of change of secondary velocity at any vertical elevation of z. The first term on the right side represents nonlocal acceleration. The second term depicts the centrifugal acceleration. The third term denotes the barotropic pressure gradient. The fourth portrays the baroclinic pressure gradient. The fifth term is the Coriolis acceleration. The last term is the turbulent shear stress in the stream-normal direction, which is introduced by the viscosity effect. The Coriolis term could be neglected due to the scale of the estuary.

The results of the momentum analysis are presented in Fig. 2.4. The distinction between Scenario I and Scenario II is quite clear during the ebb of both the spring and neap tide. Scenario II, along with the omission of the sluice gate, leads to the smaller magnitudes of governing mechanisms than Scenario I. This could

come as a result of slow streamwise flow and well-mixed conditions that have been explained in the previous sections. During floods, the governing mechanisms are stronger in both scenarios. The baroclinic pressure gradient and barotropic pressure gradient, which are influenced by the lateral salinity gradient and water level gradient respectively, seemed to become the dominant forces. However, as it has been mentioned, the sluice gate hampers the flow of water, it should come as no surprise that the centrifugal acceleration is much faster in Scenario II. This term could be the determinant force that inflicts the difference of secondary flow in both cases. In Fig. 2.4a, the barotropic pressure gradient has positive value (higher water level near the inner bank), while the baroclinic pressure gradient has negative value (higher density near the outer bank). In surface water, the barotropic pressure gradient is dominant; thus, it induces follow that is directed toward the outer bank. In the mid-depth and near bottom, the negative baroclinic pressure gradient becomes dominant, leading to the flow toward the shallower inner bank. On the other hand, in Fig. 2.4e a negative strong centrifugal force (faster current in the outer bank) and a greater barotropic pressure gradient are observed. The centrifugal force then equalized the barotropic pressure gradient in the surface, while the baroclinic pressure gradient is stabilized by a barotropic pressure gradient near the bottom. The same mechanism could also be explained by flood events during neap tide. However, during the spring ebb (Fig. 2.4b), in which the governing forces were not as strong as those during the flood, the secondary flow was observed to be relatively strong. The inverse pattern of the secondary flow could emerged as a result of the interaction between the negative barotropic pressure gradient and positive baroclinic pressure gradient that is complemented by the viscosity effect. Thus, it could be said that great values of governing forces do not necessarily generate high secondary flows, as the governing forces may counterbalance each other.
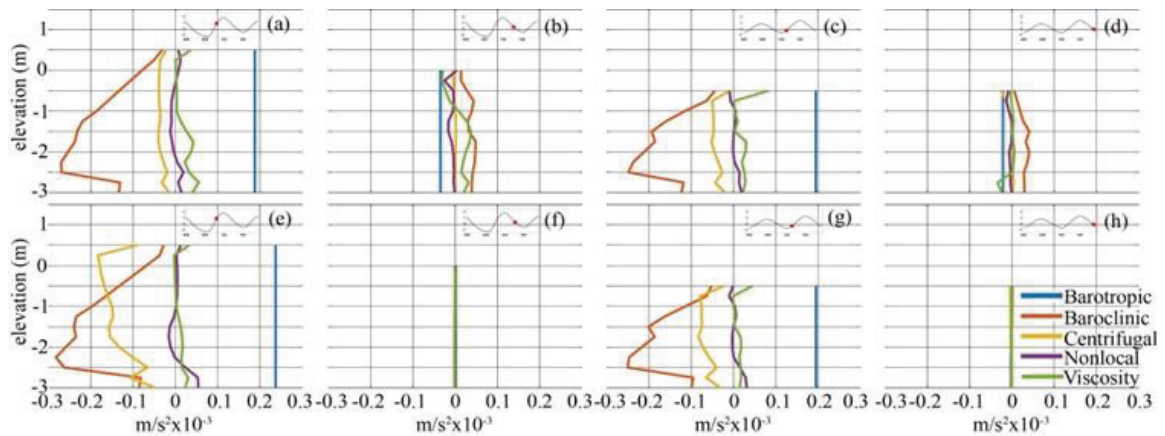
Figure 5.4 Governing forces of secondary flow in scenario with flood gate (first row) and without flood gate (second row). Each column represents the spring tide flood event, spring tide ebb event, neap tide flood event, and neap tide ebb event, respectively from left to right.

2.4 Conclusions

This work is focused on investigating the effects of flood gate on the secondary flow dynamics of estuarine channels. Numerical simulation and field observation were utilized to gain understanding on the hydrodynamic conditions of the Ota Diversion Channel. Herein, secondary flow is found to be of greater values along with the existence of the Gion Flood Gate. This is supported by the fact that the omission of the sluice gate induces faster streamwise flow as well as greater centrifugal force, which creates an equilibrium between the original dominant forces, barotropic pressure gradient and baroclinic pressure gradient. This leads to the conclusion that the existence of a flood gate indeed alters the dynamics of secondary flow in the Ota Diversion Channel, particularly in its meandering part.

CHAPTER 3: Investigating Tidal River Dynamics in a Longitudinally Varying Channel Geometry

3.1 Introduction

Tidal rivers are influenced by different factors: mainly river discharge, tides, and topography. The interaction between those factors, particularly river discharge and tides, is dominant at the downstream section of a tidal river, the definitions of which are often difficult to distinguish from those of estuaries [67]. In the last three decades, studies have revealed that tidal straining is one of the most influential mechanisms in tidal rivers and estuaries [10,11,14,16,68–73]. This mechanism involves the tidal velocity periodically straining the vertical salinity distribution in the longitudinal orientation of the channel, with stratification strengthened at the ebb tide and weakened during a flood event. Furthermore, under the influence of tidal straining, well-mixed flood currents are intensified in the bottom part of the water column, while the intensely-sheared ebb currents are more prominent near the water surface [71]. The other major process is the gravitational circulation that is thought to be induced by the longitudinal density gradient in the estuarine channel [7,8,16,74]. This mechanism generates a two-layer flow structure that varies vertically, with the less dense seaward flow in the upper half of the water column and more dense landward flow occupying the lower half. The existence of tidal straining and gravitational circulation, which affects the occurrence of mixing and stratification, has the potential to transform the circulation structure of the estuary.

Apart from the above two mechanisms, the following mechanisms have also been found to be significant in tidal river dynamics, namely tidal stirring, wind stirring, and river effect. Traditionally, tides and wind have been known to enhance stirring, which leads to mixing over the water column [10]. Although this stirring effect still holds true for tides [75], it is apparently not reciprocal for the latter stirring term. Previous studies have found that wind can enhance both mixing and stratification [76,77], which eventually introduces a wind-straining mechanism [78,79]. On the other hand, the river effect, which was first introduced by Pu et al. [9], refers to the mechanism that is generated by the interaction of river-induced

velocity shear and the longitudinal density gradient. This shear can affect the tidal river circulation, similarly to tidal straining. Eventually, these mechanisms add more complexity to the dynamics of tidal rivers.

Tidal rivers and estuaries around the world are not longitudinally identical and have some distinct features, such as curves, headlands, and sills [8]. Consequently, in recent years, many studies have investigated the effects of distinct geographical settings, particularly channel curvature [14,61,63,68,80–88]. Some of these studies have shed light on the influence of curvature on longitudinal estuarine dynamics. Becherer et al. [14] and Becherer et al. [68] introduced a strong alteration in circulation along the channel, which was generated by curvature-induced tidally asymmetric lateral circulation. Furthermore, Pein et al. [61] compared two idealized estuarine channels for curved and straight channels through numerical simulations. From this simulation, they found that the curvature significantly altered the longitudinal estuarine dynamics by converting up to 30% of the along-estuary momentum into lateral circulation compared to an estuary with a straight channel. Admittedly, most of these previous studies focused more on the effect of channel curvature on the lateral estuarine structure, with only a few available on the longitudinal estuarine structure. This lack of studies for complex hydrodynamics raises the need to pay more attention to the longitudinal dynamics of tidal rivers and estuaries, particularly through field observations of real-life tidal rivers and estuaries, to deepen our knowledge about the dynamics of estuaries that have distinct geographical settings longitudinally.

The Ota Diversion Channel in Hiroshima Japan is part of the Ota River Estuary, which is known to be affected by tidal straining in its circulation [72,89–91]. However, the striking aspect of this channel is its longitudinally varying geographical settings that consist of a curved channel in its upstream area and a straight channel in its downstream section. The strength of tidal straining and geometrical settings in this site motivate us to investigate the longitudinal estuarine dynamics in the Ota Diversion Channel, Hiroshima. The objectives of this study are: (1) to quantitatively examine the effects of longitudinally varying channel geometry on tidal river dynamics and its governing mechanisms in a single estuarine channel; (2) to

qualitatively analyze the effects of the longitudinally varying channel geometry to the longitudinal and lateral flow in the estuary; (3) to identify the influence of channel geometric difference to stratification and density distributions; and (4) to investigate the relationship between channel shape difference and tidal straining. In the following sections, we present the details of the study area and method of observations, discuss the results of the observational data analysis, and present the conclusions.

3.2 Study Area and Methods

3.2.1   Study Area

The Ota River estuary is a shallow estuarine river network that flows through the metropolitan area of Hiroshima, Japan (Fig. 3.1). The estuary has a semidiurnal mesotidal regime with a maximum tidal range of 4 m in the river mouth during the spring tide [91]. The tide can influence the dynamics in the estuary up to 13 km upstream, while the maximum length of saltwater intrusion is slightly shorter at 11 km [89]. The freshwater discharge of the Ota River separates into two major branches at approximately 9 km upstream of the river mouth. The westernmost branch is called the Ota Diversion Channel that was constructed from 1934 to 1967 to protect Hiroshima city from flooding [3]. Owing to the difference in geometry, the channel can be divided into two parts. The first part is a straight channel that spans 5 km upstream from the river mouth, and the second part is the 4 km curving channel that extends from the upstream boundary of the first part to the Gion Flood Gate.

The Gion Flood Gate is built at the upstream border of the diversion channel to control the river flow in the channel, and it is composed of three sluice gates. Yaguchi gauging station sited 5 km further upstream provides measurements to manage operations at the floodgates. During normal day-to-day operations, only one gate is opened to provide a controlled flow over the 32 m x 0.3 m cross-section that allows 10%–20% of the total discharge of the Ota River into the channel. In contrast, when the water discharge measured at the Yaguchi gauging station is greater than 400 m^3/s, all the sluice gates are completely opened, allowing approximately half of the total Ota River discharge to flow in the diversion channel.
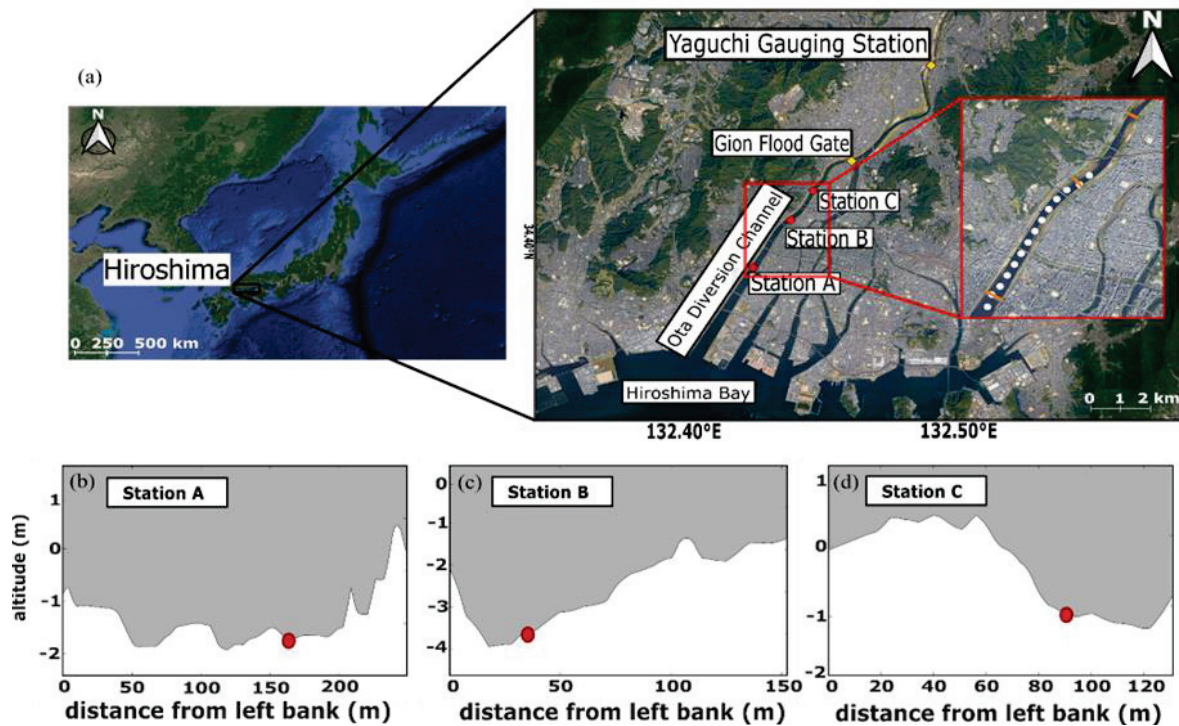
Figure 3.1 (a) Research area and observation sites in Ota Diversion Channel, Hiroshima, Japan; (b) The cross-section area of deployment station A; (c) Station B; (d) and Station C. All cross-sectional visualizations face seaward direction. Red dots show the locations of instrument deployment. White dots in the inset show the casting location of CTD probes. Yellow dots show the location of Gion Flood Gate and Yaguchi Gauging Station. Orange lines in the inset show the position of cross sections for ADCP measurements.

3.2.2   Field Measurements

Field measurements were conducted by deploying a set of instruments in the thalweg at three locations from March 16 to March 31, 2021 (Fig. 3.1). Each location has a different geometrical setting. Station A is located in a relatively straight and wide channel. On the other hand, stations B and C are located in curved and narrower channels. The degrees of curvature for each site are computed at channel longitudinal axis. Different values are obtained at ebb and flood phases in Station B because it is situated in between two counterturning curvatures (Table 1). Since it is importance to define the correct curvature degree for both flood and ebb, in this study we follow the approach by Nidzieko et al. [63]. They calculated the curvature degree by defining the angle between two radii of curvature that were situated in the bend entrance and exit. This observation covered two halves of the spring tide period (March 16 – March 20 and March 27 – March

31) and a full neap tide period (March 21 – March 26). The currents and water depth at each of these three stations were measured using upward-looking ADCPs (2 MHz Nortek Aquadopp profilers). The profiling and averaging intervals of ADCPs were 10 minutes, the cell depth was set to 0.25 m, the blank distance was 0.1m, and the bin number was 30. JFE Advantech Infinity-CT sensors (Station A) and two Alec Electronics ACT-HR (Stations B and C) were deployed along with the ADCPs to measure the time-series distribution of near-bottom salinity and temperature every 10 min.

Table 3.1 Curvature degree of each site

Site	Flood (^{0})	Ebb (^{0})
Station A	0.16	0.16
Station B	28.29	24.17
Station C	18.01	18.01

Along channel transect measurements for salinity, temperature, and water density were also conducted by casting a JFE-Advantech Rinko Profiler CTD probe. The vertical resolution of the CTD casting was set to 0.1 m for every 200 m longitudinal distance along the channel, as shown in Fig. 1a. The along channel measurements were carried out on March 24 and 31, which covered the neap and spring tide periods, respectively. During the field measurements, the discharge was estimated from the rating curve at the Yaguchi Gauging Station.

3.2.3 Data Processing

The raw current data were refined by omitting the bins above the water surface. The current data, consisting of eastward and northward velocities, were then rotated according to the orientation of the channel relative to the north direction to obtain the longitudinal velocity (u_s) and lateral velocity (u_n). On the other hand, because the data obtained at Yaguchi Gauging Station is a time series of water levels, the local rating curve equation was applied to the discharge estimation:

$$Q(0.56 \leq h \leq 1.05) = 90.78 \text{ x } (\eta + 0.156)^2 \tag{3.1}$$

where Q is the discharge (m³/s), and η is the recorded water level (m) at the Yaguchi Gauging Station. Eq. (3.1) was constructed from the observed water level and discharge data obtained from 2010 to 2019. To calculate the density at each station, we converted the temperature and salinity data using the following equation of state for seawater [92] in the ranges of $0 \leq T \leq 180°C$ and $0 \leq S \leq 40ppt$:

$$\rho = 1002.4 + 754.8S + 236.3S^2 + (-0.1338 - 0.935S - 0.0976S^2)T + (-0.003375 + 0.00996S - 0.439S^2)T^2 + (0.00000313 - 0.0000163S + 0.000244S^2)T^3 \tag{3.2}$$

where ρ is the water density (kg/m³), is S salinity (ppt), and T is the temperature (°C). We employed classic analytical approach from Hansen and Rattray [7] for density which assumes that density variations are much stronger in longitudinal field than the lateral ones. Additionally, this classic analytical approach also corresponds the potential energy anomaly [93] and its time derivation [9,10] which were used later in this study. Therefore, although continuous measurements of bottom densities by CT sensors and spatial CTD casting were only conducted along the thalweg of the channel, these density data were used to represent the respective cross-sections in this study.

The density data along the channel and current data at each station (at the same time when the CTD measurements were conducted along the channel) were used to calculate the Brunt-Vaisala frequency (N), gradient Richardson number (Ri), and potential energy anomaly (Φ) both at flood and ebb during spring and neap tides. The Brunt-Vaisala frequency, according to Wu et al. [94], can be written as

$$N = \sqrt{(-g/\rho_0)(\partial\rho/\partial z)} \tag{3.3}$$

where g denotes gravitational acceleration (9.8 m/s²), ρ_0 is the reference water density (1027 km/m³), and z is the vertical elevation (m). Physically, the Brunt-Vaisala frequency indicates the oscillation frequency at which the vertical displacement of the water body occurs around its stable density position. The flow tends to be more stable with a high value of the Brunt Vaisala frequency and less stable when the value is minimum [95].

The gradient Richardson number, which can help describe the relative stability of the flow in estuaries [94], can be defined as

$$R_i = N^2 \left(\left((\partial u_s / \partial z)^2 + (\partial u_n / \partial z)^2 \right) \right)^{-1} \qquad (3.4)$$

where $\partial u_s / \partial z$ and $\partial u_n / \partial z$ represent the vertical gradients in the longitudinal and lateral components of the flow, respectively. Previous studies indicated that the critical value of the Richardson number is $R_i = 0.25$ (e.g., [24,94]). The flow is unstable, and mixing is intensified if $R_i < 0.25$, whereas if $R_i > 0.25$, stable, and stratification is enhanced.

In addition to the Brunt-Vaisala frequency and Richardson number, a potential energy anomaly was calculated in this study. Simpson and Bowers [93] described potential energy anomalies as a measure of the degree of stratification and quantified the energy needed to mix the water column. As such, a higher value of potential energy anomaly reflects the greater energy required to break down the stratification of the water column. The equation of the potential energy anomaly can be defined as

$$\Phi = 1/d \ \int_{-h}^{\eta} gz \left(\bar{\rho} - \rho(z) \right) dz \qquad (3.5)$$

where $d = \eta + h$ denotes the total depth of the water column (m), and $\bar{\rho}$ denotes the depth-averaged density (kg/m^3).

To further examine the spatial and temporal variation of the governing mechanisms for the flow and stratification in the estuarine channel with interchanging geometry, we adhered to the time derivative of the potential energy anomaly approach, which was used by Pu et al. [9]. This approach was derived from Simpson et al. [10] for the case of the Changjiang River estuary, which corresponds to the geometrical shape of the Ota River estuary. Here, the time derivative of the potential energy anomaly [9] can be defined as:

$$\partial \Phi / \partial t = 0.035 gh\bar{u}_t (\partial \rho / \partial x) + 0.035 gh\bar{u}_r (\partial \rho / \partial x) + 0.031 (g^2 h^4 / A_z \rho)(\partial \rho / \partial x)^2 - \varepsilon k\rho (|u|^3 / h) - \delta k_s \rho_a (\overline{U_a}^3 / h) \qquad (3.6)$$

where $\bar{u}_t$ (m/s) is the depth-averaged tidal velocity, which was obtained by applying a band-pass filter to the measured velocity with a gain period of 11-30 hours, x denotes the longitudinal distance between each station (2 km), $\bar{u}_r$ (m/s) indicates the depth-averaged river velocity that was obtained from low pass-filtered measured velocity with a gain period of 30 h, A_z (m²/s) refers to the vertical eddy viscosity, k is the bottom drag coefficient (2.5 x 10-3), k_s denotes the surface stress coefficient (6.4 x 10⁻⁵), ρ_a (kg/m³) is the air density, $\overline{W}$ (m/s) is the height-averaged wind velocity, ε and δ are the mixing efficiency parameters (0.0037 and 0.0023, respectively). The first term on the right side refers to tidal straining. The second term denotes the river effect, a mechanism similar to that of tidal straining, yet it is generated by the shear from the river flow. The third term represents the gravitational circulation and longitudinal density gradients, which help maintain stratification in the estuary [7,16]. The fourth and fifth terms are tidal and wind stirring, respectively [10,76,77]. Herein, two terms were neglected from the analysis: wind stirring and gravitational circulation. The wind stirring term is negligible because it is a few orders weaker than the other terms. On the other hand, the estimation of eddy viscosity cannot be conducted in this study for two reasons: (1) the data of density vertical distribution is temporally limited and (2) the calculation of Reynolds shear stress requires current velocity data that have higher temporal resolution (i.e., profiling and averaging intervals in the order of seconds). Therefore, we could not quantify the gravitational circulation in this study.

3.3 Results

The results are separated into two subsections: velocity distributions and the spatial-temporal distributions of density. The first subsection presents the velocity time series on both the along-channel and across-channel orientations, as well as their relation to the tidal range and depth at each station. The second subsection shows the spatial and temporal distribution of density, as well as the calculation of the Brunt-Vaisala frequency, Richardson number, and potential energy anomaly.

3.3.1 Velocity Distributions

The longitudinal velocities measured at all stations are shown in Fig. 3.2. The measurements were taken on March 17 at the highest level in the first half of the spring tide and on March 24 at the lowest level of the neap tide. In general, each station shows a different pattern of tidal asymmetry between the flood and ebb. During the spring tide at Station A, the modulus of peak velocity at ebb is similar to the modulus of peak velocity at flood. The fastest flood flow occurs throughout the entire water body during the early stage of the flood tide, while the fastest ebb flow occurs consistently in the near-surface layer (the layer just below the free water surface) from the beginning until the latter stage of the ebb tide. At Station B, the ebb flow is observed to be slightly more dominant than the flood flow, which is indicated by the existence of a thin near-surface seaward flow at the beginning and the end of flood tides. The fastest seaward velocity cell at this station also shifted to the latter stage of the ebb. Furthermore, a stronger asymmetry between flood and ebb flows is found at Station C, with the appearance of seaward flow on the surface throughout the flood period, except during the mid-stage. Additionally, the longitudinal velocity at Station C seems to be more layered than at the other two stations. During the neap tide, the tidal asymmetry pattern at each station is similar to that during the spring tide, even though the tidal energy was weaker. However, one clear distinction could be observed, in which the landward flow during the flood does not occupy the entire water column. Rather, the landward flow is situated in the mid-depth and near-surface during the first and second ebbs, respectively.

Figure 3.2 Longitudinal velocity in station A (first column, panels a and b), B (second column, panels b and e), and C (third column, panels c and f). The first row (panels a, b, c) refers to measurements taken on March 17 during the spring tide, whereas the second row (panels d, e, f) refers to measurements taken on March 24 during the neap tide. The positive value denotes landward velocity and the negative value denotes seaward velocity.

Along the channel, the vertical shear of the velocity was estimated using the difference between the near-surface bin and the near-bottom bin. The near-surface bin is defined as the uppermost reliable ADCP bin in which the vertical location is temporally relative owing to the changing water level. Herein, the vertical shear of longitudinal velocity is calculated to compare the shear in the flow between the straight and curved channels. Fig. 3.3 shows the vertical shear of longitudinal velocity: $u_{sz} = (u_{ssurf} - u_{sbott})/dz$, where dz refers to the depth difference, at all stations in comparison to water depth on March 17, March 24, and in the last 24 h of observation (for the sake of convenience, we call it March 31). The shears on March 31 are limited to stations A and B due to technical problems with the ADCP transducers at Station C during the field measurements. The (+) and (-) signs of shear are relative to the orientation of the near-surface flow. However, it should be noted that the estuarine circulation in this channel is predominantly seaward (-) near

the surface and periodically changes between landward (+) during flood and seaward during the ebb near the bottom.

Figure 3.3 Vertical shear of longitudinal velocity in the station A, B, and C along with the water depth on March 17 (a), March 24 (b), and March 31 (c).

During the spring tide (Fig. 3.3a and 3.3c), the value of the vertical shear of the longitudinal velocity is found to be dominantly negative. Furthermore, the active period of the negative velocity shear is slightly different between the straight and curved channels. In the straight channel (Station A), the high velocity shear was observed from the late flood until the mid-ebb. Meanwhile, the velocity shear measured from the curving channel was observed to be of high values from early flood until mid-ebb. The longer period and greater negative shear values at stations B and C resulted from the apparent vertical variation of longitudinal flow (tidal asymmetry) in the curving channel (Fig. 3.2a and 3.2c). This agrees with Chant [62], who mentioned that high shears present evidence of stronger estuarine circulation or even two-layer circulation in the estuary.

On the other hand, neap tide induced both positive and negative vertical shear of longitudinal velocity with the tangible positive shear induced by the faster landward velocity near the water surface that is found during the second ebb at neap tide (Fig. 3.2d-f). The high negative shear in the straight and curved channels during the neap tide was found at relatively similar tidal phases. Despite the similarity, the shear in the curved channel is still consistently greater than that in the straight channel, apart from the influence of spring neap variability on the tidal flow.

Fig. 3.4 presents the lateral velocity at all stations during the spring and neap tides. Contrary to the longitudinal velocity, the lateral velocity does not seem to have clear distinctions in flood-ebb and spring-neap variabilities. However, the observed vertical distribution of the lateral velocity in the straight and curved channels shows different patterns of two-layer circulation. In the straight channel, a strong flow toward the left bank occupies the surface layer, while a weak flow toward the right bank can be seen in the bottom. Even though the cross-sectional shape of Station B, in which the thalweg is closer to the left bank, might suggest that the lateral flow at surface for ebb events must be directed toward the left bank, theoretically, the observed results (Fig. 3.4b) suggest otherwise. At Station B during the spring tide, the surface layer on both flood and ebb tides are occupied by flow toward the right bank. Besides, the lateral surface flow at ebb is stronger than at flood, with the bottom layer occupied by lateral flow toward the left bank. There are two aspects that might affect these patterns of lateral flow in Station B at spring tide namely, 1) the location of the observational cross-section which is in the bend exit relative to both flood and ebb direction, and 2) the difference in density structure between partially mixed flood (Fig. 3.7c) and stratified ebb (Fig. 3.7d). Nidzieko et al. (2009) found that the interaction between stratification and centrifugal acceleration at ebb in the Elkhorn Slough, California at stratified ebb induced strong baroclinic pressure gradient that was able to overturn the rotational sense of lateral flow to be relative to that expected in curvature at the exit of bend. At flood, the weak stratification generates classic pattern of lateral flow around the curvature, hence the lateral flow toward the right bank is also observed in Station B (Fig 3.4b). In the Station C, the lateral flow pattern, in which the surface layer is occupied by flow toward the right bank at flood, can be associated with the classic lateral flow pattern since the thalweg is close to the right bank and the observed cross-section is situated inside the bend. Additionally, the different bottom shapes between Station B and Station C could be associated with strong downstream flow during floodings since the tidal flow in normal condition in the channel may not cause large sediment transport (bed load). Furthermore, the difference in the orientation between both channels is evident in the vertical shear of the lateral velocity $(u_{nz} = (u_{nsurf} - u_{nbott})/dz)$, as shown in Fig. 3.5. The vertical shear of lateral orientation in both Stations B and C tends to be positive, while in Station A it tends to be negative.
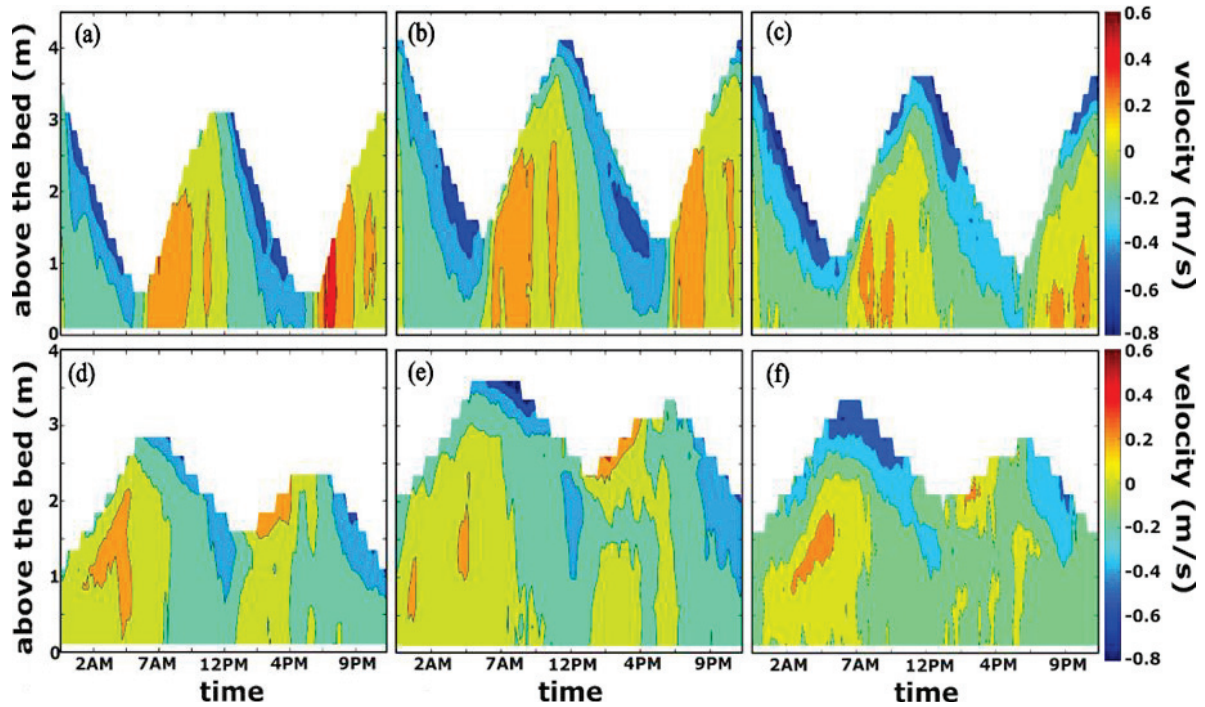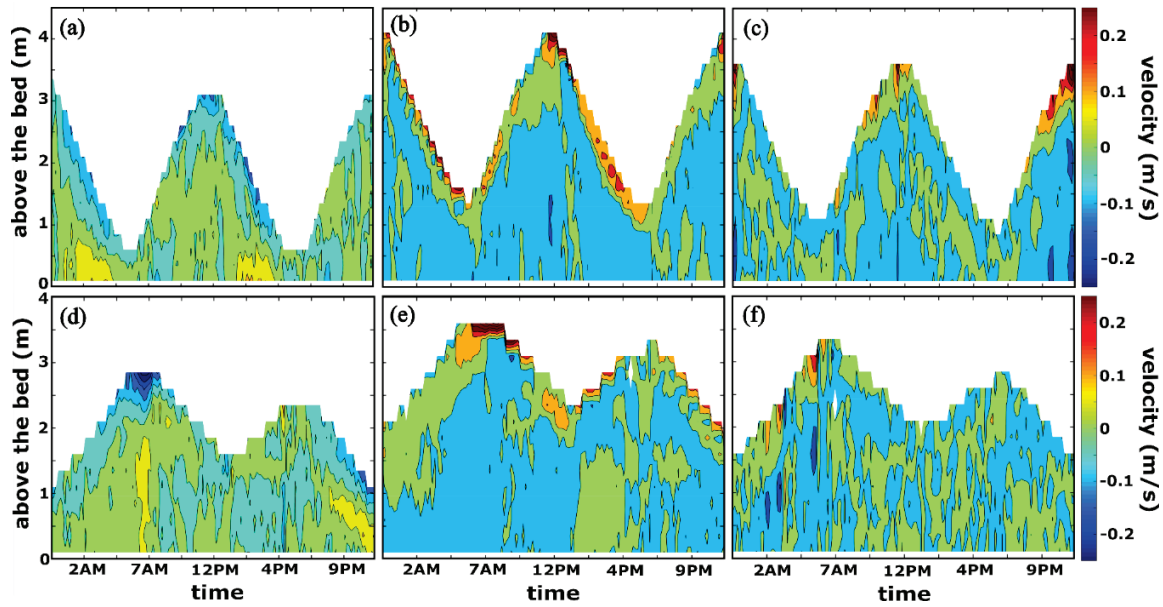
Figure 3.4 Lateral velocity in station A (fist column, panels a and b), B (second column, panels b and e), and C (third column, panels c and f). The first row (panels a, b, c) refers to measurements taken on March 17 during the spring tide, whereas the second row (panels d, e, f) refers to measurements taken on March 24 during the neap tide. The positive value denotes velocity to the direction right bank and the negative value denotes velocity towards left bank.

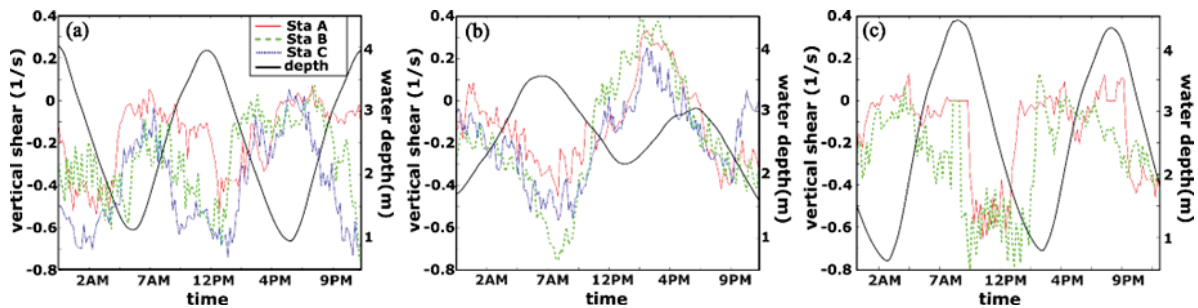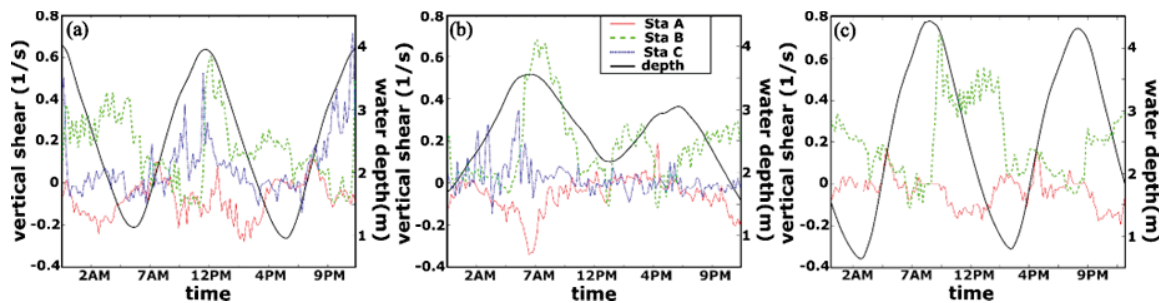Figure 3.5 Vertical shear of lateral velocity in stations A, B, and C along with the water depth on March 17 (a), March 24 (b), and March 31 (c).

3.3.2 Spatial and Temporal Distribution of Density

The time series of the near-bottom densities at each station are shown in Fig. 3.6. Temporal variations in density at these stations present distinct patterns. A periodic changes due to the tidal influence during the spring tide are observed, where the high tide induced denser water to be found at all stations and low-

51

density water at the low tide. In contrast, the densities near the bottom during the neap tide are consistently

high during the measurements. This clearly indicates the periodic changes in the water density due to tidal

straining.
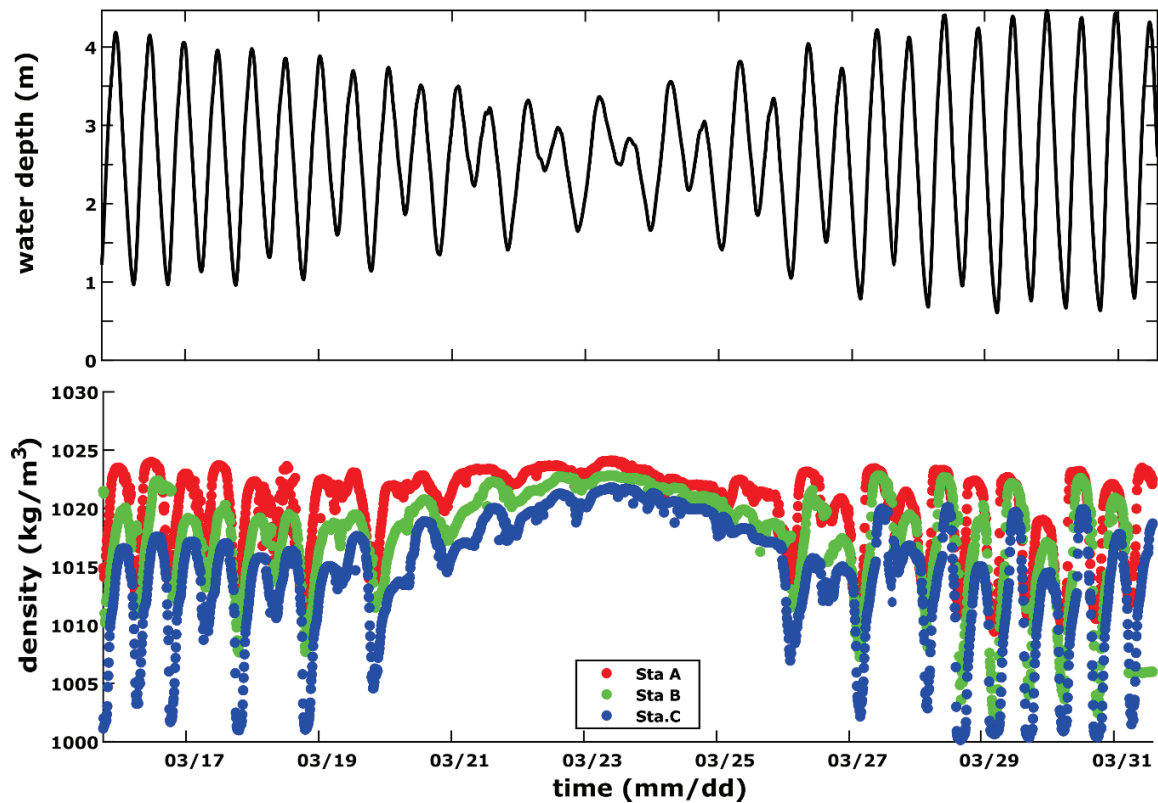
Figure 3.6 Water depth in Station A (top) and the near-bottom density measured in Station A (red dots), Station B (green dots), and Station C (blue dots) from March 16 to March 31.

Fig. 3.7 and 3.8 show the density distribution along channel and Brunt Vaisala frequency at the flood and

the ebb during the neap tide (March 24) and the spring tide (March 31), respectively. During the neap tide,

the channel is stratified with little difference between the flood and ebb. A salt wedge formation is also

observed, and the pycnocline that appears at the mid-depth in the upstream part gradually gets closer to the

surface in the downstream direction as shown by the high number of Brunt-Vaisala frequency as well. A

more striking difference in density distribution is evident during spring tide. During the flood, the channel

seems to be well-mixed, and the density gradually decreases toward the upstream part. During the ebb,

density stratification is observed along the measured channel, with freshwater occupying the near-surface water body. This indicates the existence of tidal straining, which was also mentioned in previous studies of the Ota River Estuary [72,89,90]. The periodic nature of the tidal straining yields different temporal effects. During the flood tide, the tidal straining introduces mixing between saltwater and freshwater, while at the ebb tide it induces a relatively stable stratification over the water body. Therefore, this suggests that tidal straining is greatly influenced by the strength of the tide in the channel; thus, it might vary along with the change between the spring and neap tides.
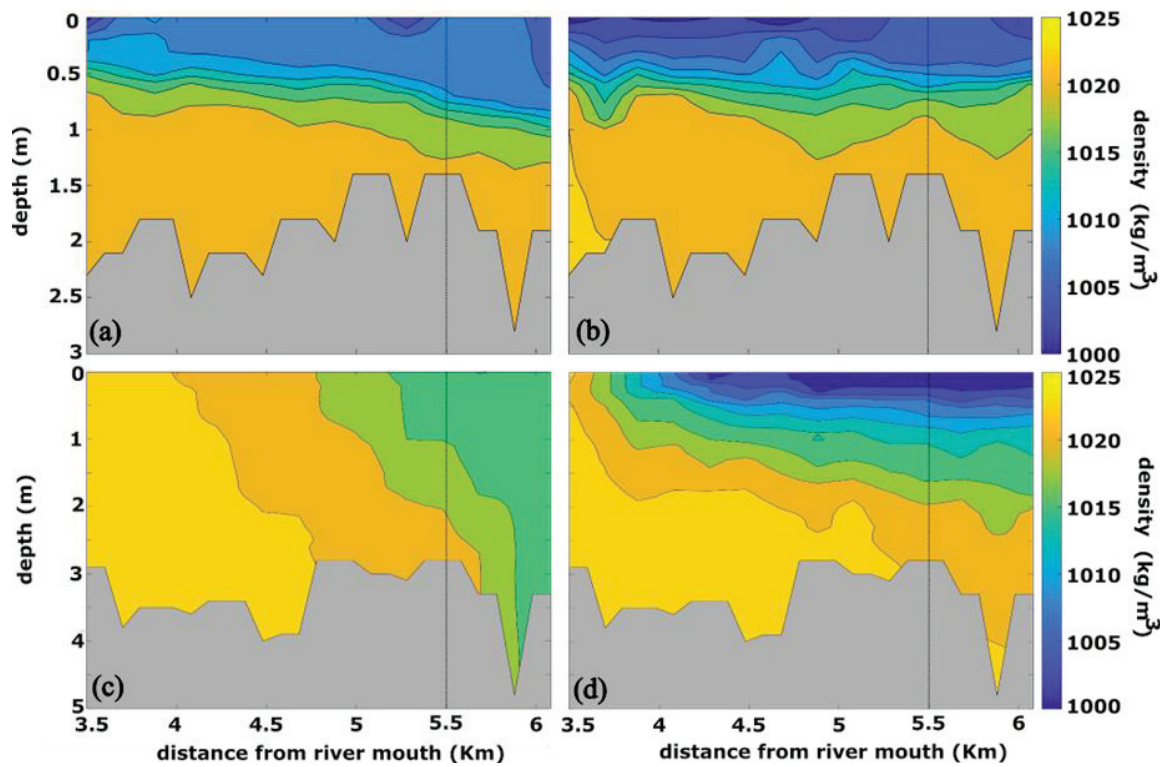
Figure 3.7 Longitudinal distribution of density at flood (first column) and ebb (second column) on March 24 (first row) and March 31 (second row). The black line indicates the start of curving channel at 5.5 km upstream of river mouth. The data were taken during the maximum flood and/or ebb flow except for (a) which was taken during early flood.
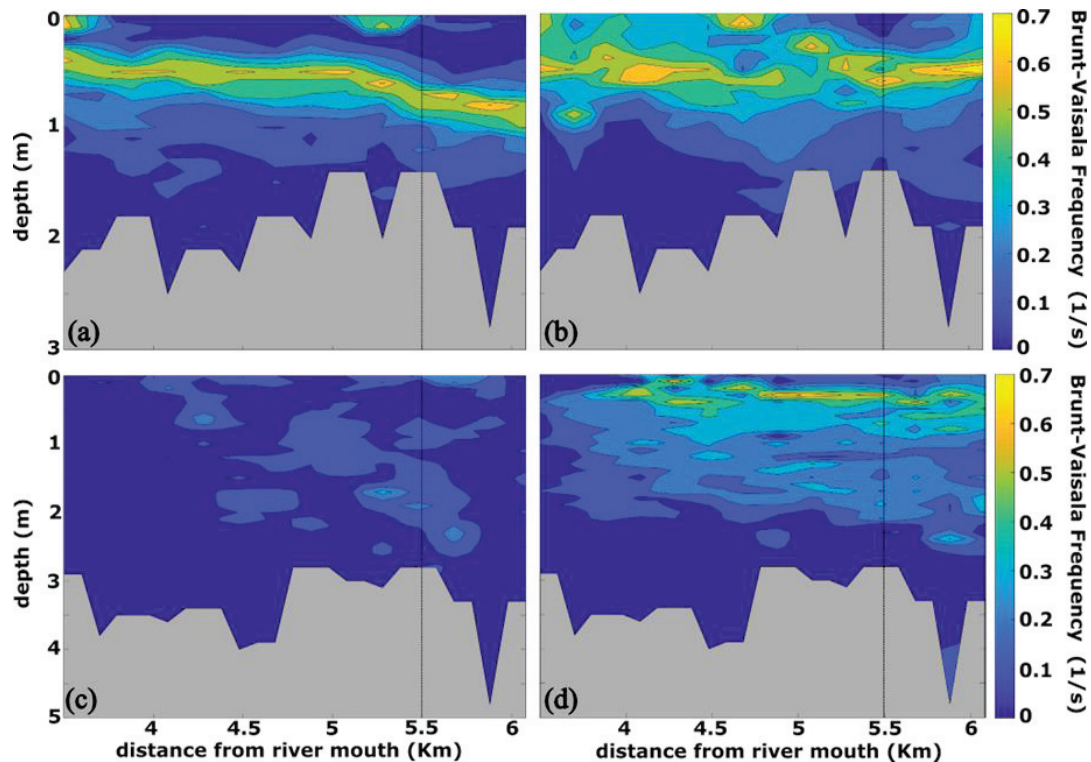
Figure 3.8 Brunt-Vaisala Frequency at flood (first column) and ebb (second column) on March 24 (first row) and March 31 (second row). The black line indicates the start of curving channel at 5.5 Km upstream of river mouth. The data were taken during the maximum flood and/or ebb flow except for (a) which was taken during early flood.

To compare the density structures in straight and curved channels, the logarithmic comparisons of the gradient Richardson number at stations A and B at both flood and ebb tides on March 24 and 31 are provided in Fig. 3.9. The logarithmic gradient Richardson number is found to be positive in the upper half and negative in the bottom half of the water body during the neap tide for both stations. This indicates a higher tendency of stratification on the surface and mixing at the bottom. During the spring tide flood in both channels, the negative logarithmic gradient Richardson number is predominantly negative, indicating mixing throughout the water body. A clear distinction between straight and curved channels is observed in the spring tide ebb. The straight and curved channels are similarly dominated by a positive logarithmic gradient Richardson number in the upper half of the water body. At the same time, the bottom half of the

channel is positive in the curved channel and negative in the straight channel. The leading mechanism that induces this difference is discussed in Section 4.
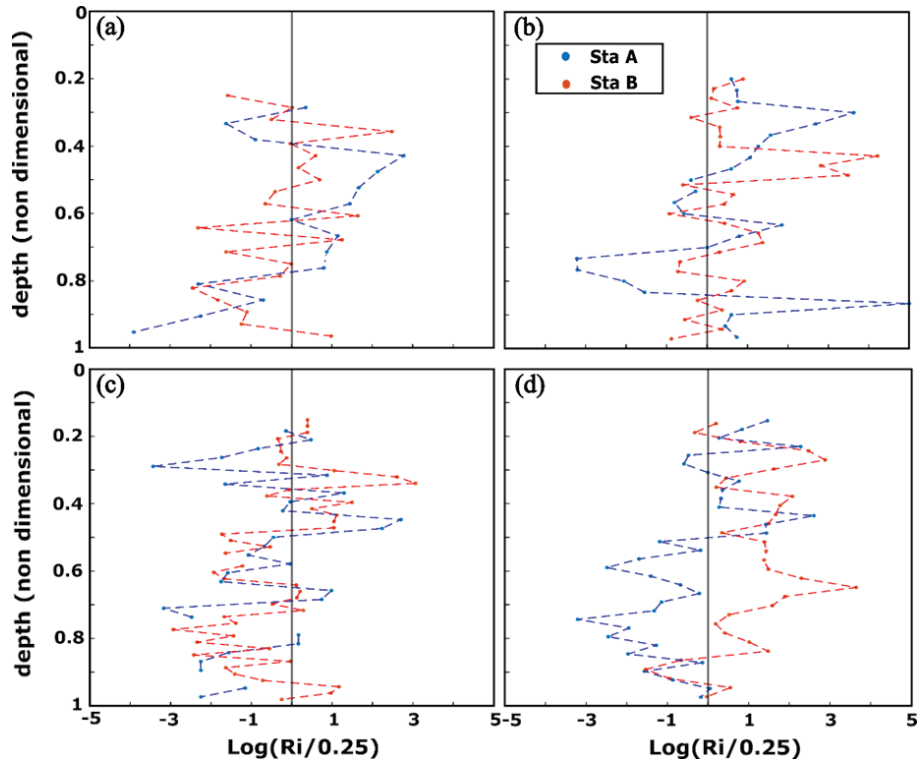
Figure 3.9 Logarithmic gradient Richardson Number in Station A and Station B at flood (first column) and ebb (second column) on March 24 (first row) and March 31 (second row). The data were taken during the maximum flood and/or ebb flow except for (a) which was taken during early flood.

The potential energy anomaly calculated using Eq. 5 is shown in Fig. 3.10. Similar to the Brunt–Vaisala frequency, the difference in channel geometry does not significantly affect the potential energy anomaly during the neap tide, and its value ranges between 20 $Jm^{-3}s^{-1}$ and 40 $Jm^{-3}s^{-1}$. Meanwhile, during the spring tide flood, the potential energy anomaly generally has low values (<20 $Jm^{-3}s^{-1}$) along the channel. At the spring tide ebb, the potential energy anomaly gradually increases from 0 $Jm^{-3}s^{-1}$ downstream of the measured area to 50-60 $Jm^{-3}s^{-1}$ in the salt-wedge that is situated in the straight channel for the ebb of spring tide. In the curved channel, the potential energy anomaly is slightly higher than that of the straight channel.

This seems to be in agreement with the results of the logarithmic gradient Richardson number, which suggests that stratification is more likely to occur in the curved channel than in the straight channel.
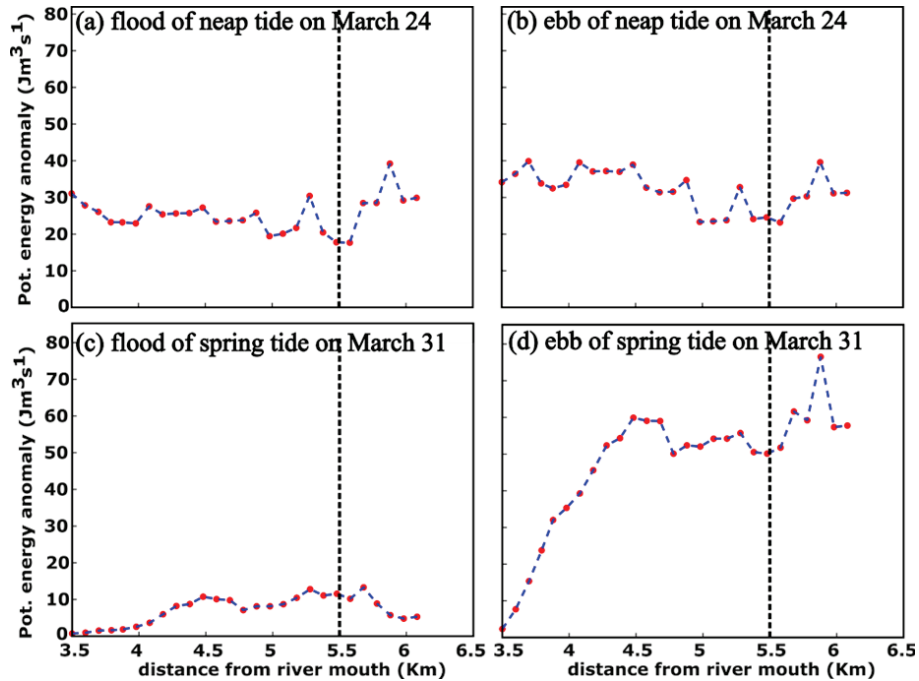
Figure 3.10 Potential energy anomaly at flood (first column) and ebb (second column) on March 24 (first row) and March 31 (second row). The black line indicates the start of curving channel at 5.5 Km upstream of river mouth. The density data were taken during the maximum flood and/or ebb flow except for (a) which was taken during early flood.

3.4 Discussion

3.4.1   Influence of Geometry on The Flow

Channel curvature primarily generates a centrifugal force that induces flow toward the outer bank of the curving channel and can be seen in the surface layers of Stations B and C. Lateral flow patterns at Station A reflect the axial convergence pattern studied by Nunes and Simpson [20], which exhibited surface convergence flow and bottom divergence flow induced by the lateral density gradient. These velocity patterns are observed as left bank oriented in the near-surface and right bank oriented in the near-bottom, which is what we observed at our measurement location (Fig. 3.1b). However, we cannot prove this

hypothesis due to the lack of lateral observational data. Hence it underlines the needs of future studies by conducting more comprehensive simultaneous observation on both lateral and longitudinal orientations.

A comparison of the logarithmic absolute values of the spring/neap tidal-averaged longitudinal and lateral velocities is presented in Fig. 3.11. The application of spring/neap tides averaged here implies the removal of the daily tidal influence on the velocity data, thus leaving only residual velocity. As can be seen in Fig. 3.11a, a significant difference in mid-depth and near-bottom longitudinal velocity is apparent in Station A at spring tide, with the latter outmatching the former by a few orders of magnitude. The difference at residual velocity could be addressed as a result of the periodic occupation of mid-depth layer by pycnocline in the straight part of the channel during the spring tide. This situation leads to the flow resulting in a mid-depth layer that is relatively smaller than the near-bottom layer, which is consistently dominated by landward flow (Fig. 3.7c and 3.7d). At the neap tide, however, the difference in the longitudinal velocity between the two layers is much lower, with the mid-depth velocity slightly greater than the near-bottom velocity. This is in line with the minimum difference in density structure (Fig. 3.7a and 3.7b) during the flood and ebb at the neap tide. In short, the difference in vertical variation of longitudinal residual velocity represents the spring-neap variability due to tidal straining in the Ota Diversion Channel.
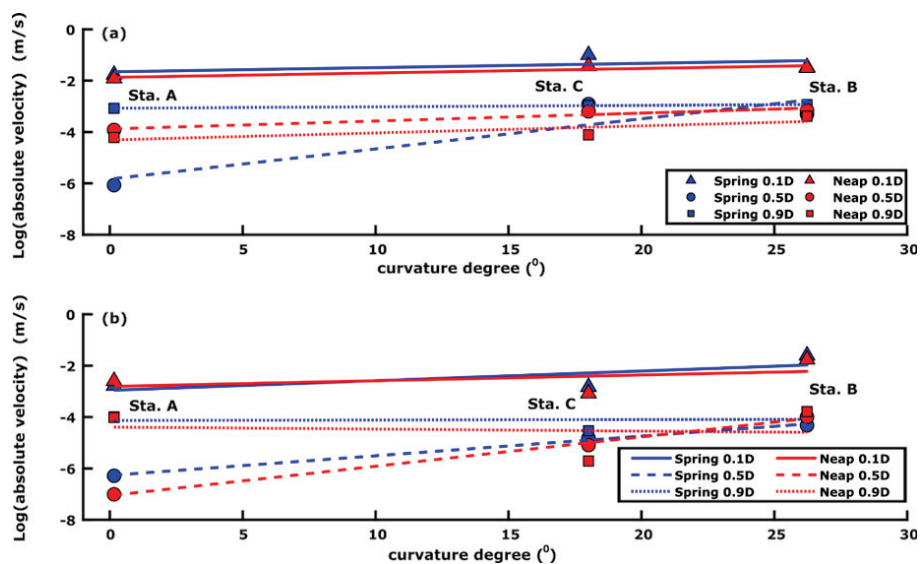
Figure 3.11 The spring/neap tidal averaged longitudinal velocity (a) and lateral velocity (b) vs. curvature degree in all stations at 0.1D, 0.5D, and 0.9D. The trendlines denote the relationship between logarithmic absolute

longitudinal/lateral velocity and the degree of curvature in each respective depth over the water column. These trendlines were made from second degree polynomial curve fitting between curvature degree and the respective logarithmic absolute velocity.

Apart from the significant differences between mid-depth and near-bottom longitudinal velocity at Station A, the spring neap variability of longitudinal velocity was observed to be less notable in the surface layer of Station A or at the other stations. Furthermore, the trend line shows that the longitudinal residual velocity seemed to steadily increase along with the higher curvature degree in the near-surface and near-bottom layers, while a significant increase is observed at the mid-depth. The increase in flow in a curved channel may be induced by its morphology. The straight channel (Fig. 3.1b) has a relatively similar channel width over the depth, whereas the curved channel (Fig. 3.1c and 3.1d) has a channel width, which decreases from the surface to the bottom. The difference in the cross-sectional configuration between both channels could be attributed to the effect of the lateral sediment transport, which often occurs in curving channels. In these channels, the centrifugally induced lateral flow leads to erosion in the outer bank and sediment deposition in the inner bank. Particularly in a partially mixed estuary, Kim and Voulgaris [86] found that sediment from the inner bank was transported to the center of the channel, which resembles the cross-sectional morphology at Station C (Fig. 3.1d). Thus, the smaller cross-sectional area in the mid-depth and near the bottom layer will result in a higher longitudinal velocity in the curved channel. However, it is also notable that the studied channel banks are significantly affected by human activities, as shown in Fig. 3.1. In particular, the curved part of the Ota Diversion Channel was originally constructed as a compound cross-sectional channel [3]. Artificially reinforced banks will prevent the channel from widening freely. Differently, the unrestricted channels, such as the tidal channels formed on open coastal areas, generally widen a lot at the curved parts, leading to a larger cross-section area. Hence, the flow velocity, in this case, is not necessarily greater.

A comparison between the spring/neap tidal-averaged lateral residual velocity is shown in Fig. 3.11b. The lateral estuarine flow seems to have relatively less difference between the spring and neap tides than the

longitudinal ones. Yet, similar to the longitudinal velocity, the lateral velocity in the near-bottom layer of Station A outmatches the mid-depth layer by several orders of magnitude. This could be related to the aforementioned lateral convergence zone of estuarine flow in the straight channel, which makes the mid-depth layer situated at the interface between the convergence flow above and the divergence flow beneath it. Consequently, this induces a minimum lateral velocity in the mid-depth layer. The trendline reveals that the lateral residual velocity tends to increase with an increase in the degree of curvature, particularly in the near-surface and mid-depth layers. On the other hand, the lateral residual velocity at the near-bottom layer exhibits a relatively constant trend with increasing curvature degree. The rising pattern of the lateral residual velocity trend line in the top half of the water column could be a result of the stronger influence of centrifugal acceleration in the curving channel. The centrifugal acceleration tends to induce velocity that goes to the outer bank of the bend in the near-surface layer, as shown in Figs. 3.4b, 3.4c, 3.4e, 3.4f, and 3.5d. In contrast, the velocity toward the left bank in the bottom half section of the water column might also be induced by the depth-independent lateral baroclinic pressure gradient response to curvature [63].

3.4.2   Interaction of Governing Mechanisms

Fig. 3.12 shows a comparison of the tidal straining, river effect, and tidal stirring between the straight and curved channels. The longitudinal density gradient ($\partial\rho/\partial x$) in the straight and curved channels is represented by the difference in the near-bottom density at stations A, B, and C (Fig. 3.6), respectively. Meanwhile, the point-stationary variables of Eq. (3.6) are represented by Station A for the straight channel and Station B for the curving channel in succession. The positive value in the terms presented here indicates that it enhances stratification, whereas negative terms tend to induce mixing in the water body.
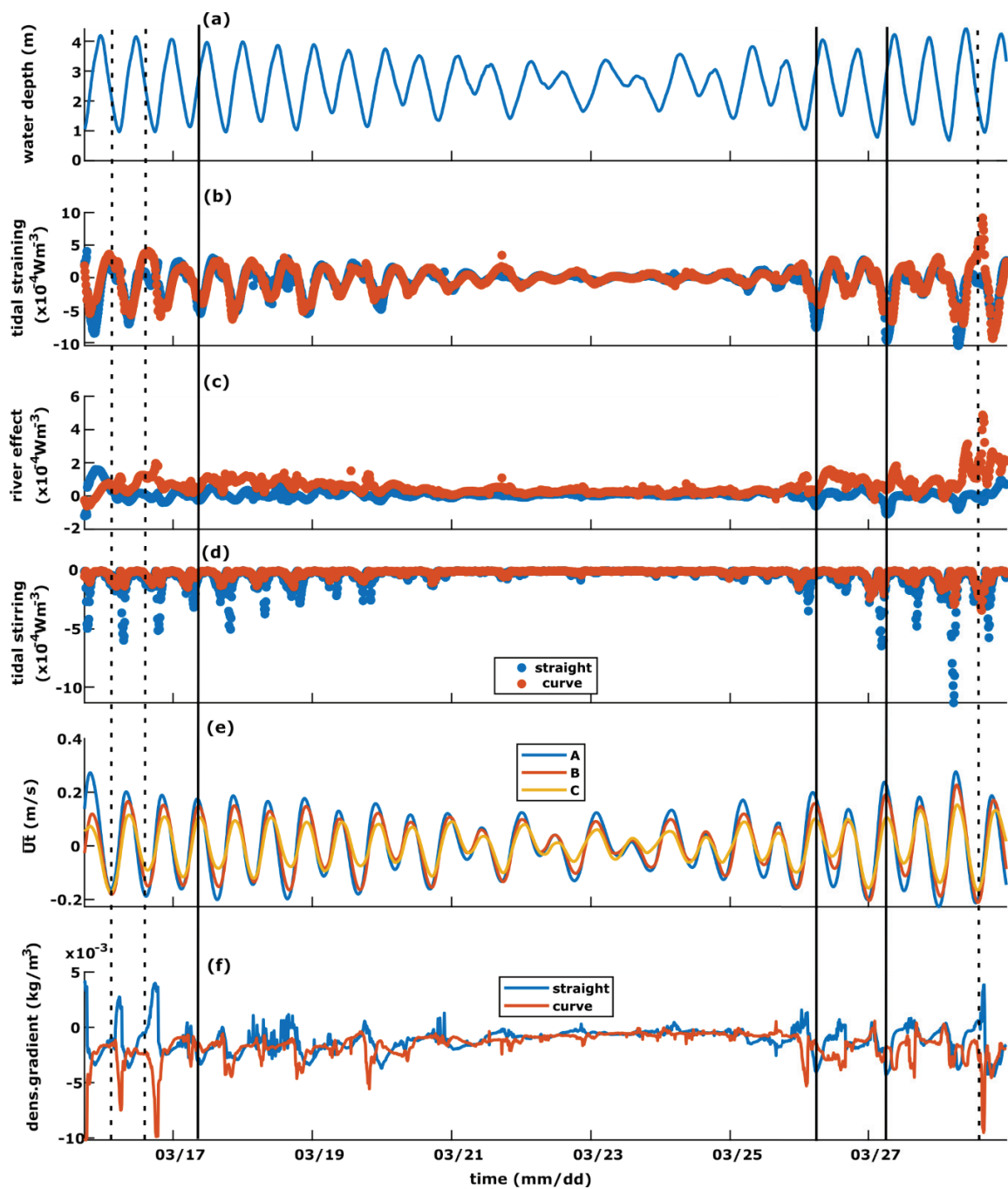
Figure 3.12 (a) Time series of water height above the bed. Comparison between (b) tidal straining, (c) river effect, and (d) tidal stirring. (e) Depth-averaged tidal velocity in the Station A, B, and C, positive value denotes landward velocity and negative value denotes seaward velocity. (f) Longitudinal near-bottom density gradient in the straight channel and curving channel, positive value denotes increasing density to the upstream and negative value denotes decreasing density to the upstream. The black lines indicate examples of peak flood events, while dashed lines denote examples of peak ebb events.

A comparison of the tidal straining in the straight and curved channels over the spring and neap tides is presented in Fig. 3.12b. The spring and neap tidal variability induces different responses of tidal straining, with strong tidal straining occurring during the spring tide and close to non-existent during the neap tide. During the spring tide, the vertical distribution of density in the water column alternates between partially stratified, which is represented by positive tidal straining during ebb, and well-mixed, which is denoted by the negative value of tidal straining during the flood. Since our time series data of density is limited to the near-bottom layer, we employed near-bottom density to calculate the longitudinal density gradient term. Nonetheless, the quantification of tidal straining that is affected by longitudinal density gradient, shows same interpretation of density stratification with the Brunt Vaisala Frequency (Fig. 3.7a-d) and potential energy anomaly (Fig. 3.10a-d). Yet, it is of importance to address limitation of this study in the future research by conducting more comprehensive observation on vertical density distribution temporally. In the context of geometry comparison, although tidal straining has a similar pattern for both channels over the period of observation, the tidal straining in the curving channel is found to have a stronger positive influence at the ebb tide, while in the straight channel, tidal straining presents greater negative values during flooding. The different responses indicate that the curving channel tends to enhance stratification, whereas the straight channel encourages vertical mixing over the water column. To understand the influence of different channel geometries on tidal straining, we further break down the tidal straining into the tidal velocity term and the longitudinal density gradient, as shown in Fig. 3.12e and 3.12f. The tidal velocity at Station A is higher than that at the other two stations because of its location closest to the river mouth. Table 2 presents the values of Pearson correlation coefficient of tidal straining with density gradient and tidal velocity in the straight and curving channels. Positive values mean that the respective aspects strengthen tidal straining while negative values suggest otherwise. Additionally, the correlation values that are close to zero denote the weak correlation between the respective aspects and the tidal straining. Good negative correlations between tidal velocity and tidal straining obtained in both channels with curving channel has slightly greater correlation value than the straight channel. Since positive values of tidal velocity denotes landward flow, these correlations emphasize the different effect of flood and ebb to the strength of tidal straining. On the

other hand, the density gradient represents moderate and weak correlations with tidal straining in straight and curving channels, respectively. Therefore, these differences might suggest that the variation of channel geometry affects the degree of influence of tidal velocity and density gradient in the occurrence of tidal straining throughout the full period of spring and neap tides.

Table 3.2 Pearson correlation coefficients of density gradient and tidal velocity with tidal straining in the straight and curving channels

Tidal straining in	Tidal velocity	Density gradient
Straight channel (AB)	−0.7241	0.5872
Curve channel (BC)	−0.8647	0.1834

Although the density gradient is relatively less influential than the tidal velocity, the spatial and temporal variations of the density gradient in the Ota Diversion Channel represent interesting patterns. The near-bottom longitudinal density gradient (Fig. 3.12f) shows a density gradient anomaly in the straight channel with a positive gradient landward. This anomaly indicates the occurrence of density trapping in the bottom layer, particularly at Station B at low tide. The possible reason for this trapping could be explained as follows. (1) The Ota diversion channel is an ebb-dominated estuary (Fig. 3.1), and the seaward flow forces the intruding dense water back to the river mouth. (2) Because the strongest longitudinal velocity at ebb is situated near the surface layer, the seaward forcing gradually weakens with increasing depth. (3) The weakened seaward force near the bottom and the bathymetry configuration at Station B, which is deeper than Station A (Fig. 3.1b-c), traps the denser water near the bottom that was intruding upstream during the flood. Apart from the several density gradient anomalies between Station B and Station A, the density gradients shown in Fig. 3.12f mostly have negative values that reflect the decreasing value of density in the landward orientation. A comparison of the longitudinal density gradient at the peak flood reveals that a greater density gradient is observed in the straight channel. In contrast, the peak ebb induced a greater density gradient in the curved channel. The density gradient disparity at different tidal phases in different

channel sections indicates that the channel with longitudinally varying geometry could have stronger tidal asymmetry than the channel with homogenous geometry. Consequently, the density gradient will be more influential on the tidal straining in the channel with longitudinally varying geometry at certain tidal phases. This asymmetry is also supported by the study of Pein et al. [61], who found that the tidal asymmetry in a meandering channel was generated by the interchange between density gradients and curving topography. Furthermore, the curving channel plays a significant role by introducing a lateral variation of along the channel advection. However, one of the limitations of our study is that we cannot quantify the cross-sectional variation of along the channel advection because our data are restricted to the channel coverage along the channel.

A comparison of the river effects in the straight and curved channels is shown in Fig. 3.12c. The river effect pattern generally has positive values, which means that this term enhances stratification over the water column. To clearly determine the relationship between the river effects in both channels and river discharge, we compared the river effect term with river discharge, which was estimated from the water level at Yaguchi Gauging Station using Eq. (1). Since we did not obtain discharge data in the Ota Diversion Channel, we used discharge from Yaguchi Gauging Station as a proxy to determine the relationship mentioned above. From this comparison (Fig. 3.13b), a clear difference in the river effect pattern between those above and below 101 m^3/s is observed. The river effect in the curved channel has higher values than that in the straight channel, with a relatively constant difference over the increasing discharge. However, above 101 m^3/s the river effect values in the curved channel are significantly higher than those in the straight channel. It could indicate the predominant influence of centrifugal acceleration over the flow, particularly in the presence of curvature in the channel. The river effect term reflects the shear from the river flow, which is commonly found in the upper half of the water body with heterogeneous density in the estuary. Furthermore, in the curvature area of the stratified estuary, the top half section of the water body is dominated by centrifugal acceleration, which can shift the maximum longitudinal current toward the exit of the curve [82,88]. Although there are no discharge measurements available for Ota Diversion Channel, the approximated

stream flow of 101 m³/s might suggest that there is a critical discharge value in which the river effect term would significantly increase in the curving channel.
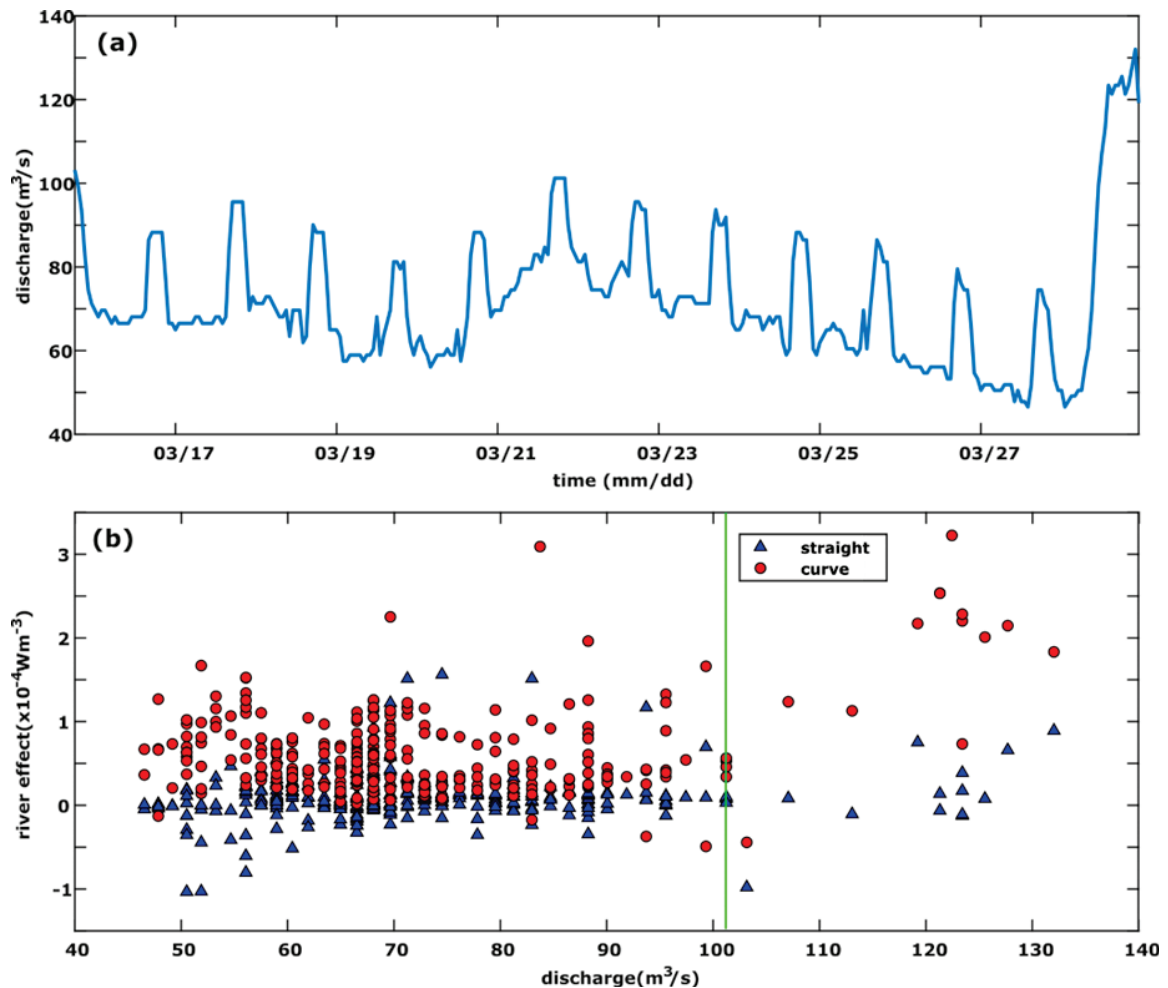
Figure 3.13 (a) time series of river discharge in Yaguchi Gauging Station. (b) Distribution of river effect term in straight and curving channels over measured river discharge in Yaguchi Gauging Station. The green line denotes Q=101m³.

Tidal stirring steadily encouraged uniformity over the vertical density of the water column. This is proven by the constant negative values over time (Fig. 3.12d). This term has strong spring-neap variability, with spring tides inducing greater tidal stirring due to strengthened tidal energy during this period. In addition to the spring neap-variability, tidal stirring is also found to be stronger during the early to mid-stage of the flood and infrequently at the ebb. Consequently, tidal stirring enhances mixing over the water column

during flood events and resists the stratification generated at the ebb. Unlike the gravitational circulation, tidal stirring is strongly affected by changes in the channel geometry. The straight channel induced greater tidal stirring values than the curving channel because of the smaller Richardson number value during both the flood and ebb events (Fig. 3.9c and 3.10d). Furthermore, tidal stirring was the dominant term after tidal straining, as can be seen in the second period of the spring tide (Fig. 3.12d).

A numerical study conducted by Burchard and Hetland [16] revealed that for irrotational flow in a periodically stratified estuary with nonexistent wind forcing and residual runoff, tidal straining accounts for two-third of the estuarine circulation, while gravitational circulation accounts for the remaining one-third. Even though we could not quantify the gravitational circulation term in this study, Soltaniasl [90] quantified this term in the Ota Diversion Channel, albeit with a different approach. He found through salt flux decomposition that gravitational circulation was comparable to the driving mechanisms that are induced by tidal oscillations. Moreover, he also revealed that the gravitational circulation is stronger during the neap tide, which is similar to the case of the Changjiang River, which was observed by Pu et al. [9]. However, it should be noted in the case of low-discharge and mesotidal estuarine channels such as the Ota Diversion Channel, tidal stirring is also found to be on par with the tidal straining. During the neap tide, stratification is found to be relentless over both the flood and ebb as a result of weak tidal straining and stirring along with strong gravitational circulation. During the spring tide, vertical mixing and stratification alternated periodically owing to the interaction of tidal straining, tidal stirring, river effect, and gravitational circulation. The breakdown of the time derivative of the potential energy anomaly in (Fig. 3.12 and 3.13) exhibits that even if the difference in channel geometry might affect each driving mechanism individually, it does not necessarily alter the dominance of certain terms over another.

3.4.3 Long-term Impacts on The Ota Diversion Channel

The Ota Diversion Channel mainly serves as a flood mitigation measure for Hiroshima urban areas. At the time when river discharge is normal, the channel provides homes for estuarine animals and vegetations to flourish on its tidal flats along its riverbanks. Results of our study reveal that the longitudinally varying

geometry of the Ota Diversion Channel enhance tidal asymmetry and residual currents as well as dynamics that are affected by density distribution particularly tidal straining and tidal stirring even though the tidal straining and tidal stirring can be associated with how the salt intrusion occurs [57,96]. In the case of Ota Diversion Channel, the effect of salt intrusion is of limited influence due to the elevated position of the drainage runoff canals from the banks of the Diversion Channel. However, it could prove otherwise for tidal asymmetry and residual currents.

Dronkers [27] showed that in irregularly shaped estuaries the tidal asymmetry can induce residual sediment transport which varies according to the geometry. Moreover, enhanced lateral residual current in the curved part of the channel induces net sediment transport towards the inner bank of the curvature [63]. The morphodynamic evolution due to the continuous sediment transport over a prolonged period might affect the effectiveness of Ota Diversion Channel to combat flooding. Annually, East Asian monsoon generates massive rainfall that turns into heavy flooding in Hiroshima. One the most devastating events was the extreme flooding in 2018, which caused huge infrastructure and life losses [4]. Although, the occurrence of 2018 flooding in Hiroshima was a rare case, it presents a comprehensive image on the degree of risk of flood events in this area. Therefore, it is necessary to manage the morphodynamic condition of Ota Diversion Channel in the long term.

3.5 Conclusions

The spatial and temporal distributions of water velocity and density were measured in the thalweg of curved and straight sections of the Ota Diversion Channel from March 16 to March 31, 2021. The data were used to characterize the tidal river dynamics affected by longitudinally varying channel geometries. Moreover, we investigated the influence of different channel geometry on the driving mechanisms of estuarine circulation. In addition, our study has several interesting findings.

First, the curved channel induces higher residual longitudinal and lateral velocities than in a straight channel. A combination of two factors, the difference in cross-sectional bathymetry configuration and the growing

influence of centrifugal acceleration, generates stronger lateral and longitudinal velocities in the area with a higher curvature degree. Second, the density structure in the Ota Diversion Channel is significantly influenced by tidal straining. It was found that the influence was greater during the spring tides. The variation in channel geometry affected the tidal straining at different times. At the ebb, stronger negative tidal straining was found to enhance the stratification in the curved channel. During the flood, positive tidal straining was established more in the straight channel, which caused mixing. Furthermore, we also found that the different channel geometry affected the degree of significance between tidal velocity and density gradient on the generation of tidal straining governing mechanisms that generated tidal straining (longitudinal density gradient and tidal velocity). Third, the river effect was generally found to be higher in the curved channel than in the straight channel. However, after a certain critical discharge value, the river effect in the curved channel suddenly increased significantly compared to that in the straight channel. To comprehensively examine the relationship between discharge and river effects, further studies are needed, particularly in tidal rivers with high river discharge or during river flood events. Fourth, we discovered that the magnitude of tidal stirring was stronger in the straight channel, especially during the flood. This variability is likely to be induced by a smaller Richardson number in the straight channel. Within the context of low discharge and small mesotidal estuarine channels, one of the additional important findings in our study is that tidal stirring was able to be on par with the tidal straining. This showed a unique behavior in this type of estuary because tidal stirring is not commonly known to be able to compensate for tidal straining in other tidal river and estuarine environments.

Even though our study was performed locally in the Ota Diversion Channel as a case study, the analysis and discussion exhibited the influence of longitudinally varying channel geometry on the tidal river dynamics and its governing mechanisms in a single tidal river channel. Thus, the results and discussion can contribute to increasing the understanding of circulation dynamics in tidal rivers and estuaries. In addition, further studies by simultaneous observation on lateral, longitudinal, and vertical fields are highly recommended to comprehensively understand the impacts of the variation on channel geometry to the

spatial variation of tide-induced hydrodynamics and the associated morphological evolution in these environments.

CHAPTER 4: Subtidal Dynamics in a Tidal River with Limited Discharge

4.1 Introduction

Tidal rivers occupy transitional water bodies in lowland areas situated between the rivers and the sea. Tidal rivers are often located in highly populated, urban areas. Therefore, tidal rivers provide important feedback in society from physical aspects, such as wetland ecosystems, hydrological processes, water quality, and sediment transport, as well as socioeconomic aspects, such as disaster risk prevention, fisheries, navigational safety, and even political stakes [35, 97–100]. A tidal river exhibits a complex hydrodynamic structure because land-originated river runoff encounters bidirectional flow: tidal currents. The hydrodynamic complexity of a tidal river is further enhanced by the impact of other minor, but not insignificant, factors, such as water waves, surges, mean sea level variation, and topographical conditions [67, 101].

The interaction between propagating tidal waves and river runoff leads to tidal distortion and damping [30]. Furthermore, this nonlinear interaction generates quadratic friction within the water columns of tidal rivers [30, 102]. In tidal river systems, the behaviors of tidal-fluvial interaction can be identified by utilizing a one dimensional momentum balance equation, which is referred to as the Saint Venant Equation [28, 67, 103]. Buschman et al. [33] evaluated the friction term in the subtidal (averaged over a diurnal period) Saint Venant equation by utilizing velocity and water elevation data for the Berau River, Indonesia which resulted in a residual flow term (significantly influenced by river runoff, Fr), a river-tide interaction term (Frt), and a tidal asymmetry term (Ft). An observational study of the Mahakam River, Indonesia by Sassi and Hoitink [34] revealed that river runoff significantly affects the relative contributions of the three subtidal friction terms, implying an interrelationship between the development of Frt and Ft with quarter diurnal and fortnightly tides. More importantly, a study by Guo et al. [104] on the Yangtze River, China stated that these subtidal friction terms also governed the variation in the subtidal water elevation, indicating the significant role of subtidal friction in the tidal river environment.

In addition to subtidal friction, the propagating tidal wave in the tidal river generates an inherent landward mass transport known as Stokes flux. The magnitude of the Stokes flux peaked when the phase difference between the water elevation and current velocity was 0^0 and was non-existent when the phase difference was 90^0. In a single tidal river channel with no floodplains, the Stokes flux is typically balanced by the Eulerian seaward 'return' flux, which is closely associated to the river runoff [105]. Hence, the magnitude of the subtidal discharge in a single tidal river channel is usually close to zero [67,106].

In most cases, the contributions of river runoff and river-tide interactions to subtidal friction and river-tide interactions have positive values that reflect a strong seaward orientation of the subtidal velocity, which is largely governed by river runoff [33, 34]. However, in the case of subtidal discharge terms, the river runoff-affected return flux was the product of the subtidal pressure gradient induced by the landward-oriented Stokes flux. Therefore, the return flux naturally comes in a seaward orientation as a net compensating flux to balance the Stokes flux [105,107]. However, it must be highlighted that these studies were conducted in the estuarine environments that received a high amount of freshwater runoff. Recently, Zhang et al. [108] and Zhang et al. [109] conducted numerical simulations of the subtidal flow and discharge by considering a tidal channel with low freshwater runoff in the Yangtze Delta, China. Their studies revealed that landward return flux can be generated owing to variations in the channel depth and width over long distances. The landward return flux further generated a significant difference between the subtidal discharge magnitude and upstream and downstream phases. However, to the best of our knowledge, the existence of an anomaly in the return flux pattern was only observed in the results of the numerical simulation. Additionally, because subtidal friction terms are also affected by the amount of river discharge, changes in subtidal behavior due to limited river discharge might affect more than just subtidal discharge. Herein, we intend to confirm the existence of such anomalies, not only in subtidal discharge, but also in subtidal friction, from field observations in a tidal channel with limited river runoff.

This study investigated the spatial and temporal variability of subtidal friction and subtidal flux in a low-discharge tidal river channel using the frequency domain and theoretical decomposition analyses. The

frequency domain analysis consisted of power spectrum and tidal harmonic analyses, which revealed the dominant tidal mechanisms in the tidal river channel. The decomposition analyses by Buschman et al. [33] and Buschman et al. [105] were employed to unravel the underlying dynamics. We demonstrate the vertical variability in the friction and flux terms, the governing mechanism that induce their variability, and their anomalous orientation. The remainder of this chapter is organized as follows. Section 2 describes the study area, the data, and the methods used. Sections 3 and 4 present the results and a discussion, respectively. Finally, a summary of the study is presented in Section 5.

4.2 Materials and Methods

4.2.1   Field Site

The Ota River Estuary is a small-scale estuarine network situated in the delta of Hiroshima which flows into Hiroshima Bay, Japan (Fig. 4.1). The Ota River Estuary has high socioeconomic value in Hiroshima. In addition to the vital functions of this estuary for transportation and tourism, its downstream area is extensively used for oyster aqua-culture [110]. The tidal regime in this estuary is mainly semidiurnal, with a tidal range varying from 1.2 m at neap tide to 4 m at spring tide at the river mouth [111]. Over this multichannel network, tidal waves can propagate as far as 13 km upstream from the mouth, although the saline water intrusion length is slightly shorter, at 11 km [89]. The Ota Diversion Channel is a partially stratified estuary, with a periodic semidiurnal stratification cycle induced by tidal straining. During the flood and the first half ebb, the channel is well mixed, while in the latter half of the ebb, salt wedge formation occurs [72,112]. Additionally, the salinity in the channel varies from 10 psu to 30 psu fortnightly [113]. The maximum tidal current velocities during the flood and ebb, respectively, are 0.65 m/s and 0.5 m/s [114].
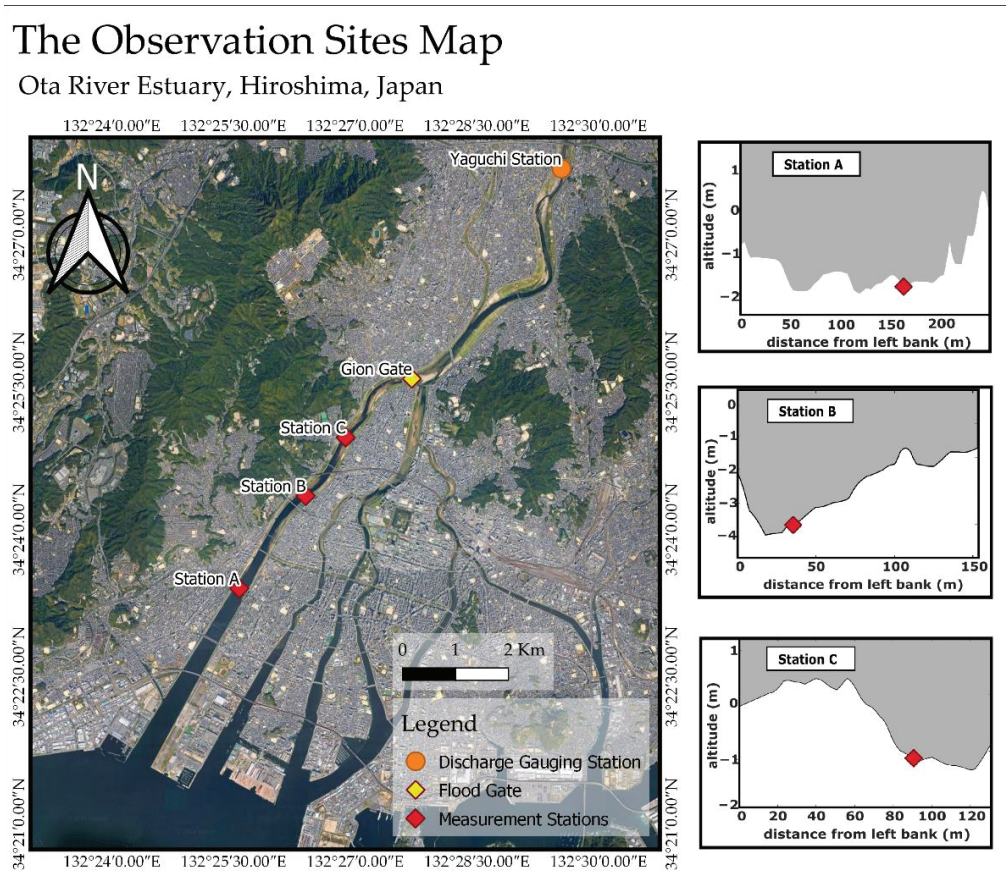
Figure 4.1 The observation sites in the Ota Diversion Channel, Hiroshima, Japan. Red diamonds show the location of instrument deployment. Insets show a cross-sectional view (seaward) of each station.

At 9 km upstream of the river mouth, the Ota River Estuary bifurcates into two main branches. The west branch is an artificial channel called the Ota Diversion Channel, whereas the east branch splits further into four separate downstream rivers. The Ota Diversion Channel's mean depth and width are approximately 2.1 m and 248 m, respectively, while the east branch has the mean depth of around 2 m and mean width of 212 m. Measurements of water level by the Ministry of Land, Infrastructure, Transport, and Tourism (MLIT) at the Yaguchi Gauging Station revealed that under normal conditions, the total discharge that flows through the estuary is approximately 50–80 m^3 during summer and 20–30 m^3 during winter [113]. Approximately 10–20% of the total discharge flows to the Ota Diversion Channel, depending on the flow condition, whereas the remaining streams flow into the bifurcating eastern branch [90].

The Ota Diversion Channel was constructed from 1934 to 1967 to mitigate Hiroshima City's flood disaster risk during the rainy and typhoon seasons [3]. The Ota Diversion Channel is divided into two parts. The compound cross-sectional channel spans 6 km downstream of the Gion Floodgate, and a single cross-sectional channel spans 3 km downstream of the compound channel. Generally, the bed materials in the Ota Diversion Channels are dominated by silt and clay, with an increasing proportion of finer particles closer to the river mouth [3, 91]. Additionally, under normal conditions, the suspended sediment concentration in the Ota Diversion Channel does not exceed 100 g/m^3 [72]. The Gion Floodgate (a flood control structure at the upstream end of the Ota Diversion Channel consisting of three sluice gates) was built to regulate the amount of river flow to the channel. When the gauging station at Yaguchi reports a discharge of greater than 400 m^3/s, the Gion Floodgate is fully opened. Xiao et al. [91] classified the Ota Diversion Channel as having moderate estuarine circulation because it is influenced by limited run-off and mesotidal flow from Hiroshima Bay.

4.2.2 Data Acquisition

A measurement program was conducted in the compound channel section of the Ota Diversion Channel during March 16-28, 2021. Three upward-looking ADCPs (2 MHz Aquadopp profilers, Nortek Co., Ltd.) were deployed at three different locations along the Ota Diversion Channel to measure the current profiles and water depths. All of these were located in the thalweg of the compound channel. However, one was located in a straight channel section (station A), whereas the other two were located in relatively curved channel sections (stations B and C). The ADCPs for measurement programs were designed to have 10 min profiling and averaging intervals, 0.1 m blank distance, and 0.25 m cell depth, with as many as 30 bins. Topographic measurements were conducted on a total station to convert the measured water depths into water levels. Tokyo Peil (T.P.) of Japan, a modern sea level datum based on the mean sea level in Tokyo Bay, was used as a reference for water levels at all stations. Two ACT-HR (conductivity and temperature loggers, Alec Electronics Co., Ltd.) were deployed 15 cm above the riverbed at stations A and C, with 10 min sampling periods to obtain the near-bottom water density at both the upstream and downstream edges

of our observation zone. The measurement accuracy of the sensors was 0.05 °C for temperature and 0.02 mS/cm for conductivity. The rating curve at the Yaguchi Gauging Station of the MLIT was used to estimate the river discharge during the measurement programs. The observed water depth, near-bottom salinity, and current velocity at each station are shown in Fig. 4.2.
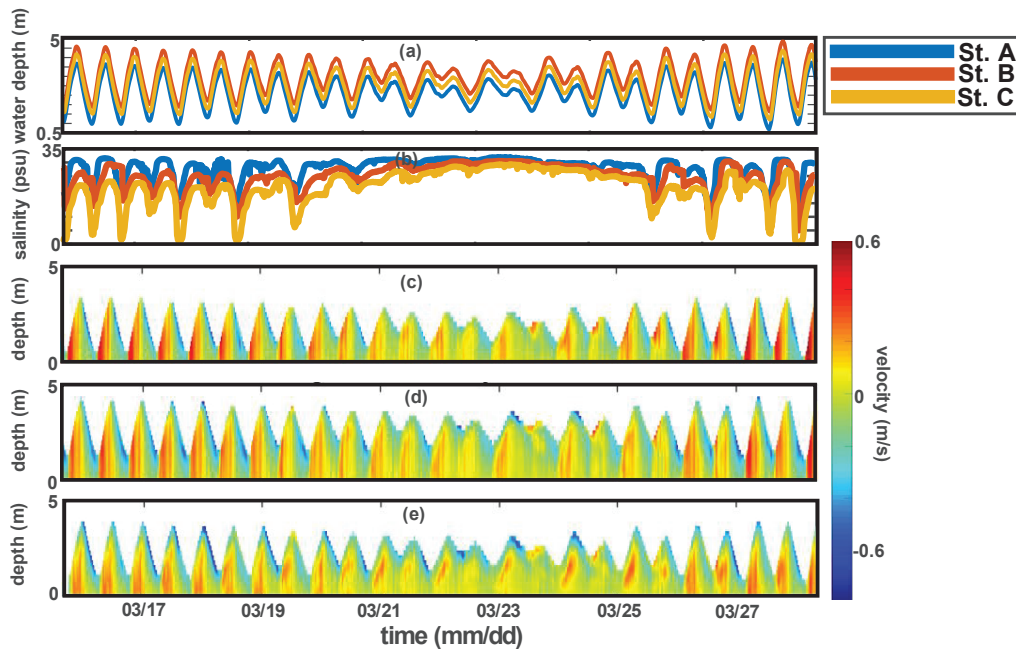
Figure 4.2 Time series plot of observed water depth (a), near-bottom salinity (b), and current velocities in station A (c), station B (d), and station C (e).

4.2.3 Data Processing

The water velocity data from the ADCPs were filtered by omitting bins above the water surface that had low backscatter counts (20–30 counts). To obtain the longitudinal velocity of the flow, the filtered current data were rotated from an east-north orientation to the orientation of the channel. The longitudinal velocity profile was then vertically divided into three sections, and all the velocity bins within each section were depth-averaged. The division of the depth section was utilized to represent the vertical variability of the dynamic mechanisms analyzed in this study. Each velocity section covered one-third of the total water depth, representing the upper, middle, and lower velocities over the water column. Simultaneously, the

water level data at each station were averaged over a 25 h window to obtain the subtidal water level. The tidal range was obtained by subtracting the maximum water level from the minimum water level for the 25 h window.

4.2.3.1 Tidal Frequency Domain Analysis

- Spectral Analysis

Tides greatly affect the water level and current in tidal rivers, with varying level of energy at diurnal, semidiurnal, quarterdiurnal, and fortnightly time scales. The power spectrum describes the time-series data in its mean frequency content. Therefore, the power spectrum can distinguish between variability and influential processes within certain time-series data. Herein, the power spectrum was calculated with the aim of resolving dominant tidal processes in the Ota Diversion Channel between a period of 13 days (total length of measurement period) and 2 h (cut-off Nyquist frequency for hourly data). To obtain the power spectrum, we employed the Fourier transform, a method to convert continuous time-series data with a certain time step into its power distribution in the frequency domain [115]. Mathematically, the Fourier transform can be expressed as [116]

$$\hat{F}(k) = \int_{t1}^{t2} F(t)e^{-2\pi kt}dt \tag{4.1}$$

where F(t) refers to the water level or water current at certain time (t), t1 and t2 denote the start and end times of the analyzed period, and k represents the wave number. The power spectrum is then obtained by multiplying the discrete Fourier transform with its complex conjugate, as shown by the following equation [116]

$$S(k) = \left|\frac{1}{2\pi}\sum_{t1}^{t2} F(t)e^{-kt}\right|^2 = \frac{\hat{F}(k)\widehat{F_*}(k)}{2\pi} \tag{4.2}$$

in which $\hat{F}(k)$ is the discrete Fourier transform of the analyzed time series, and $\widehat{F_*}(k)$ is its complex conjugate. Herein, we applied this method to analyze the mean velocities in each depth section and the water level data. In this analysis, we used hourly water level and velocity data instead of subtidal data to consider the influence of overtide components.

- Harmonic Analysis

We performed tidal harmonic analysis, a least-squares fitting procedure, in the short-term mode to depth-averaged velocity data, based on the T_Tide function [117]. Originally, this method commonly applied the water level time series as the total of a mean value and a group of harmonic terms, as follows:

$$\eta(t) = b_0(t) + \sum_{n=1}^{N}[A_n \cos(\omega_n t - \theta_n)] + r(t)] \tag{4.3}$$

where η (t) denotes the water level at a specified time; b_0(t) is the mean water level; and A, ω, and θ are the tidal amplitude, frequency, and phase, respectively, of tidal constituents n (n = 1,2.. .N), and r(t) represents the residual components. The short-term tidal harmonic analysis in this study utilized a short data sequence of a 25 h depth-averaged velocity to provide a time series of tidal outputs for the six tidal constituents. Three of these tidal constituents, K1, M2, and M4, were used to represent diurnal, semidiurnal, and quarterdiurnal velocities, respectively.

4.2.3.2 Subtidal Friction Decomposition

To examine the behavior of the subtidal variation in the Ota Diversion Channel, we followed the approach developed by Buschman et al. [33] to differentiate the subtidal friction components from a cluster of tidal constituents that are similar in frequency. First, the friction term in the subtidal momentum balance can be given as

$$\left\langle gW\frac{U|U|}{C^2}\right\rangle = \frac{gW}{2\pi C^2}\int_0^{2\pi} U|U|dt \tag{4.4}$$

in which U is the current velocity, W denotes the channel width, the Chézy coefficient is represented by C, and the angular bracket describes the averaging process over a diurnal period.

Subsequently, an odd function [30,118] was used to analytically approximate the product of U|U| in the friction term. The friction term can then be expressed as

$$\frac{gW}{2\pi C^2}\int_0^{2\pi} U|U|dt \approx \frac{gWU_m^2}{2\pi C^2}\int_0^{2\pi}(a\tilde{U} + b\tilde{U}^3)dt \tag{4.5}$$

where $\widetilde{U}$ is the current velocity nondimensionalized by the maximum velocity (U_m), and a and b are two constant coefficients set to 0.3395 and 0.6791, respectively, based on the work of Godin [30]. The dominant velocity components over a diurnal period occur at diurnal, semidiurnal, and quarterdiurnal frequencies. Hence, the nondimensional current velocity can be approximated as [33]

$$\widetilde{U} \approx \widetilde{U}_0 + \widetilde{U}_1 \cos(\omega_1 t - \Phi_1) + \widetilde{U}_2 \cos(\omega_2 t - \Phi_2) + \widetilde{U}_4 \cos(\omega_4 t - \Phi_4) \qquad (4.6)$$

The subscript i = 0, 1, 2, 4 denote subtidal currents, diurnal tidal currents, semidiurnal tidal currents, and quarterdiurnal currents, respectively. In this study, $\widetilde{U}_0$ was obtained by averaging the measured current velocity over a diurnal period, whereas $\widetilde{U}_1$, $\widetilde{U}_2$, and $\widetilde{U}_4$ were obtained through harmonic analysis, as mentioned in the previous subsection.

To obtain the subtidal friction, Equation (4.5) was substituted by Equation (4.6), yielding

$$\frac{gWU_m{}^2}{2\pi C^2} \int_0^{2\pi} (a\widetilde{U} + b\widetilde{U}^3) dt = \frac{gWU_m{}^2}{2\pi C^2} \left((a\widetilde{U}_0 + b\widetilde{U}_0^3) + \frac{3b}{2} \widetilde{U}(\widetilde{U}_1^2 + \widetilde{U}_2^2 + \widetilde{U}_4^2) + \right.$$

$$\left. \frac{3b}{4} (\widetilde{U}_1^2 \widetilde{U}_2 \cos(2\phi_1 - \phi_2) + \widetilde{U}_2^2 \widetilde{U}_4 \cos(2\phi_2 - \phi_4)) \right) \qquad (4.7)$$

The first term inside the bracket on the right-hand side represents Fr, the subtidal friction that is induced by the river flow. The second term is Frt, which is the subtidal friction caused by the interaction between the river flow and tides. Finally, the third term represents Ft, which is the subtidal friction due to tidal asymmetry.

4.2.3.3 Stokes Fluxes Analysis

We investigated the subtidal water transport dynamics in the Ota Diversion Channel by analyzing the Stokes flux, a landward water transport which is induced when the water level and current velocity are in phase, or when the phase difference between the two is minimal [105]. The Stokes flux is balanced by the seaward Eulerian flux, which is created by the gradients in the subtidal water level. To obtain these fluxes, we followed the approaches of Buschman et al. [105] and Sassi and Hoitink [34]. First, the observed current velocity is decomposed into

$$U = U_0 + U'' \tag{4.8}$$

where U" is obtained from the zero-mean variation in the current velocity during a tidal cycle. Likewise, the total depth can be expressed as

$$D = h + \eta_0 + \eta'' \tag{4.9}$$

in which h is the water depth η_0 is the subtidal elevation, and η" denotes the zero-mean variation in the water surface elevation during a tidal cycle. Subsequently, by assuming a constant channel width, the subtidal flux can be expressed as

$$\frac{Q}{W} = U_0(H + \eta_0) + (U''\eta'') \tag{4.10}$$

The first term on the right-hand side represents the Eulerian return flux, and the second term represents the Stokes flux.

4.3 Results

4.3.1 Time and Frequency Variation of Water Level, Near-Bottom Density, Current Velocity

The tidal range and subtidal elevation at each station are shown in Fig. 4.3. Notable temporal variations in the tidal range due to spring-neap tidal cycles were observed at all stations. Stations A, B, and C, located at the channel thalweg, had tidal ranges relatively similar to the spring tidal ranges, which were approximately 1.5–2 m larger than the neap tidal ranges. Similar to the tidal range, the subtidal elevation also exhibited strong temporal variability because of the spring-neap tidal cycles at all stations. At longitudinally arranged stations, the variability in the subtidal elevation was stronger, moving land-ward. At all stations, the subtidal elevations at spring tide are observed to be 0.2 to 0.3 m higher than during the subsequent neap tide. Fig. 4.4 displays the near-bottom densities at stations A and C. They indicated a clear modulation influenced by the spring-neap variation in salinity (Fig. 4.2b). The near-bottom water density during the neap tide remained above 1015 kg/m^3 at both stations, whereas during the spring tide, the water densities dropped to 1010 kg/m^3 and 1001 kg/m^3 at Stations A and C, respectively.
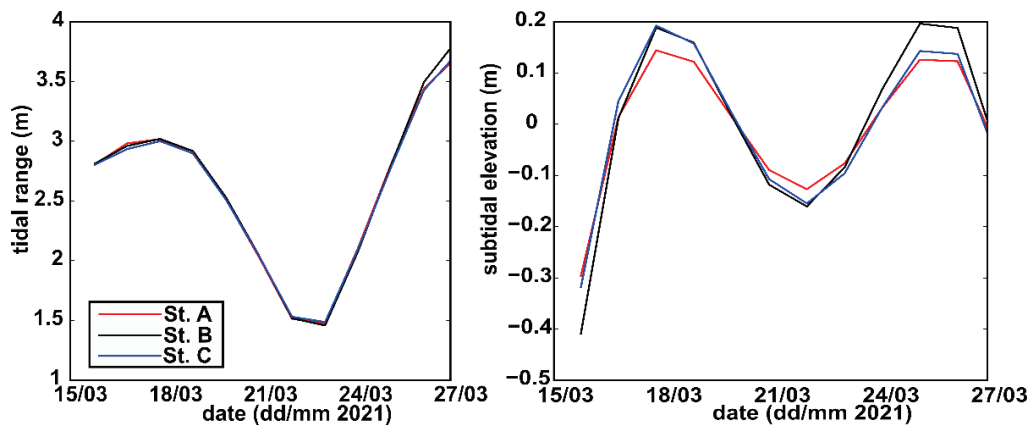
Figure 4.3 Tidal ranges (left) and subtidal elevations (right) at Stations A, B, and C.
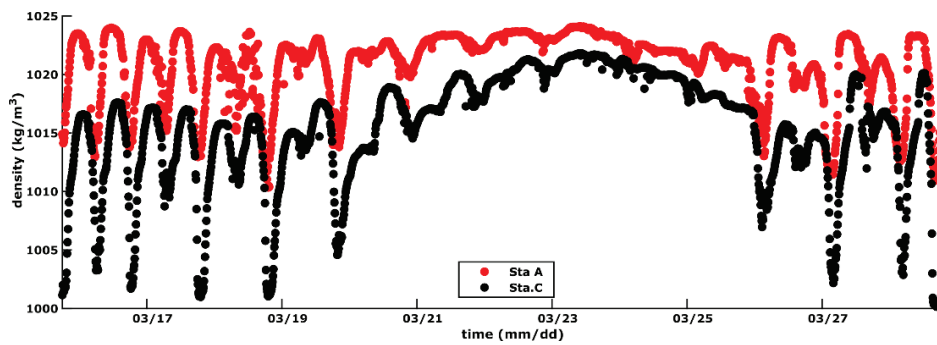
Figure 4.4 Water densities at Stations A and C.

Fig. 4.5 shows the time series of the river discharge at the Yaguchi Gauging Station and the subtidal velocities at the three stations. Positive values represent seaward subtidal velocities, and negative values represent landward subtidal velocities. During the observation period, the discharge at the Yaguchi Gauging Station ranged from 50 m^3/s to 130 m^3/s. Since, at most, the Ota Diversion Channel only received one-fifth of the total discharge from the Ota River, it can be said that during the observation period, the channel was under the limited influence of freshwater runoff. The subtidal velocity ranges from 0.05 m/s to 0.2 m/s at the surface, −0.025 m/s to 0.025 m/s at the mid-depth, and −0.05 m/s to −0.01 m/s at the lower depth. The subtidal velocity represents a distinct vertical variability from the seaward subtidal velocity at the upper

depth. Vertically, the magnitude of the subtidal velocity gradually diminished from the upper depth to mid-depth before changing in a landward direction at a lower depth.
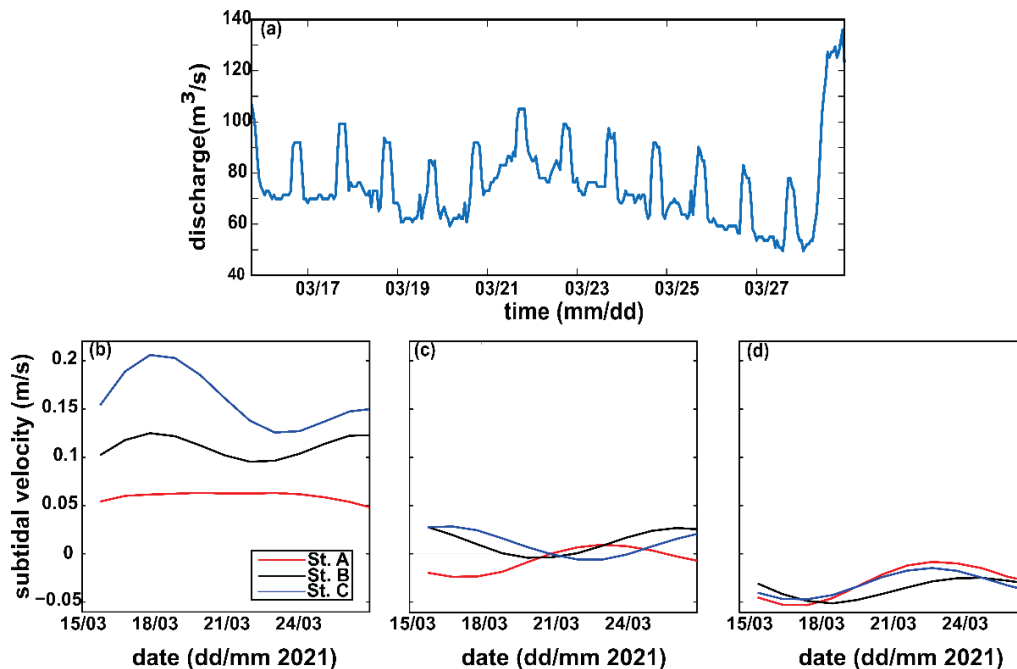
Figure 4.5 River discharge at the Yaguchi Gauging Station (a) and subtidal velocities at the upper depth, (b) mid-depth (c), and lower depth (d) at Stations A, B, and C.

Fig. 4.6 shows the distribution of the energy spectra of the water level and mean velocity at the upper, middle, and bottom depths at all measurement stations along the Ota Diversion Channel, which were estimated using the Fourier transform. The water level spectrum in Stations A, B, and C (Fig. 4.6a) indicates that the Ota Diversion Channel is dominated by signals in the 12 h and 24 h bands. Both bands represents semidiurnal and diurnal tides, with the former being significantly greater than the latter, and no significant difference in energy between each station is observed. In contrast, a significant amount of energy is also observed in the 7-day power-peaking band, which shows the effect of long-period tides (2SK5 and 2MK5) that are most influential at Station B. Peak bands can also be found in the spectrum with periods lower than 12 h, particularly at 3 h, 4 h, 6 h, and 8 h. These peaking bands are usually referred to as overtides and are induced by shallow-water interactions [119]. These interactions lead to the transfer of energy from the

semidiurnal and diurnal tidal components to the lower period bands [26] and increase the energy in these bands from downstream to upstream. Spectral analysis of the depth-averaged velocities in each depth section (Fig. 4.6c, e, g) at stations A, B, and C also shows the dominance of the semidiurnal tidal velocity, although its magnitude is only slightly greater than the overtide velocity. Furthermore, a distinct difference in the water level spectrum is observed for diurnal tidal velocity. The diurnal bands are only slightly stronger than the overtide bands at lower and mid-depths, whereas the overtide bands are more prominent at the upper depth. This phenomenon indicates that the energy decay rates of semidiurnal and diurnal tides and their energy transfer to shallow water tidal components are more intense in the water current than in the water level.
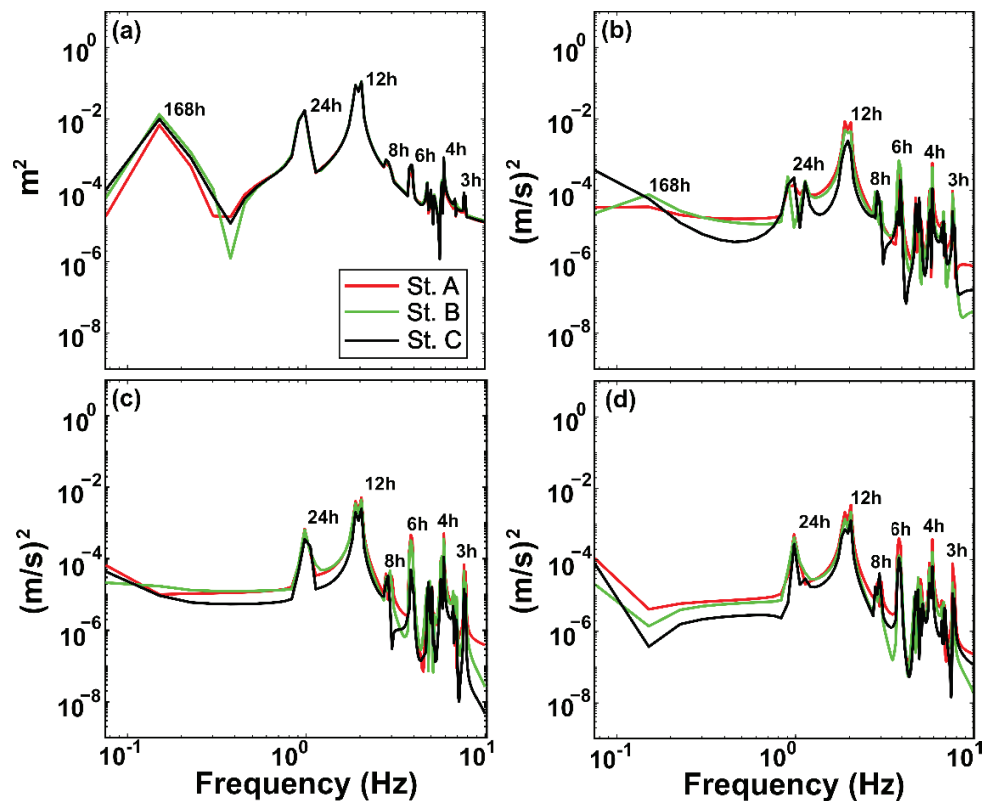
Figure 4.6 The power spectrum of water elevation (a) and current velocity in upper (b), mid-depth (c), and lower (d) depths at Stations A, B, and C.

The time series of the diurnal velocity (U1), semidiurnal velocity (U2), and quarterdiurnal velocity (U4) based on harmonic analysis at each depth at stations A, B, and C are shown in Fig. 4.7. Semidiurnal tidal species dominated the velocity signal at each depth, featuring more fluctuations in the amplitude maxima than in the amplitude minima (Fig. 4.7b,e,h). The temporal variation of U2 is strongly modulated by spring-neap variation, with a velocity between 0.15 to 0.4 m/s at the spring tide and 0.04 to 0.15 m/s at neap tide, respectively. The semidiurnal velocity is higher in the downstream area. U4 co-oscillated with U2 at stations A and B, respectively. At Station C, U4 shows relatively insignificant values that fluctuated over time (Fig. 4.7c,f), except at a lower depth (Fig. 4.7i), where spring-neap modulation is apparent. U1 is the least dominant tidal velocity, and its values do not vary with U2 or U4. The U1 values peak during the neap tide and reach a minimum during the spring tide at mid- and lower depths (Fig. 4.7d,g).
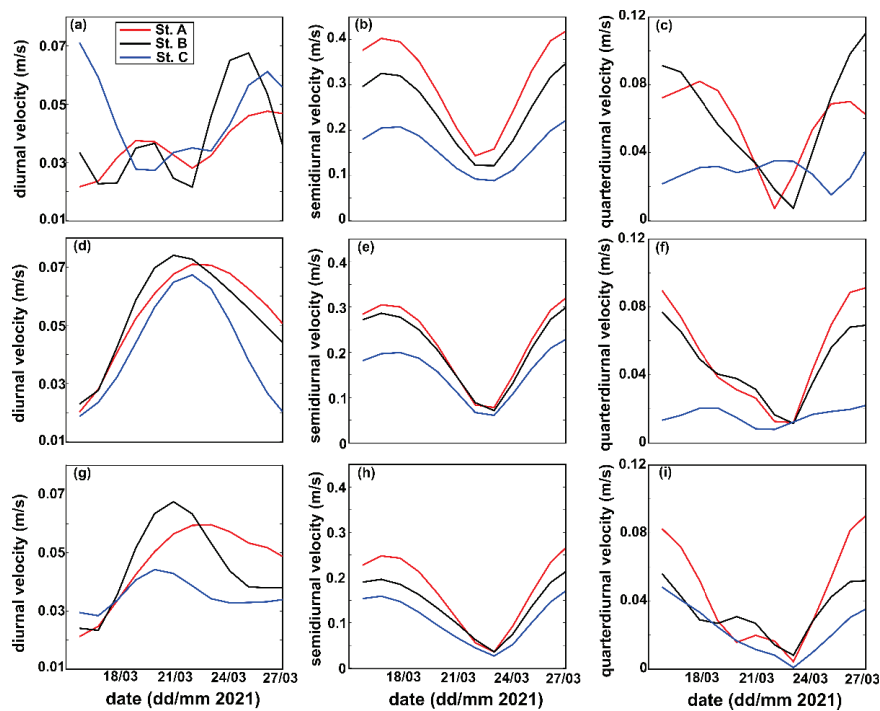
Figure 4.7 The diurnal velocity (a,d,g), semidiurnal velocity (b,e,h), and quarterdiurnal velocity (c,f,i) at upper (top row), mid- (middle row), and lower depth (bottom row) at Stations A, B, and C.

4.3.2   Subtidal Friction

The results of the harmonic analysis of the shape of the diurnal, semidiurnal, quarterdiurnal, and residual currents were utilized to determine the effect of subtidal friction on the tidal dynamics in the Ota Diversion Channel. Eq. (4.7) was employed to estimate the contribution of subtidal friction due to river flow (Fr), river-tide interaction (Frt), and tidal asymmetry (Ft). However, since the influence of freshwater discharge can be neglected in this channel, we would like to denounce the river flow effect (Fr) as "subtidal flow", hence Frt is a tidal–subtidal interaction. This is partly because Fr and Frt employ U0, which represents subtidal velocity. In a high-discharge environment, U0 is synonymous with river flow, because river runoff is the leading non-tidal force.

Fig. 4.8 displays the contributions of Fr, Frt, and Ft in Stations A, B, and C. Along the Ota Diversion Channel, the subtidal flow is the most influential component of the subtidal friction to the extent that its values are greater than the tidal–subtidal interaction and tidal asymmetry by an order of magnitude (Fig. 4.8c, f, i), even when the amplitude of semidiurnal velocity is notably higher than the subtidal velocity (particularly at spring tide). The sign and temporal pattern of Fr closely followed those of U0, with diminishing subtidal friction at lower depths before changing from positive to negative near the bed. The Frt also shows vertical variability in terms of magnitude and sign (Fig. 4.8a,d,g). Indeed, the temporal variation in Frt indicates that Fr might have greatly affected it, although according to Buschman et al. [33], Frt is more influenced by squared tidal velocity species. The third component, Ft, has a relatively smaller magnitude than the other two components, with small vertical variability and a greater tendency to have a negative sign over the observation period. The small magnitude of Ft is a result of the interaction between semi-diurnal and quarterdiurnal tidal species, which induce an ebb-dominated environment. Furthermore, unlike Fr and Frt, the sign of tidal asymmetry depends on the phase difference between the diurnal, semidiurnal, and quarterdiurnal tidal species. Therefore, they could independently reinforce or reduce the other two terms. By separating the water column vertically, we showed that Fr and Frt, in the tidal channel with a small discharge, have vertical variability not only in magnitude, but also in its positive/negative orientations. The reasons for the vertical variability of Fr and Frt are discussed in Section 4.

Figure 4.8 Frt (a, d, g), Ft (b, e, h), and Fr (c, f, i) at upper (top row), mid- (middle row), and lower depth (bottom row) in Stations A, B, and C.

4.3.3 Stokes Fluxes

The temporal distributions of Stokes flux, return flux, and their subsequent total fluxes at stations A, B, and C are presented in Fig. 4.9. Negative values denote landward flux, and positive values represent seaward flux. Stokes fluxes at Station A, B, and C are observed to be predominantly negative (-0.025 m²/s to 0 m²/s) throughout all depths, except for relatively minor positive values in the upper depth of Station C (~0.01 m²/s) during the second phase of spring tide (Fig. 4.9a,d,g). The time series of Stokes fluxes shows temporal variation due to the spring-neap tidal cycles, with greater values further upstream. Because Stokes flux is affected by the phase difference between the current velocity and water level instead of merely the tidal magnitude, its values will be greater when the diurnal-semidiurnal inequality is at its maximum and lower when the tidal asymmetry is at its minimum [120]. The return flux shows temporal patterns that do not

clearly resemble the variation due to the spring-neap tidal cycles. The values of the return flux, which are higher than those of the Stokes flux, vary with both positive and negative signs (Fig. 4.9b, e, h). In the upper depth, the return flux varies in positive values from 0.04 m^2/s to 0.2 m^2/s, with greater values observed farther upstream. At mid-depth, the return flux varies from -0.025 m^2/s to 0.045 m^2/s. During spring tide, the return flux at Station A is predominantly negative, whereas a positive return flux is more apparent at Stations B and C. At neap tide, the values of the return flux at all stations are relatively close to zero. At lower depths, the return flux induced negative values at all stations, ranging from -0.06 m^2/s to 0 m^2/s. Subsequently, the total flux at all stations has non-zero values and is clearly modulated by the return flux because its magnitude is greater than that of the Stokes flux.
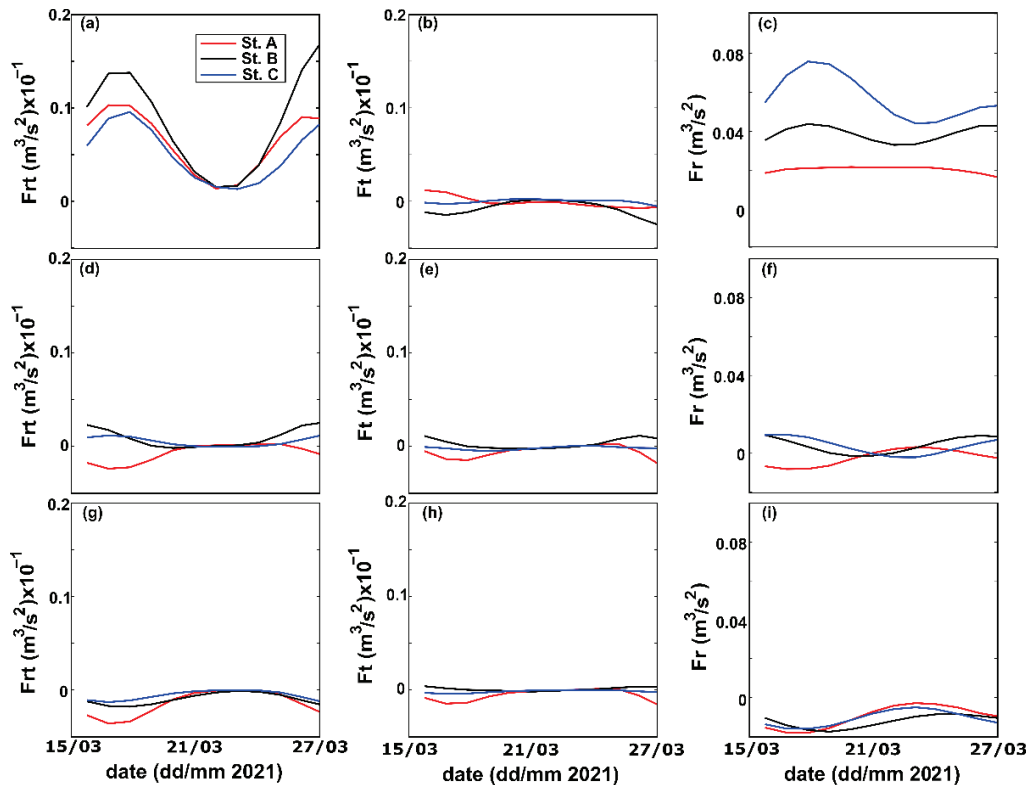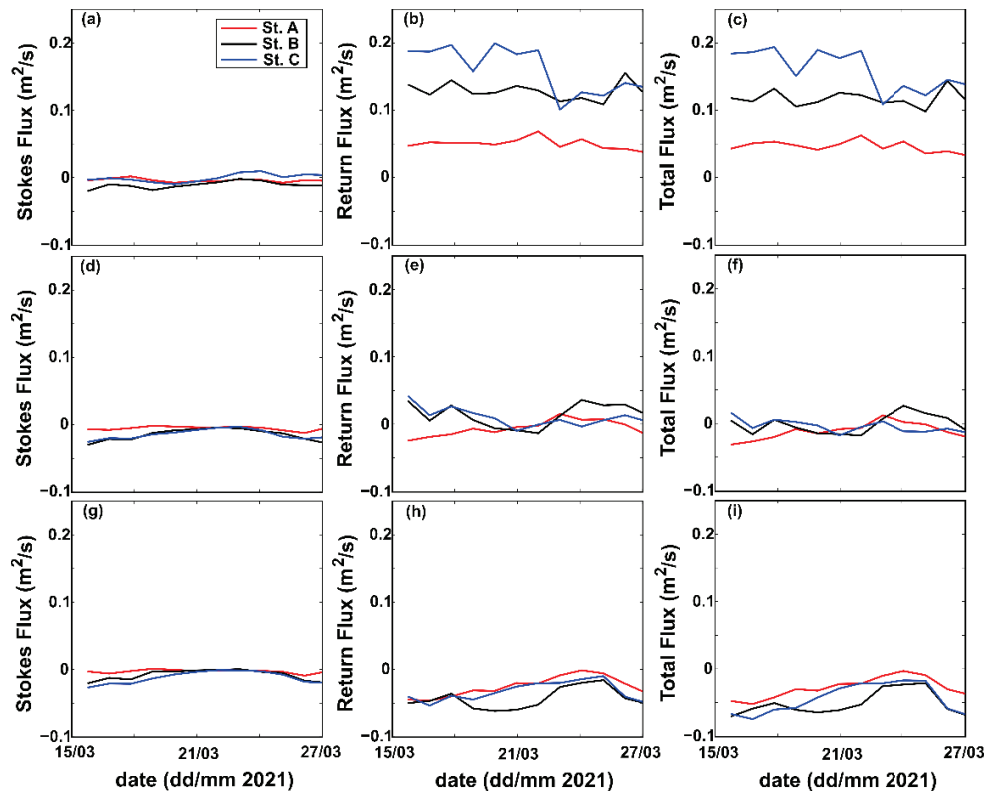

Figure 4.9 Stokes flux (a, d, g), return flux (b, e, h), and total flux (c, f, i) at upper (top row), mid- (middle row), and lower depth (bottom row) at Stations A, B, and C.

4.4 Discussions

Our analysis of subtidal friction and Stokes flux in low-discharge tidal channels identified distinct vertical variability in the orientation of subtidal flow-induced subtidal friction, the tidal–subtidal interaction term of subtidal friction, and return flux. Both subtidal friction terms vary from positive values near the surface to negative values near the bottom (Fig. 4.8), whereas the return flux indicates a seaward flux at the upper depth and a landward flux at a lower depth (Fig. 4.9). According to Eq. (4.7) and (4.10), the relationship between Fr, Frt, and the return flux is that they are similarly influenced by sub-tidal velocity. However, because the subtidal velocity in the Ota Diversion Channel is not necessarily associated with freshwater runoff, we deduced that the subtidal velocity in the channel can be influenced by the baroclinic effect. Through numerical simulations, Burchard and Hetland [16] demonstrated that estuarine circulation in a periodically stratified estuary with irrotational flow comprises gravitational circulation and tidal straining, with the latter being twice as large as the former. Moreover, previous studies on the Ota Diversion Channel have demonstrated the importance of tidal straining [72] and gravitational circulation [90]. However, because the mechanism of tidal straining involves the periodicity of stratification between the flood and ebb, which cannot be observed correctly in the subtidal period, we only considered gravitational circulation as the baroclinic effect.

Gravitational circulation is a physical mechanism generated in an estuary owing to the existence of a longitudinal density gradient in the estuarine channel [8]. This mechanism takes the form of a two-layer circulation that differs vertically in flow orientation. Gravitational circulation induces the seaward flow of low-density water on the surface and landward flow of high-density water near the bed. Owing to vertical variability, gravitational circulation is expected to permanently introduce stratification over the water column in the estuary. For a partially mixed estuary, the gravitational circulation can be expressed as [9]

$$0.031(g^2H^4/A\rho)(\partial\rho/\partial x)^2 \tag{4.10}$$

where g is gravitational acceleration (9.8 m/s^2), A is vertical eddy viscosity (m^2/s), ρ is water density (kg/m^3), and x is longitudinal distance (m). However, in this study, we could not estimate the eddy viscosity because of the limited density data in the vertical distribution and the insufficiencies of the temporal and

spatial resolutions of the current data in calculating the Reynolds shear stress. The return flux pattern shows the seaward surface and landward bottom fluxes. This vertical variability closely resembles the two-layer circulation flow of gravitational circulation. Additionally, Geyer and Macready [8] indicated that subtidal velocity, which is the influential driver of Fr, Frt, and return flux, can be associated with gravitational circulation. Hence, because we could not quantify gravitational circulation, and density stratification data were not available, we opted to use the near-bottom longitudinal density gradient term ($\partial\rho / \partial x$) as a proxy to show the influence of gravitational circulation.

Fig. 4.10 displays the longitudinal gradient of the near-bottom density between stations C and A at 10 min and subtidal intervals. Negative values of the density gradient indicate a higher density in the seaward direction, which prompts landward baroclinic flow over the lower depth of the water column along the Ota Diversion Channel. The temporal variation in the subtidal density gradient signifies the strong influence of the spring neap tide cycle on density distribution.
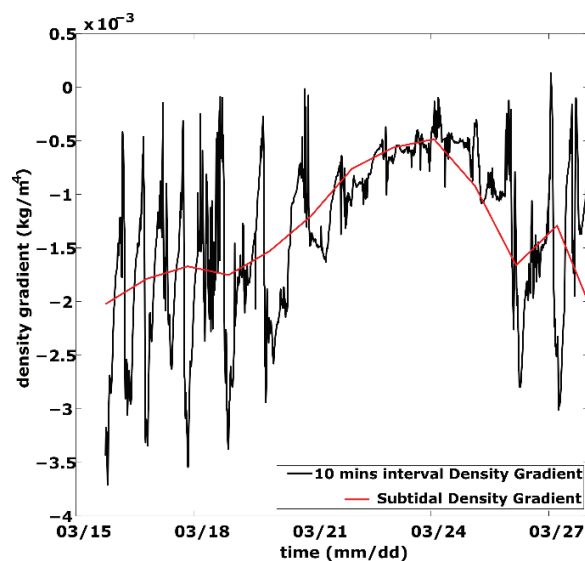
Figure 4.10 The longitudinal gradient of near-bottom density between Stations C and A. The red line depicts subtidal density gradient, while the black line depicts 10 min interval density gradient.

The correlation trends between Fr and Frt, while the longitudinal subtidal density gradient (Fig. 4.11) shows that Frt seems to steadily increase with a higher density gradient, whereas Fr has a more substantial increase for higher density gradients, particularly at stations A and C. Fig. 4.11 also displays the R^2 and p-values at each station. The Frt and density gradients are correlated at each station. On the other hand, although Fr and the density gradient are found to be highly correlated in the Stations A and C, more than with Frt, the R^2 value in Station B indicates poor correlation between both terms. Because the magnitude of the subtidal density gradient is significantly affected by the spring-neap tidal cycle, the low correlation of Fr at Station B could be attributed to the phase difference between the subtidal velocity at Station B and the other stations (Fig. 4.5d). These results suggest that the subtidal density gradient indeed modulates both Frt and Fr through the subtidal velocity, with a greater modulation potential in the latter.
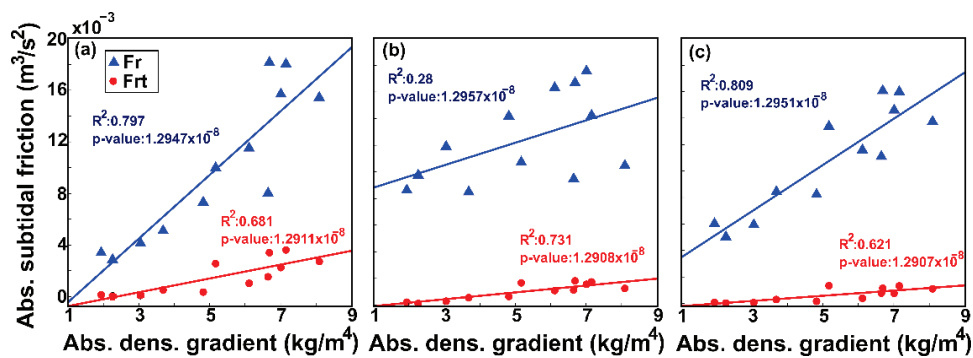
Figure 4.11 The longitudinal subtidal density gradient vs. Fr (blue triangles) and Frt (red dots) at Stations A (a), B (b), and C (c). The trendlines denote the linear relationship between the density gradient with Fr (blue lines) and Frt (red lines).

Fig. 4.12 presents the correlation trends, R^2, and p-values between the return flux and longitudinal subtidal density gradient. Similar to the subtidal friction terms, the return flux tended to increase with increasing density gradient magnitude. Likewise, the return fluxes at Stations A and C are found to be finely correlated with the density gradient, whereas that at Station B shows a poor correlation between both terms. The low correlation at Station B is likely caused by a greater value of return flux than that at the other stations during the period between the peak of the first spring tide and the lowest neap tide (Fig. 4.9h). As the difference

in the subtidal range between Station B and the other stations is not significant (Fig. 4.3), the higher value of the return flux could be attributed to the phase difference in the subtidal velocity at lower depths at Station B (Fig. 4.5d). This phase difference can be attributed to the bathymetry effect because Station B is situated in a small trough within the longitudinal orientation of the channel. Subsequently, this phase difference leads to a relatively higher subtidal velocity at Station B than that at the other stations, which induces a higher return flux.
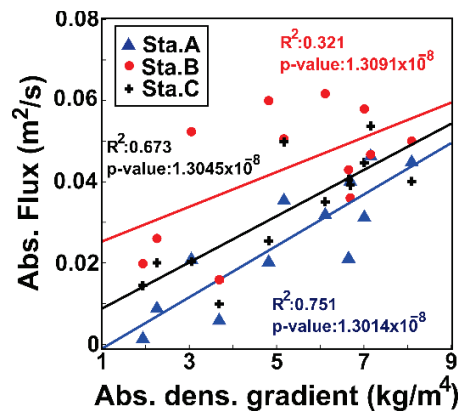
Figure 4.12 The longitudinal subtidal density gradient vs. return flux at Stations A (blue triangles), B (red dots), and C (black plus). The trendlines denote the linear relationship between the density gradient with return flux in each respective station.

Subtidal friction and discharge play important roles in determining the mean water level and mass transport in tidal channels [67]. Our results offer insights into the behavior of subtidal friction and subtidal discharge in tidal channels where freshwater runoff is limited (Fig. 4.8 and 4.9), and we demonstrate a correlation between the friction flux and the longitudinal density gradient (Fig. 4.10 and 4.11). The longitudinal density gradient has always been one of the main governing processes in tidal channels [74]. Furthermore, the longitudinal density gradient generates a baroclinic flow that regulates the influx of fine sediments into the tidal channels [121]. A continuous sediment influx from sea can lead to the introduction of a turbidity maximum zone within the tidal channel. Our results for the total flux between Stations A, B, and C indicate the existence of a turbidity maximum zone in the Ota Diversion Channel. Fig. 4.9f shows the convergence of the total flux near Station B at mid-depth during spring tide, supporting the findings of Xiao et al. [91].

Our findings suggest that the existence of a convergence zone in the Ota Diversion Channel is more likely to be caused by the total subtidal flux, which is strongly affected by baroclinic flow, rather than simply by river and tidal forcing.

Our study presents contrasting dominant mechanisms to similar studies that focus on high-discharge tidal rivers. High river discharge introduces a strong seaward runoff that could be more influential on the subtidal velocity than the longitudinal density gradient [33, 34, 105]. Subsequently, the river runoff directly affects Fr, Frt, and return flux through the term U_0 in high-discharge tidal rivers. More importantly, for subtidal friction, the product of the constant coefficient (a) and subtidal velocity (U_0) has the potential to be the mechanism makes the greatest contribution to subtidal friction [33]. However, the effects of high river discharge on the subtidal dynamics may not stop there. Studies in the Qiantang River, China [53, 122, 123] revealed that the interaction of high river discharge and tides could generate seasonal and interannual variations in bed morphology due to sediment erosion and accumulation. Although we did not focus on the effects of bathymetry on subtidal dynamics, our study indicates that bed morphology could affect the longitudinal variation of subtidal fluxes, particularly the Eulerian return flux. The relationship between bed morphology evolution and subtidal dynamics may provide significant information; however, owing to the time span of our data, this will be considered in future studies.

4.5 Conclusions

We conducted measurements to obtain temporal variations in water velocity and elevation at three longitudinal locations in the Ota Diversion Channel from 16 March to 28 March 2021. The data were evaluated using frequency domain and theoretical decomposition analyses to identify the behavior of the subtidal friction and subtidal flux in a low-discharge tidal river. Furthermore, we investigated the underlying mechanism that generates variability in the friction and flux orientations. Our study yielded several interesting findings.

First, the energy decay rates of the semidiurnal and diurnal tides between the current velocity and the water level were different. In essence, the Ota Diversion Channel is dominated by semidiurnal and diurnal tides,

with higher-frequency tides becoming more influential further upstream, owing to the energy transfer generated by the shallow-water interaction. The spectral analysis of the current velocity presents a more balanced energy distribution than the water level, particularly between overtides and diurnal tides. Second, by dividing the water column into three separate vertical depths, we found that the magnitude and sign orientation of Fr and Frt varied vertically in the low-discharge tidal river. The magnitude and pattern of Fr are closely associated with the subtidal velocity. Although Frt was also modulated by the subtidal velocity, to a certain extent, it was not as influential as the squared tidal velocity. Additionally, the subtidal friction in the Ota Diversion Channel was primarily driven by subtidal flow because its contribution was an order of magnitude higher than that of the tidal–subtidal interaction and subtidal friction. Third, in the case of the subtidal fluxes, vertical variability was apparent in the return flux. Generally, the return flux generated strong seaward transport, which diminished the seaward movement and eventually changed its transport orientation according to depth, starting from the downstream area of the channel. Furthermore, because the value of the return flux was greater than the Stokes flux, the total subtidal flux in the Ota Diversion Channel was not zero, and was significantly dominated by the return flux. Fourth, we discovered that the vertical variability of Fr, Frt, and return discharge in the low-discharge tidal channel was induced by a longitudinal subtidal density gradient through subtidal velocity. Additionally, Fr, Frt, and the return flux tended to have a greater magnitude, with a higher subtidal density difference between the upstream and downstream areas. An additional important finding of our study within the context of low-discharge tidal channels is that the total subtidal flux, which was governed by baroclinic flow, could lead to the formation of an estuarine convergence zone. This further signifies a unique behavior in a tidal channel with limited river discharge.

Although our study used a specific site in the Ota Diversion Channel as a case study, its analysis and results represented the distinct behavior of subtidal dynamics in a tidal river with low freshwater discharge. Hence, the results and discussion of our study can contribute to expanding our understanding of the river and tidal interaction dynamics in tidal rivers.

CHAPTER 5: Conclusions and Future works

5.1 Main Conclusions

The main purpose of this research was to investigate estuarine hydrodynamics in an artificial flood diversion channel that is subject to regulated river runoff conditions. Numerical simulations and observational field campaigns were conducted to examine the estuarine circulation mechanisms. The studies in this dissertation were conducted in the Ota Diversion Channel, a man-made channel with longitudinal variation in its geometry, located in the metropolitan area of Hiroshima, Japan. Although this study dealt with the Ota Diversion Channel as a case-specific example, the findings should increase the knowledge of common hydrodynamic processes in human-affected estuarine channels that have similar environments worldwide.

This research focused on (1) characterization of the underlying mechanisms in longitudinal and lateral estuarine circulation that are affected by flood control, and (2) investigation of the influential subtidal mechanisms that are generated by the longitudinal variation in channel geometry.

The specific conclusions and contributions of this study can be summarized as:

i.   A comparison of the numerical simulation scenarios with and without the flood gate presented different salinity structures in the Ota Diversion Channel. The omission of the Gion Flood gate led to a well-mixed structure generated by a stronger streamwise flow that shifted the saltwater intrusion upstream, particularly during flood tides. However, the existence of the Gion Flood Gate generated strong lateral and vertical stratification in the water column. Strong stratification subsequently led to a stronger baroclinic pressure gradient.

ii. The existence of the Gion Flood Gate exerts resistance to water flow, thus limiting the longitudinal flow. Consequently, the centrifugal force in the meandering area of the channel was limited, which resulted in the dominance of barotropic and baroclinic pressure gradients. The lateral flow in the meandering area of the Ota Diversion Channel was primarily generated by the interaction of both the pressure gradient terms. However, we also found that strong governing forces in the water circulation

do not always generated strong secondary flow because each governing force could counterbalance and nullify each other.

iii.   The longitudinal velocity profile indicated the existence of tidal asymmetry, in which ebb currents were dominant over flood currents. The asymmetry, which was induced by the interaction between the channel curvature and density gradient, was observed to be more enhanced in the curved channel than in the straight channel. Moreover, the across-channel bathymetry difference between curved and straight channels led to different patterns of lateral flow in those channels. Additionally, the longitudinal and lateral velocities averaged for the spring/neap tides revealed that the channel with a higher degree of curvature had greater residual circulation.

iv.   Tidal straining significantly affected the density structure in the Ota Diversion Channel, and its influence was greater during spring tides when tidal energy was relatively strong. On the other hand, tidal straining could be affected differently at different tidal phases by variations in the longitudinal geometry of the channel. Positive tidal straining, which enhanced mixing, was found to be more influential in straight channels during flooding. In contrast, strong negative tidal straining, which introduced stratification, was more influential at the ebb in the curved channel. Moreover, the longitudinal variation in channel geometry also affected the relative influence of tidal velocity and density gradient on the generation of tidal strain in the estuarine channel.

v.   The river effect, which permanently enhanced stratification, was stronger in the curved channel than in the straight channel. Additionally, the values of the river effect in the curved channel could be exponentially much stronger than those in the straight channel after a certain critical discharge value.

vi.   Tidal stirring was the most dominant forcing in the Ota Diversion Channel after tidal straining. This indicated a unique behavior in the context of small mesotidal estuarine channels that are affected by human intervention, as tidal stirring was not commonly known to be able to compensate for tidal straining in other estuarine environments.

vii.   The tidal energy in the Ota Diversion Channel was influenced mainly by semidiurnal and diurnal tides. Further upstream, overtides became more influential because of the transfer of tidal energy due to

shallow-water interaction. More importantly, spectral analysis indicated a more balanced energy distribution in the current velocity than in the water level. This implied that the rate of energy transfer due to the shallow water interaction for the current velocity was stronger than that for the water elevation.

viii. Subtidal friction decomposition analysis indicated that the subtidal friction in the Ota Diversion Channel was dominated by the influence of subtidal flow-induced subtidal friction, which was an order of magnitude higher than that of the tidal–subtidal interaction and tidal asymmetry. Additionally, vertical separation of the water column presented vertical variations in Fr and Frt. Similar to subtidal friction, vertical variability was also observed in the Eulerian return flux. Moreover, because the Eulerian return flux was dominant over the Stokes flux, the total subtidal flux in the Ota Diversion Channel was not zero and the subtidal transport in this channel was dominated by seaward movement.

ix. The vertical variabilities of Fr, Frt, and return flux were strongly associated with the subtidal density gradient. The subtidal density gradient governed these mechanisms through the subtidal velocity, which, in the case of the Ota Diversion Channel, was minimally influenced by river runoff, unlike in other estuarine environments. Additionally, the total subtidal flux in estuaries, similar to the Ota Diversion Channel, could lead to the formation of an estuarine convergence zone due to the vertical and longitudinal variability of the flux.

5.2 Future Works

The research is ongoing, and an enormous number of points must be investigated; however, additional future investigations are suggested as follows:

- Examining lateral, longitudinal, and vertical structures of water current, density, and sediment concentration are highly recommended to comprehensively understand the impacts of the flood control structure and variation in channel geometry on the spatial variation of tidal-induced hydrodynamics and the associated morphological evolution in small mesotidal estuaries.

- It is recommended to conduct an extended study as minimum as a full hydrological year to examine the seasonal effects and how its interactions with human interventions in the Ota River Estuary affect estuarine circulation and mixing. Additionally, our study indicated that bed morphology can influence the spatial variation of the subtidal flux in the channel. Hence, a study using numerical simulation over a prolonged time span (years or decades) is suggested to examine the relationship between human intervention, bed morphology evolution, and associated subtidal dynamics.

References

[1]   K.R. Dyer, Estuaries: A Physical Introduction, 2nd edition, Chichester, UK, 1997.

[2]   J.P.M. Syvitski, A.J. Kettner, I. Overeem, E.W.H. Hutton, M.T. Hannon, G.R. Brakenridge, J. Day, C. Vörösmarty, Y. Saito, L. Giosan, R.J. Nicholls, Sinking deltas due to human activities, Nat. Geosci. 2 (2009) 681–686. https://doi.org/10.1038/ngeo629.

[3]   T. Gotoh, S. Fukuoka, Y. Miyagawa, Topographic changes of tidal flats in the Ota River estuary by flood flows, Adv. River Sediment Res. (2013) 1337–1345.

[4]   M.B. Al Sawaf, K. Kawanisi, C. Xiao, Characterizing annual flood patterns variation using information and complexity indices, Sci. Total Environ. 806 (2022) 151382. https://doi.org/10.1016/j.scitotenv.2021.151382.

[5]   P. MacCready, W.R. Geyer, Advances in estuarine physics, Ann. Rev. Mar. Sci. 2 (2010) 35–58. https://doi.org/10.1146/annurev-marine-120308-081015.

[6]   W. Pritchard, F. Estuary, F. Water, Estuarine Hydrography, Adv. Geophys. 1 (n.d.) 243–280.

[7]   D. V. Hansen, M. Rattray, Gravitational Circulation in Straits and Estuaries, J. Mar. Res. (1965) 104–122.

[8]   W.R. Geyer, P. MacCready, The estuarine circulation, Annu. Rev. Fluid Mech. 46 (2014) 175–197. https://doi.org/10.1146/annurev-fluid-010313-141302.

[9]   X. Pu, J.Z. Shi, G.D. Hu, L.B. Xiong, Circulation and mixing along the North Passage in the Changjiang River estuary, China, J. Mar. Syst. 148 (2015) 213–235. https://doi.org/10.1016/j.jmarsys.2015.03.009.

[10]   J.H. Simpson, J. Brown, J. Matthews, G. Allen, Tidal straining, density currents, and stirring in the control of estuarine stratification, Estuaries. 13 (1990) 125–132. https://doi.org/10.2307/1351581.

References

[11]   M.T. Stacey, S.G. Monismith, Creation of residual flows in a partially stratified estuary, J. Geophys. Res. 106 (2001) 17013–17037.

[12]   M.T. Stacey, M.L. Brennan, J.R. Burau, S.G. Monismith, The tidally averaged momentum balance in a partially and periodically stratified estuary, J. Phys. Oceanogr. 40 (2010) 2418–2434. https://doi.org/10.1175/2010JPO4389.1.

[13]   E. Garel, L. Pinto, A. Santos, Ó. Ferreira, Tidal and river discharge forcing upon water and sediment circulation at a rock-bound estuary (Guadiana estuary, Portugal), Estuar. Coast. Shelf Sci. 84 (2009) 269–281. https://doi.org/10.1016/j.ecss.2009.07.002.

[14]   J. Becherer, H. Burchard, G. Flöser, V. Mohrholz, L. Umlauf, Evidence of tidal straining in well-mixed channel flow from micro-structure observations, Geophys. Res. Lett. 38 (2011) 2–6. https://doi.org/10.1029/2011GL049005.

[15]   J. Wang, L. Li, Z. He, N.A. Kalhoro, D. Xu, Numerical modelling study of seawater intrusion in Indus River Estuary, Pakistan, Ocean Eng. 184 (2019) 74–84. https://doi.org/10.1016/j.oceaneng.2019.05.029.

[16]   H. Burchard, R.D. Hetland, Quantifying the contributions of tidal straining and gravitational circulation to residual circulation in periodically stratified tidal estuaries, J. Phys. Oceanogr. 40 (2010) 1243–1262. https://doi.org/10.1175/2010JPO4270.1.

[17]   H. Burchard, H. Baumert, The formation of estuarine turbidity maxima due to density effects in the salt wedge. A hydrodynamic process study, J. Phys. Oceanogr. 28 (1998) 309–321. https://doi.org/10.1175/1520-0485(1998)028<0309:TFOETM>2.0.CO;2.

[18]   M.G. Sassi, A.J.F. Hoitink, B. De Brye, E. Deleersnijder, Downstream hydraulic geometry of a tidally influenced river delta, J. Geophys. Res. F Earth Surf. 117 (2012) 1–13. https://doi.org/10.1029/2012JF002448.

References

[19]   N. Leonardi, A.S. Kolker, S. Fagherazzi, Interplay between river discharge and tides in a delta

        distributary, Adv. Water Resour. 80 (2015) 69–78.

        https://doi.org/10.1016/j.advwatres.2015.03.005.

[20]   R.A. Nunes, J.H. Simpson, Axial convergence in a well-mixed estuary, Estuar. Coast. Shelf Sci.

        20 (1985) 637–649. https://doi.org/10.1016/0272-7714(85)90112-X.

[21]   L. He, Distribution of primary and secondary currents in sine-generated bends, Water SA. 44

        (2018) 118–129. https://doi.org/10.4314/wsa.v44i1.14.

[22]   W.R. Geyer, Three-dimensional tidal flow around headlands, J. Geophys. Res. 98 (1993) 955–966.

[23]   R.J. Chant, Secondary circulation in a highly stratified estuary, J. Geophys. Res. C Ocean. 102

        (1997) 23207–23215. https://doi.org/10.1029/97JC00685.

[24]   M.E. Scully, W.R. Geyer, The Role of Advection, Straining, and Mixing on the Tidal Variability

        of Estuarine Stratification, J. Phys. Oceanogr. 42 (2012) 855–868. https://doi.org/10.1175/JPO-D-

        10-05010.1.

[25]   J.A. Lerczak, W.R. Geyer, Modeling the lateral circulation in straight, stratified estuaries, J. Phys.

        Oceanogr. 34 (2004) 1410–1428. https://doi.org/10.1175/1520-

        0485(2004)034<1410:MTLCIS>2.0.CO;2.

[26]   P.E. Speer, D.G. Aubrey, A study of non-linear tidal propagation in shallow inlet/estuarine

        systems Part I: Observations, Estuar. Coast. Shelf Sci. 21 (1985) 207–224.

        https://doi.org/10.1016/0272-7714(85)90097-6.

[27]   J. Dronkers, Tidal asymmetry and estuarine morphology, Netherlands J. Sea Res. 20 (1986) 117–

        131. https://doi.org/10.1016/0077-7579(86)90036-0.

[28]   P. Matte, D.A. Jay, E.D. Zaron, Adaptation of classical tidal harmonic analysis to nonstationary

        tides, with application to river tides, J. Atmos. Ocean. Technol. 30 (2013) 569–589.

References

https://doi.org/10.1175/JTECH-D-12-00016.1.

[29] P. Matte, Y. Secretan, J. Morin, Drivers of residual and tidal flow variability in the St. Lawrence fluvial estuary: Influence on tidal wave propagation, Cont. Shelf Res. 174 (2019) 158–173. https://doi.org/10.1016/j.csr.2018.12.008.

[30] G. Godin, The propagation of tides up rivers with special considerations on the upper Saint Lawrence river, Estuar. Coast. Shelf Sci. 48 (1999) 307–324. https://doi.org/10.1006/ecss.1998.0422.

[31] G. Godin, A. Martinez, Friction on the Propagation O F Tides in a Channel, Cont. Shelf Res. 14 (1994) 723–748.

[32] A.E. Yankovsky, S.K. Iyer, Propagation of subtidal sea level oscillations in the river channel: A case study of the St. Johns River, Florida, USA., Estuar. Coast. Shelf Sci. 157 (2015) 69–78. https://doi.org/10.1016/j.ecss.2015.02.012.

[33] F.A. Buschman, A.J.F. Hoitink, M. Van Der Vegt, P. Hoekstra, Subtidal water level variation controlled by river flow and tides, Water Resour. Res. 45 (2009). https://doi.org/10.1029/2009WR008167.

[34] M.G. Sassi, A.J.F. Hoitink, River flow controls on tides and tide-mean water level profiles in a tidal freshwater river, J. Geophys. Res. Ocean. 118 (2013) 4139–4151. https://doi.org/10.1002/jgrc.20297.

[35] Y. Wu, C. Hannah, P. Matte, M. O'Flaherty-Sproul, R. Mo, X. Wang, P. MacAulay, Tidal propagation in the Lower Fraser River, British Columbia, Canada, Estuar. Coast. Shelf Sci. 264 (2022) 107695. https://doi.org/10.1016/j.ecss.2021.107695.

[36] J. Syvitski, C.N. Waters, J. Day, J.D. Milliman, C. Summerhayes, W. Steffen, J. Zalasiewicz, A. Cearreta, A. Gałuszka, I. Hajdas, M.J. Head, R. Leinfelder, J.R. McNeill, C. Poirier, N.L. Rose,

References

W. Shotyk, M. Wagreich, M. Williams, Extraordinary human energy consumption and resultant geological impacts beginning around 1950 CE initiated the proposed Anthropocene Epoch, Commun. Earth Environ. 1 (2020) 1–13. https://doi.org/10.1038/s43247-020-00029-y.

[37]   C. Ferrarin, A. Tomasin, M. Bajo, A. Petrizzo, G. Umgiesser, Tidal changes in a heavily modified coastal wetland, Cont. Shelf Res. 101 (2015) 22–33. https://doi.org/10.1016/j.csr.2015.04.002.

[38]   R.L. Bain, R.P. Hale, S.L. Goodbred, Flow Reorganization in an Anthropogenically Modified Tidal Channel Network: An Example From the Southwestern Ganges-Brahmaputra-Meghna Delta, J. Geophys. Res. Earth Surf. 124 (2019) 2141–2159. https://doi.org/10.1029/2018JF004996.

[39]   J. Dronkers, Convergence of estuarine channels, Cont. Shelf Res. 144 (2017) 120–133. https://doi.org/10.1016/j.csr.2017.06.012.

[40]   J.C. Winterwerp, Z.B. Wang, A. Van Braeckel, G. Van Holland, F. Kösters, Man-induced regime shifts in small estuaries - II: A comparison of rivers, Ocean Dyn. 63 (2013) 1293–1306. https://doi.org/10.1007/s10236-013-0663-8.

[41]   J. Zhu, R.H. Weisberg, L. Zheng, S. Han, Influences of Channel Deepening and Widening on the Tidal and Nontidal Circulations of Tampa Bay, Estuaries and Coasts. 38 (2015) 132–150. https://doi.org/10.1007/s12237-014-9815-4.

[42]   R. Familkhalili, S.A. Talke, The effect of channel deepening on tides and storm surge: A case study of Wilmington, NC, Geophys. Res. Lett. 43 (2016) 9138–9147. https://doi.org/10.1002/2016GL069494.

[43]   D.K. Ralston, S. Talke, W.R. Geyer, H.A.M. Al-Zubaidi, C.K. Sommerfield, Bigger Tides, Less Flooding: Effects of Dredging on Barotropic Dynamics in a Highly Modified Estuary, J. Geophys. Res. Ocean. 124 (2019) 196–211. https://doi.org/10.1029/2018JC014313.

[44]   S. Bao, W. Zhang, J. Qin, J. Zheng, H. Lv, X. Feng, Y. Xu, A.J.F. Hoitink, Peak Water Level

References

Response to Channel Deepening Depends on Interaction Between Tides and the River Flow, J. Geophys. Res. Ocean. 127 (2022). https://doi.org/10.1029/2021JC017625.

[45]   V.N. De Jonge, H.M. Schuttelaars, J.E.E. van Beusekom, S.A. Talke, H.E. de Swart, The influence of channel deepening on estuarine turbidity levels anddynamics, as exemplified by the Ems estuary, Estuar. Coast. Shelf Sci. 139 (2014) 46–59. https://doi.org/10.1016/j.ecss.2013.12.030.

[46]   R.J. Chant, C.K. Sommerfield, S.A. Talke, Impact of Channel Deepening on Tidal and Gravitational Circulation in a Highly Engineered Estuarine Basin, Estuaries and Coasts. 41 (2018) 1587–1600. https://doi.org/10.1007/s12237-018-0379-6.

[47]   D.K. Ralston, W.R. Geyer, Response to Channel Deepening of the Salinity Intrusion, Estuarine Circulation, and Stratification in an Urbanized Estuary, J. Geophys. Res. Ocean. 124 (2019) 4784–4802. https://doi.org/10.1029/2019JC015006.

[48]   W. Wei, Z. Dai, X. Mei, J.P. Liu, S. Gao, S. Li, Shoal morphodynamics of the Changjiang (Yangtze) estuary: Influences from river damming, estuarine hydraulic engineering and reclamation projects, Mar. Geol. 386 (2017) 32–43. https://doi.org/10.1016/j.margeo.2017.02.013.

[49]   M. Zhang, I. Townend, Y. Zhou, L. Wang, Z. Dai, An examination of estuary stability in response to human interventions in the South Branch of the Yangtze (Changjiang) estuary, China, Estuar. Coast. Shelf Sci. 228 (2019) 106383. https://doi.org/10.1016/j.ecss.2019.106383.

[50]   Q. Yang, S. Hu, L. Fu, P. Zhang, Responses of tidal duration asymmetry to morphological changes in Lingding Bay of the Pearl River Estuary, Front. Mar. Sci. (2022) 1–19. https://doi.org/10.3389/fmars.2022.983182.

[51]   W. Gong, Y. Wang, J. Jia, The effect of interacting downstream branches on saltwater intrusion in the Modaomen Estuary, China, J. Asian Earth Sci. 45 (2012) 223–238.

References

https://doi.org/10.1016/j.jseaes.2011.11.001.

[52]   N.E. Vellinga, A.J.F. Hoitink, M. van der Vegt, W. Zhang, P. Hoekstra, Human impacts on tides overwhelm the effect of sea level rise on extreme water levels in the Rhine-Meuse delta, Coast. Eng. 90 (2014) 40–50. https://doi.org/10.1016/j.coastaleng.2014.04.005.

[53]   D. Xie, Z. Bing Wang, J. Huang, J. Zeng, River, tide and morphology interaction in a macro-tidal estuary with active morphological evolutions, Catena. 212 (2022) 106131. https://doi.org/10.1016/j.catena.2022.106131.

[54]   H. Cai, X. Zhang, M. Zhang, L. Guo, F. Liu, Q. Yang, Impacts of Three Gorges Dam's operation on spatial-temporal patterns of tide-river dynamics in the Yangtze River estuary, China, Ocean Sci. 15 (2019) 583–599. https://doi.org/10.5194/os-15-583-2019.

[55]   C. Bakker, M. Vink, Nutrient concentrations and planktonic diatom-flagellate relations in the Oosterschelde (SW Netherlands) during and after the construction of a storm-surge barrier, Hydrobiologia. 282–283 (1994) 101–116. https://doi.org/10.1007/BF00024624.

[56]   J. Du, J. Shen, D.M. Bilkovic, C.H. Hershner, M. Sisson, A Numerical Modeling Approach to Predict the Effect of a Storm Surge Barrier on Hydrodynamics and Long-Term Transport Processes in a Partially Mixed Estuary, Estuaries and Coasts. 40 (2017) 387–403. https://doi.org/10.1007/s12237-016-0175-0.

[57]   L. Li, J. Zhu, R.J. Chant, C. Wang, L.F. Pareja-Roman, Effect of Dikes on Saltwater Intrusion Under Various Wind Conditions in the Changjiang Estuary, J. Geophys. Res. Ocean. 125 (2020) 1–25. https://doi.org/10.1029/2019JC015685.

[58]   Z. Liu, Y.J. Zhang, H. V. Wang, H. Huang, Z. Wang, F. Ye, M. Sisson, Impact of small-scale structures on estuarine circulation, Ocean Dyn. 68 (2018) 509–533. https://doi.org/10.1007/s10236-018-1148-6.

References

[59]   M. Razaz, K. Kawanisi, I. Nistor, S. Sharifi, An acoustic travel time method for continuous

         velocity monitoring in shallow tidal streams, Water Resour. Res. 49 (2013) 4885–4899.

         https://doi.org/10.1002/wrcr.20375.

[60]   K. Kawanisi, Structure of Turbulent Flow in a Shallow Tidal Estuary, J. Hydraul. Eng. 130 (2004)

         1013–1024. https://doi.org/10.1061/(ASCE)0733-9429(2004)130.

[61]   J. Pein, A. Valle-Levinson, E. V. Stanev, Secondary Circulation Asymmetry in a Meandering,

         Partially Stratified Estuary, J. Geophys. Res. Ocean. 123 (2018) 1670–1683.

         https://doi.org/10.1002/2016JC012623.

[62]   R.J. Chant, Secondary circulation in a region of flow curvature: Relationship with tidal forcing and

         river discharge, J. Geophys. Res. C Ocean. 107 (2002) 14–1.

         https://doi.org/10.1029/2001jc001082.

[63]   N.J. Nidzieko, J.L. Hench, S.G. Monismith, Lateral circulation in well-mixed and stratified

         estuarine flows with curvature, J. Phys. Oceanogr. 39 (2009) 831–851.

         https://doi.org/10.1175/2008JPO4017.1.

[64]   P. Parsapour-Moghaddam, C.D. Rennie, J. Slaney, Hydrodynamic Simulation of an Irregularly

         Meandering Gravel-Bed River: Comparison of MIKE 21 FM and Delft3D Flow models, E3S Web

         Conf. 40 (2018) 1–8. https://doi.org/10.1051/e3sconf/20184002004.

[65]   H. de Pablo, J. Sobrinho, M. Garcia, F. Campuzano, M. Juliano, R. Neves, Validation of the 3D-

         MOHID hydrodynamic model for the Tagus coastal area, Water (Switzerland). 11 (2019).

         https://doi.org/10.3390/w11081713.

[66]   E. Kasvi, L. Laamanen, E. Lotsari, P. Alho, Flow patterns and morphological changes in a sandy

         meander bend during a flood-spatially and temporally intensive ADCP measurement approach,

         Water (Switzerland). 9 (2017) 6–11. https://doi.org/10.3390/w9020106.

References

[67]   A.J.F. Hoitink, D.A. Jay, Tidal river dynamics: Implications for deltas, Rev. Geophys. 54 (2016) 240–272. https://doi.org/10.1002/2015RG000507.

[68]   J. Becherer, M.T. Stacey, L. Umlauf, H. Burchard, Lateral circulation generates flood tide stratification and estuarine exchange flow in a curved tidal inlet, J. Phys. Oceanogr. 45 (2015) 638–656. https://doi.org/10.1175/JPO-D-14-0001.1.

[69]   H. Burchard, H.M. Schuttelaars, Analysis of tidal straining as driver for estuarine circulation in well-mixed estuaries, J. Phys. Oceanogr. 42 (2012) 261–271. https://doi.org/10.1175/JPO-D-11-0110.1.

[70]   W. Gong, L. Jia, J. Shen, J.T. Liu, Sediment transport in response to changes in river discharge and tidal mixing in a funnel-shaped micro-tidal estuary, Cont. Shelf Res. 76 (2014) 89–107. https://doi.org/10.1016/j.csr.2014.01.006.

[71]   D.A. Jay, J.D. Musiak, Particle trapping in estuarine tidal flows, J. Geophys. Res. 99 (1994). https://doi.org/10.1029/94jc00971.

[72]   K. Kawanishi, Variability of tidal current, density stratification and tidal flat sediment in a tidal river, WIT Trans. Ecol. Environ. 88 (2006) 129–138. https://doi.org/10.2495/CENV060131.

[73]   L. Zhu, Q. He, J. Shen, Modeling lateral circulation and its influence on the along-channel flow in a branched estuary, Ocean Dyn. 68 (2018) 177–191. https://doi.org/10.1007/s10236-017-1114-8.

[74]   H. Burchard, R.D. Hetland, E. Schulz, H.M. Schuttelaars, Drivers of residual estuarine circulation in tidally energetic estuaries: Straight and irrotational channels with parabolic cross section, J. Phys. Oceanogr. 41 (2011) 548–570. https://doi.org/10.1175/2010JPO4453.1.

[75]   S. Kobayashi, J.H. Simpson, T. Fujiwara, K.J. Horsburgh, Tidal stirring and its impact on water column stability and property distributions in a semi-enclosed shelf sea (Seto Inland Sea, Japan), Cont. Shelf Res. 26 (2006) 1295–1306. https://doi.org/10.1016/j.csr.2006.04.006.

References

[76]   S.N. Chen, L.P. Sanford, Axial wind effects on stratification and longitudinal salt transport in an idealized, partially mixed estuary, J. Phys. Oceanogr. 39 (2009) 1905–1920. https://doi.org/10.1175/2009JPO4016.1.

[77]   W. Lai, J. Pan, A.T. Devlin, Impact of tides and winds on estuarine circulation in the Pearl River Estuary, Cont. Shelf Res. 168 (2018) 68–82. https://doi.org/10.1016/j.csr.2018.09.004.

[78]   X. Lange, K. Klingbeil, H. Burchard, Inversions of Estuarine Circulation Are Frequent in a Weakly Tidal Estuary With Variable Wind Forcing and Seaward Salinity Fluctuations, J. Geophys. Res. Ocean. 125 (2020). https://doi.org/10.1029/2019JC015789.

[79]   X. Lange, H. Burchard, The relative importance of wind straining and gravitational forcing in driving exchange flows in tidally energetic estuaries, J. Phys. Oceanogr. 49 (2019) 723–736. https://doi.org/10.1175/JPO-D-18-0014.1.

[80]   M. Li, W. Liu, R. Chant, A. Valle-Levinson, Flood-ebb and spring-neap variations of lateral circulation in the James River estuary, Cont. Shelf Res. 148 (2017) 9–18. https://doi.org/10.1016/j.csr.2017.09.007.

[81]   M.I. Morell, P.A. Tassi, C.A. Vionnet, Flow pattern at a river diffluence at the alluvial system of the Paraná River, J. Appl. Water Eng. Res. 2 (2014) 140–156. https://doi.org/10.1080/23249676.2014.981371.

[82]   B.P. Paiva, E. Siegle, C.A.F. Schettini, Channel curvature effects on estuarine circulation in a highly stratified tropical estuary: The São Francisco river estuary (Brazil), Estuar. Coast. Shelf Sci. 238 (2020). https://doi.org/10.1016/j.ecss.2020.106723.

[83]   M.C. Buijsman, H. Ridderinkhof, Variability of secondary currents in a weakly stratified tidal inlet with low curvature, Cont. Shelf Res. 28 (2008) 1711–1723. https://doi.org/10.1016/j.csr.2008.04.001.

References

[84]   L. Chen, W. Gong, H. Zhang, L. Zhu, W. Cheng, Lateral Circulation and Associated Sediment Transport in a Convergent Estuary, J. Geophys. Res. Ocean. 125 (2020) 1–23. https://doi.org/10.1029/2019jc015926.

[85]   P. Cheng, R.E. Wilson, R.J. Chant, D.C. Fugate, R.D. Flood, Modeling influence of stratification on lateral circulation in a stratified estuary, J. Phys. Oceanogr. 39 (2009) 2324–2337. https://doi.org/10.1175/2009JPO4157.1.

[86]   Y.H. Kim, G. Voulgaris, Lateral circulation and suspended sediment transport in a curved estuarine channel: Winyah Bay, SC, USA, J. Geophys. Res. Ocean. 113 (2008) 1–15. https://doi.org/10.1029/2007JC004509.

[87]   W.M. Kranenburg, W.R. Geyer, A.M.P. Garcia, D.K. Ralston, Reversed lateral circulation in a sharp estuarine bend with weak stratification, J. Phys. Oceanogr. 49 (2019) 1619–1637. https://doi.org/10.1175/JPO-D-18-0175.1.

[88]   R. Lacy, G. Monismith, Secondary currents in a curved, stratified, estuarine channel, J. Geophys. Res. 106 (2001) 31283–31302.

[89]   K. Kawanisi, M. Razaz, A. Kaneko, S. Watanabe, Long-term measurement of stream flow and salinity in a tidal river by the use of the fluvial acoustic tomography system, J. Hydrol. 380 (2010) 74–81. https://doi.org/10.1016/j.jhydrol.2009.10.024.

[90]   M. Soltaniasl, K. Kawanisi, J. Yano, K. Ishikawa, Variability in salt flux and water circulation in Ota River Estuary, Japan, Water Sci. Eng. 6 (2013) 283–295. https://doi.org/10.3882/j.issn.1674-2370.2013.03.005.

[91]   C. Xiao, K. Kawanisi, M.B. Al Sawaf, Suspended particulate matter concentration in response to tidal hydrodynamics in a long mesotidal floodway, Estuar. Coast. Shelf Sci. 233 (2020) 106525. https://doi.org/10.1016/j.ecss.2019.106525.

References

[92]   L. Grunberg, Properties of seawater concentrates, in: Third Int. Symp. Fresh Water from Sea, 1970: pp. 31–39.

[93]   J.H. Simpson, D. Bowers, Models of stratification and frontal movement in shelf seas, Deep Sea Res. Part A, Oceanogr. Res. Pap. 28 (1981) 727–738. https://doi.org/10.1016/0198-0149(81)90132-1.

[94]   J. Wu, J.T. Liu, X. Wang, Sediment trapping of turbidity maxima in the Changjiang Estuary, Mar. Geol. 303–306 (2012) 14–25. https://doi.org/10.1016/j.margeo.2012.02.011.

[95]   H. Perales-Valdivia, R. Sanay-González, A. Valle-Levinson, Effects of tides, wind and river discharge on the salt intrusion in a microtidal tropical estuary, Reg. Stud. Mar. Sci. 24 (2018) 400–410. https://doi.org/10.1016/j.rsma.2018.10.001.

[96]   S. Eslami, P. Hoekstra, H.W.J. Kernkamp, N. Nguyen Trung, D. Do Duc, H. Nguyen Nghia, T. Tran Quang, A. Van Dam, S.E. Darby, D.R. Parsons, G. Vasilopoulos, L. Braat, M. Van Der Vegt, Dynamics of salt intrusion in the Mekong Delta: Results of field observations and integrated coastal-inland modelling, Earth Surf. Dyn. 9 (2021) 953–976. https://doi.org/10.5194/esurf-9-953-2021.

[97]   A. Barendregt, C.W. Swarth, Tidal Freshwater Wetlands: Variation and Changes, Estuaries and Coasts. 36 (2013) 445–456. https://doi.org/10.1007/s12237-013-9626-z.

[98]   A.T. Fricke, C.A. Nittrouer, A.S. Ogston, D.J. Nowacki, N.E. Asp, P.W.M. Souza Filho, Morphology and dynamics of the intertidal floodplain along the Amazon tidal river, Earth Surf. Process. Landforms. 44 (2019) 204–218. https://doi.org/10.1002/esp.4545.

[99]   B. Camenen, N. Gratiot, J.A. Cohard, F. Gard, V.Q. Tran, A.T. Nguyen, G. Dramais, T. van Emmerik, J. Némery, Monitoring discharge in a tidal river using water level observations: Application to the Saigon River, Vietnam, Sci. Total Environ. 761 (2021) 143195.

References

https://doi.org/10.1016/j.scitotenv.2020.143195.

[100] K. Haralambidou, G. Sylaios, V.A. Tsihrintzis, Salt-wedge propagation in a Mediterranean micro-
       tidal river mouth, Estuar. Coast. Shelf Sci. 90 (2010) 174–184.
       https://doi.org/10.1016/j.ecss.2010.08.010.

[101] S. Sarker, A Short Review on Computational Hydraulics in the Context of Water Resources
       Engineering, Open J. Model. Simul. 10 (2022) 1–31. https://doi.org/10.4236/ojmsi.2022.101001.

[102] H. Cai, H.H.G. Savenije, C. Jiang, Analytical approach for predicting fresh water discharge in an
       estuary based on tidal water level observations, Hydrol. Earth Syst. Sci. 18 (2014) 4153–4168.
       https://doi.org/10.5194/hess-18-4153-2014.

[103] A.A. Reza, S. Sarker, S.A. Asha, an Application of 1-D Momentum Equation To Calculate
       Discharge in Tidal River: a Case Study on Kaliganga River, Tech. J. River Res. Inst. (2014).

[104] L. Guo, M. van der Wegen, D.A. Jay, P. Matte, Z.B. Wang, D. Roelvink, Q. He, Journal of
       Geophysical Research : Oceans nonlinear tidal behavior in the Yangtze River estuary, J. Geophys.
       Res. C Ocean. 120 (2015) 3499–3521. https://doi.org/10.1002/2014JC010491.Received.

[105] F.A. Buschman, A.J.F. Hoitink, M. Van Der Vegt, P. Hoekstra, Subtidal flow division at a shallow
       tidal junction, Water Resour. Res. 46 (2010). https://doi.org/10.1029/2010WR009266.

[106] M.G. Sassi, A.J.F. Hoitink, B. De Brye, B. Vermeulen, E. Deleersnijder, Tidal impact on the
       division of river discharge over distributary channels in the Mahakam Delta, Ocean Dyn. 61
       (2011) 2211–2228. https://doi.org/10.1007/s10236-011-0473-9.

[107] A. Wünchow, A.K. Masse, R.W. Garvine, Astronomical and nonlinear tidal currents in a coupled
       estuary shelf system, Cont. Shelf Res. 12 (1992) 471–498. https://doi.org/10.1016/0278-
       4343(92)90087-Z.

[108] W. Zhang, H. Feng, A.J.F. Hoitink, Y. Zhu, F. Gong, J. Zheng, Tidal impacts on the subtidal flow

References

division at the main bifurcation in the Yangtze River Delta, Estuar. Coast. Shelf Sci. 196 (2017) 301–314. https://doi.org/10.1016/j.ecss.2017.07.008.

[109] W. Zhang, H. Feng, Y. Zhu, J. Zheng, A.J.F. Hoitink, Subtidal Flow Reversal Associated With Sediment Accretion in a Delta Channel, Water Resour. Res. 55 (2019) 10781–10795. https://doi.org/10.1029/2019WR025945.

[110] Wahyudin, T. Yamamoto, Modeling bottom-up and top-down controls on the low recruitment success of oyster larvae in Hiroshima Bay, Japan, Aquaculture. 529 (2020) 735564. https://doi.org/10.1016/j.aquaculture.2020.735564.

[111] H.T. Nguyen, K. Kawanisi, M.B. Al Sawaf, Acoustic monitoring of tidal flow and salinity in a tidal channel, J. Mar. Sci. Eng. 9 (2021). https://doi.org/10.3390/jmse9111180.

[112] K. Kawanisi, Evaluation of M-Y closure model in tidal estuary with turbulence data from high-resolution current profiler, WIT Trans. Built Environ. 70 (2003) 101–110.

[113] F. Khadami, K. Kawanisi, M.B. Al Sawaf, G.N.N. Gusti, C. Xiao, Spatiotemporal Response of Currents and Mixing to the Interaction of Tides and River Runoff in a Mesotidal Estuary, Ocean Sci. J. (2022). https://doi.org/10.1007/s12601-022-00056-0.

[114] M. Razaz, K. Kawanisi, Turbulence characteristics in the bottom layer of a shallow tidal channel, J. Turbul. 13 (2012) 1–22. https://doi.org/10.1080/14685248.2012.741322.

[115] D.A. Jay, K. Leffler, H.L. Diefenderfer, A.B. Borde, Tidal-Fluvial and Estuarine Processes in the Lower Columbia River: I. Along-Channel Water Level Variations, Pacific Ocean to Bonneville Dam, Estuaries and Coasts. 38 (2015) 415–433. https://doi.org/10.1007/s12237-014-9819-0.

[116] S. Sarker, A Story on the Wave Spectral Properties of Water Hammer, Appl. Mech. 3(3) (2022) 799–814. https://doi.org/10.3390/applmech3030047.

[117] R. Pawlowicz, B. Beardsley, S. Lentz, Classical tidal harmonic analysis including error estimates

References

in MATLAB using TDE, Comput. Geosci. 28 (2002) 929–937. https://doi.org/10.1016/S0098-3004(02)00013-4.

[118]   G. Godin, Compact approximations to the bottom friction term, for the study of tides propagating in channels, Cont. Shelf Res. 11 (1991) 579–589. https://doi.org/10.1016/0278-4343(91)90013-V.

[119]   G.P. Schramkowski, H.E. de Swart, Morphodynamic equilibrium in straight tidal channels: Combined effects of Coriolis force and external overtides, J. Geophys. Res. Ocean. 107 (2002). https://doi.org/10.1029/2000jc000693.

[120]   W. Gong, J. Shen, L. Jia, Salt intrusion during the dry season in the Huangmaohai Estuary, Pearl River Delta, China, J. Mar. Syst. 111–112 (2013) 235–252. https://doi.org/10.1016/j.jmarsys.2012.11.006.

[121]   P. V. Ridd, T. Stieglitz, Dry season salinity changes in arid estuaries fringed by mangroves and saltflats, Estuar. Coast. Shelf Sci. 54 (2002) 1039–1049. https://doi.org/10.1006/ecss.2001.0876.

[122]   D. Xie, C. Pan, S. Gao, Z.B. Wang, Morphodynamics of the Qiantang Estuary, China: Controls of river flood events and tidal bores, Mar. Geol. 406 (2018) 27–33. https://doi.org/10.1016/j.margeo.2018.09.003.

[123]   D. Xie, Z.B. Wang, Seasonal Tidal Dynamics in the Qiantang Estuary: The Importance of Morphological Evolution, Front. Earth Sci. 9 (2021) 1–11. https://doi.org/10.3389/feart.2021.782640.